# Characterisation of the transverse emittance of laser-wakefield-accelerated electrons

**Wolfgang Raphael Weingartner**


München 2018

# Characterisation of the transverse emittance of laser-wakefield-accelerated electrons

**Wolfgang Raphael Weingartner**

Dissertation
an der Fakultät für Physik
der Ludwig–Maximilians–Universität
München

vorgelegt von
Wolfgang Raphael Weingartner
aus Schrobenhausen

München, den 14.09.2018

Erstgutachter: Prof. Dr. Florian Grüner
Zweitgutachter: Prof. Dr. Jörg Schreiber
Tag der mündlichen Prüfung: 22.10.2018

# Zusammenfassung

Die Experimente dieser Doktorarbeit befassen sich mit Aspekten der Strahlenlenkung und der Charakterisierung von Laser-Plasma beschleunigten Elektronen. Ein fokusierter Hochleistungslaser kann Plasmawellen treiben, die elektrische Felder von ca. 100 GV/m aufweisen. Solche elektrischen Felder sind drei bis vier Größenordnungen stärker als solche, die von Hochfrequenzresonatoren ("rf-cavities") wie zum Beispiel am Large Hadron Collider am CERN eingesetzt werden. Ein Plasmabeschleuniger kann daher in entsprechend kürzeren Strecken Teilchen zu hohen Energien beschleunigen. Üblicherweise werden Plasmazellen mit einer Länge von $\sim$1 cm verwendet, mit denen Elektronen mit Energien von mehreren hundert MeV bis einige GeV und $\sim$10 pC erzeugt werden können. Weitere Vorteile dieser Technologie folgen aus der kleinen Größe der Plasmawelle: Diese führt zu einer kurzen Pulsdauer ($<$10 fs) und zu einer geringen transversalen Emittanz der Elektronen. Das Ziel dieser Arbeit war die Vermessung der Emittanz von Laser-Plasma beschleunigten Elektronen.

Durch Messungen mit Quadrupollinsen konnte eine normalisierte Emittanz von $0.21^{+0.01}_{-0.02}$ $\pi$·mm·mrad für Elektronen mit einer Energie von 245 MeV erechnet werden. Zusätzlich zur bekannten "quadrupole scan"-Methode wurde in dieser Arbeit eine Variante entwickelt, welche die Berechnung der Emittanz auch für einzelne Elektronenstrahle errechnen lässt. Die Ergebnisse beider Methoden stimmen überein. Die normalisierte Emittanz bleibt relativ konstant für Energien zwischen 245 und 300 MeV. Dies entspricht der Erwartung von linearen Fokussierfeldern innerhalb der Plasmawelle, eine vorteilhafte Eigenschaft solcher Beschleuniger. In den Experimenten wurde eine auffällig geringe Divergenz der Elektronenstrahlen von $\lesssim$0.5 mrad gemessen. Mithilfe eines einfachen Modells des Übergangs zwischen Plasma und Vakuum können die Divergenz und die Quellgrösse der Elektronen nachgebildet werden. Im Experiment konnte die Beschleunigungslänge und die Elektronendichte variiert werden. Somit konnte die Wechselwirkung zwischen Elektronen und dem Laserpuls innerhalb der Plasmawelle untersucht werden. Die hoch-relativistischen Elektronen holen den Laserpuls ein, werden gestreut, und zeigen eine messbare Vergrösserung der Emittanz auf.

In dieser Arbeit wurden magnetische Quadrupollinsen mit einem Feldgradienten von $\sim$500 T/m verwendet um den Elektronenstrahl zu führen. Indem die Elektronenquelle mit den Quadrupollinsen entsprechend in einem Spektrometer abgebildet wurde, konnte die Auflösung des Spektrometers signifikant erhöht werden. Diese Methode ermöglichte die Messung der Energieverteilung eines Elektronenstrahls von

1% rms bei 190 MeV. Die Strahlenführung kann durch entsprechende Positionierung der Quadrupollinsen für verschiedene Energien angepasst werden. Indem die Linsen den Elektronenstrahl kollimierten, konnte das integrierte Strahlprofil einen Meter nach der Quelle um einen Faktor fünf reduziert werden. Durch einen transversalen Versatz der Quadrupollinsen kann der Elektronenstrahl um einige mrad abgelenkt werden. Die oben genannten Methoden können ohne wesentliche zeitliche Verlängerung, ohne Vergrößerung der transversalen Emittanz und ohne wesentlichen Verlust der Ladung des Elektronenstrahls implementiert werden. Diese kompakte und zuverlässige Methode um plasmabeschleunigte Elektronen zu führen, ist unabhangig vom Beschleuniger selbst und erweist sich als nützliches Werkzeug.

# Abstract

The experiments conducted for this thesis study aspects of the transport and characterisation of laser-wakefield-accelerated (LWFA) electrons. By propagating a high-intensity laser pulse through a plasma, plasma waves with electric fields of the order of 100 GV/m are excited. These fields are three to four orders of magnitude stronger than those generated by radio-frequency cavities commonly used at conventional accelerator facilities such as the Large Hadron Collider at CERN. This technology therefore allows a corresponding miniaturisation of the acceleration length; typical acceleration lengths are $\sim$1 cm and the achieved energies are several hundred MeV to several GeV. Further strengths of this scheme originate from the small accelerating structure, the plasma wakefield, leading to short bunch durations ($<$10 fs), and small beam emittances. It was the main objective this thesis to quantify the transverse emittance of LWFA electron beams.

Using quadrupole scan measurements on LWFA electrons, a normalised transverse emittance of $0.21^{+0.01}_{-0.02}$ $\pi$·mm·mrad at 245 MeV was measured. A modified version of the "traditional" multiple-shot quadrupole scan is shown which enables a single-shot determination of the emittance; the obtained emittance values for both methods agree well. In the energy range of 245 to 300 MeV the normalised emittance remains relatively constant confirming the expectation that plasma wakefields are emittance conserving. The low measured divergences of $\lesssim$0.5 mrad are discussed in the context of a simple model of the beam dynamics in the plasma density downramp at the accelerator exit; the source size and divergence values inferred from the model match the experimental measurement. By altering the acceleration length or the plasma density, the point at which the electron beam interacts with the laser in the plasma could be inferred. The ultra-relativistic electrons can "catch up" to the driver laser and are scattered by it, causing an observable increase in the beam emittance.

For the presented experiments the LWFA electron beams were transported using miniature magnetic quadrupole lenses with field gradients of $\sim$500 T/m. By imaging the electron beams the spectral resolution of a dipole magnet spectrometers can be significantly increased, resulting in measured energy spreads down to 1% rms at 190 MeV. The tunability of the lens system is demonstrated by focusing a range of electron energies. By collimating the beam the integrated beam profile was reduced by a factor of five measured at a distance of one meter from the source. Additionally, by transversely offsetting a quadrupole lens, the electron beam could be steered in any direction by several mrad. These methods can be implemented while still

maintaining the ultra-short bunch duration and low emittance of the beam without any relevant loss of charge. This reliable and compact control of laser-wakefield accelerated electron beams is independent of the accelerator itself, making it a useful tool for transporting LWFA electron beams.

# Contents

# 1. Introduction

The idea to use laser-driven plasma waves to accelerate particles was first published by Tajima and Dawson [1979]. The main advantage of a plasma accelerator is the large accelerating field that is achievable; on the order of ∼100 GV/m. In contrast to this, the radio frequency cavities currently used at CERN for the Large Hadron Collider generate accelerating fields of 5 MV/m. While cavities with stronger fields are common, rf-cavities are ultimately limited by electrical breakdown between the cavity walls.

The experimental breakthrough for laser-plasma acceleration occurred in 2004 with three groups publishing results of ∼ 100 MeV, multi-pC electron bunches, estimated to have a duration of only a few 10s of fs [Geddes et al. 2004; Faure et al. 2004; Mangles et al. 2004]. Since then, several diagnostic tools have been employed to characterise the plasma wakefield as well as the accelerated beams in an effort to improve the understanding and stability of this novel source of ultra-relativistic electrons. Initial efforts to stabilise the generated electron beam were made by adjustment of the laser-pulse and plasma parameters (for example Mangles et al. [2007]), by using alternate injection schemes (for example Faure et al. [2006]), or by refining the gas target [Osterhoff et al. 2008; Schmid et al. 2010]. In addition to the studies above, laser-plasma accelerated beams have been studied in terms of bunch length [Lundh et al. 2011; Buck et al. 2011], confirming a sub-10 fs duration.

## Motivation

The motivation driving this thesis was the characterisation of the transverse emittance of laser-wakefield-accelerated electron beams. The transverse emittance is related to the volume that the beam occupies in position and momentum phase space. As the phase-space volume of the beam is conserved in certain situations, the emittance indicates how well a beam can be transported and focused. It is therefore a key quantity when designing a beamline and a downstream experiment.

## Methodology

Early estimates of the emittance of plasma-accelerated electrons were based on the observed divergence and the expected source size (a fraction of the extent of the transverse wakefield), giving a normalised emittance of ∼1 $\pi$·mm·mrad. Indeed,

such values where approximately confirmed by the first emittance measurements employing the "pepper-pot" method [Fritzler et al. 2004]. This technique relies on scattering electrons passing through the pepper-pot mask and therefore becomes increasingly challenging the higher the beam energy. Despite this limitation, measurements of a 3 GeV beam have been carried out [Thomas et al. 2013]. As illustrated by Cianchi et al. [2013], the pepper-pot method is not suitable to measure the emittance of beams with a large divergence and initial source size smaller than 10 µm due to poor sampling of the phase space.

An alternative method is to analyse the betatron radiation emitted by the electron beam while it is in the plasma. The beam size is measured to be $\lesssim$1 µm, which in combination with a downstream divergence measurement gives an estimated emittance of 0.5 $\pi$·mm·mrad [Kneip et al. 2012]. However, inferring the emittance from the electron beam size in the plasma and its downstream divergence in the vacuum can be unreliable as this neglects the plasma-to-vacuum density transition at the accelerator exit; here the decreasing strength of the plasma focusing forces result in an increase in beam size and decrease in divergence [Sears et al. 2010a; Thaury et al. 2015]. Kneip et al. [2012] argue that the effect of the plasma-to-vacuum transition can be neglected as long as it is short compared to the betatron wavelength of the beam.

Neither of the above-discussed techniques are spectrally resolved, they therefore rely on a low energy spread to give a meaningful normalised emittance. For LWFA beams which fluctuate in energy and energy spread, a simultaneous measurement of the spectrum is required.

This thesis reports on measurements of the emittance of LWFA electron beams that are both energy resolved and that include the beam transport of the density downramp at the accelerator exit. The emittance calculation is based on analysing the electron beam size around a focus using a quadrupole lens scan method. Quadrupole lenses are useful tools to control and reliably apply LWFA electron beams while still preserving their intrinsic advantages of ultra-short pulse duration and low emittance. They are well-suited for the task of steering beams by several mrad and in particular, significantly reduce the spatial fluctuations caused by the inherent pointing instabilities of these accelerators. Like the pepper-pot, the quadrupole-scan method is limited by the beam energy: the beam must be focusable by the quadrupole lenses. For a beam with very high charge, space charge during propagation to focus will lead to an emittance increase. Furthermore, the beam is focused which may be problematic for simultaneous application of the beam. Despite these limitations, the presented technique is applicable to most state-of-the-art LWFA experiments.

Using magnetic lenses for imaging an electron beam is analogous to that of an optical beam where the final position of a ray at the image plane is independent of

its incoming angle. This decoupling is very useful if the incoming beam is fluctuating in angle due to pointing instabilities as this can be mitigated by the imaging. A position-jitter at the source plane results in a correspondingly magnified jitter at the image plane. The image plane can be set at a finite or infinite distance behind the lens resulting in the focusing or collimation of the beam.

## Applications

Knowledge of the electron beam emittance is important for the further application of LWFA beams. Two relevant examples are the generation of radiation with a free-electron laser [Maier et al. 2012] and the staging of successive plasma accelerators to achieve higher beam energies (see for example Schroeder et al. [2010]). In both cases, the value of the emittance fundamentally affects the design of the experiments.

The potentially detrimental effect of energy and energy spread fluctuations of the LWFA electrons on applications such as the generation of undulator radiation can be mitigated with PMQ lenses [Fuchs et al. 2009]. The chromaticity of a PMQ focusing system can be employed as an energy bandpass filter to select a certain electron energy to be transported through the system. Photon sources that are based on ultra-relativistic electrons such as undulator radiation and inverse Compton scattering have the inherent property of emitting mainly along the electron beam propagation direction. This places a central role on the electron beam transport system as it can tailor the subsequently generated photon beam to be focused on a target without the complication of lossy x-ray optics. Positioning the lenses such that electrons with energy $E_0$ are focused at the detector will decrease the flux intensity emitted by electrons with energies $E \neq E_0$ thereby enabling the tuning of the wavelength of this type of radiation with PMQ lenses [Fuchs et al. 2009].

## Structure of this thesis

This thesis is structured into the following chapters:

**Chapter 2:** briefly describes the theoretical models for laser-wakefield acceleration such as laser propagation in a plasma, plasma wave-generation, electron-injection and acceleration. The chapter is concluded by discussing some expected scalings for the electron beam parameters.

**Chapter 3:** discusses the transport of the electron beam. From this the calculation for the electron beam emittance used in the experimental part of this work is obtained. The conditions for imaging a beam with a quadrupole doublet are discussed, along with the potential detrimental effects to the electron beam quality. The chapter finishes by discussing different techniques for measuring the electron beam emittance.

**Chapter 4:** discusses the experimental setup and its limitations. The major components of the experiment are discussed: the laser, the gas target, the magnetic quadrupole lenses, and the electron beam diagnostics. The chapter analyses the possible errors and their effects on the calculated emittance. For the case of the quadrupole lenses, measured field maps of the lenses are used in tracking simulations to check the effect of aberrations and positioning errors on the electron beam.

**Chapter 5:** shows experimental results concerning laser-wakefield accelerated electrons. Typical electron beams had a peak containing approximately 15 pC of charge and energies of about 300 MeV. These beams were the basis for the subsequent work with quadrupole lenses concerning beam transport and the characterisation of the transverse phase space.

**Chapter 6:** shows experimental results regarding the transport and characterisation of laser-wakefield accelerated electron beams. Section 6.1 shows how the spatial stability of the beam can be improved and the results of a high-resolution imaging spectrometer using a combination of a lens doublet and a dipole magnet. Section 6.2 shows the measurement of the electron beam emittance for three energies and the effect of the accelerator length and the plasma density on the emittance.

**Chapter 7:** concludes the thesis by summarising the results and discussing the remaining open questions.

# 2. Laser-wakefield acceleration of electrons

This chapter discusses the theory behind laser-wakefield acceleration of electrons in plasma. The goal is to give an understanding of the mechanisms involved in the creation of an accelerating structure (the plasma wakefield), the injection of electrons into the structure, the dynamics of the electrons during acceleration, and the exit of the electrons from the plasma (transition to vacuum). Laser-wakefield acceleration is a complex interaction between the driving laser and the plasma. The easiest way to approach the interaction is to start with a one-dimensional model assuming a constant laser intensity and plasma density. This simple model is explored for most of the chapter and already gives valuable insight into the acceleration process. An extension to two dimensions helps to understand the injection of electrons into the plasma wakefield and is discussed in section 2.7. At the end of the chapter, a short summary of effects particularly relevant to the experimental measurements of this thesis are given. For a thorough review of the theory, the reader is referred to [Esarey et al. 2009], which is the basis for much of this chapter.

## 2.1. Fundamentals

Before describing the laser-plasma interaction, some fundamentals about laser fields, plasmas, and the motion of a single electron in a laser field are discussed.

### 2.1.1. Description of the laser field

Normalised vector potential
Laser ionisation

---

Light is an electro-magnetic (EM) wave which is characterised by its electric and magnetic fields, $\vec{E}$ and $\vec{B}$. The relationship between these fields and their variation in time and space is described by Maxwell's equations:

$$\nabla \cdot \vec{E} = \frac{\rho}{\varepsilon_0},$$

$$\nabla \cdot \vec{B} = 0,$$

$$\nabla \times \vec{B} = \mu_0 \left( \varepsilon_0 \frac{\partial \vec{E}}{\partial t} + \vec{j} \right),$$

$$\nabla \times \vec{E} = -\frac{\partial \vec{B}}{\partial t}.$$

The constants $\mu_0, \varepsilon_0$, and $c$ are the permeability, the permittivity, and the speed of light in vacuum and are related to each other through $c = (\mu_0 \varepsilon_0)^{-1/2}$. The charge density is represented by $\rho$, and the current density by $\vec{j}$. In vacuum with no charges ($\rho = 0$) nor currents $\vec{j} = 0$ and after some algebra with Maxwell's equations the wave equation can be obtained:

$$\frac{1}{c^2} \frac{\partial^2 \vec{E}}{\partial t^2} - \nabla^2 \vec{E} = 0,$$

an analogous equation can be obtained for the magnetic field. A solution to the electric wave equation with space vector $\vec{r}$ and time $t$ is:

$$\vec{E} = \vec{E_0}(\vec{r}, t) \sin(\omega t - \vec{k}\vec{r} + \phi). \tag{2.1}$$

The envelope vector $\vec{E_0}$ determines the magnitude and polarisation of the field oscillation. The remaining parameters $\omega, \vec{k}, \phi$ represent the angular frequency, the wave vector ($\vec{k} = 2\pi/\lambda$), and an arbitrary phase offset respectively. An EM-wave can also be described in terms of the vector potential as:

$$\vec{A} = \vec{A_0} \cos(\omega t - \vec{k}\vec{r} + \phi)$$

The magnitudes of the vector fields are related by $|\vec{E_0}| = c|\vec{B_0}| = \omega|\vec{A_0}|$. A useful quantity in the context of interactions between high-intensity lasers and matter is the **normalised vector potential**:

$$a_0 = \frac{q_e |\vec{A_0}|}{m_e c}, \tag{2.2}$$

where $q_e$ and $m_e$ are the electron charge and rest mass respectively. EM-waves transport energy as they propagate, which is described by the energy-flux ("Poynting") vector:

$$\vec{S} = \varepsilon_0 c^2 (\vec{E} \times \vec{B})$$

The intensity of the EM-wave is given by averaging over one cycle of the fields:

$$I = \langle \vec{S} \rangle = \varepsilon_0 c |\vec{E}|^2 \tag{2.3}$$

Using equation 2.3 the normalised vector potential can be written in convenient units:

$$a_0 = 0.854 \sqrt{I[10^{18}\mathrm{W/cm}^2]} \cdot \lambda[\mu m] \tag{2.4}$$

Current femtosecond high-power laser systems are often based on Titanium-Sapphire crystals which have a central wavelength at $\sim 800$ nm. A laser intensity of $a_0 = 1$ corresponds to an intensity of $2 \times 10^{18}\mathrm{W/cm}^2$ and an electric field amplitude of $\sim 2 \times 10^{12}$ V/m. The ATLAS laser facility used for the work in this thesis reaches intensities in focus of $\sim 1.2 \times 10^{19}\mathrm{W/cm}^2$, which corresponds to $a_0 = 2.4$.

### 2.1.2. Plasma

A plasma is an ionised gas consisting of positively charged ions and unbound electrons. The electrons are free in the sense that they are not each bound to a particular ion as in the gaseous state, and hence more mobile. The plasma generated by an intense laser pulse in a gas is quasi-neutral as it contains equal amounts of positive and negative charge. A displacement of some electrons will therefore result in regions of net negative and net positive charge and therefore a resulting electric field. The displaced electrons will be accelerated back towards the positive charge region and overshoot due to the kinetic energy they have gained. The resulting motion will be a harmonic oscillation at the **plasma frequency**:

$$\omega_p = \sqrt{\frac{n_e e^2}{\langle \gamma \rangle m_e \varepsilon_0}}, \tag{2.5}$$

where $n_e$ represents the electron density, $e$ the charge of an electron, $\langle \gamma \rangle$ the Lorentz factor averaged locally over many electrons, $m_e$ the electron mass, and $\varepsilon_0$ the electric permittivity of free space. With $\lambda_p = 2\pi c/\omega_p$, a plasma wavelength can be defined and written in convenient units:

$$\lambda_p[\mu\mathrm{m}] = 3.3 \times 10^{10} / \sqrt{n_e[\mathrm{cm}^{-3}]}. \tag{2.6}$$

A typical electron density as used in the experiments of this thesis of $6 \times 10^{18}\mathrm{cm}^{-3}$ results in a plasma wavelength of $\sim$13 µm.

In the experiments conducted for this thesis, hydrogen gas was used as a target. Above a threshold electric field strength the atomic potential barrier for the electron is completely suppressed and the electron is ionised ("barrier suppression ionisation"). This threshold is reached for a laser intensity of $\sim 1 \times 10^{14}\mathrm{W/cm^2}$,[i] which is orders of magnitude below the intensity reached by the ATLAS laser.

### 2.1.3. Single-electron motion in laser field

Quiver motion
Ponderomotive force

In the previous section it was concluded that a hydrogen gas will be fully ionised in the focal region of a high-power laser such as the one used in the experimental part of this thesis. The interaction of the laser field is then mainly with the individual electrons and ions of the plasma which will be discussed here.

#### Quiver motion

A particle with rest mass $m$ and charge $q$ in a laser electromagnetic field $\vec{E}/\vec{B}$ is subjected to the Lorentz force:

$$\frac{d\vec{p}}{dt} = \frac{d}{dt}(\gamma m\dot{\vec{r}}) = q\left[\vec{E}(\vec{r},t) + \dot{\vec{r}} \times \vec{B}(\vec{r},t)\right].$$

If during the interaction the particle velocity is much smaller than the speed of light ($\dot{r} << c$), and as for an EM-wave $|\vec{B}| = |\vec{E}|/c$, the $q\dot{\vec{r}} \times \vec{B}$ term of the Lorentz force can be neglected. Furthermore, an infinite plane wave solution to the wave equation 2.1 of the form $\vec{E}(\vec{r},t) = \vec{E}_x \sin(\omega t - kr)$ is assumed. As the relativistic gamma factor of the particle $\gamma \approx 1$, a "first-order" equation of motion is obtained:

$$m\ddot{\vec{r}}_{quiv.} = q\vec{E}(\vec{r}_{quiv.}, t).$$

The influence of a radial dependence of the electric field will be introduced below. Inserting the infinite plane wave [ii] and integrating over time, the particle "quiver"

[i] The required laser intensity for BSI can be estimated by overlaying a constant electric field (assumption: laser field not changing on the time scale of the electron dynamics)) on top of the Coloumb potential of the hydrogen atom (see Osterhoff [2008])

[ii] The infinite plane wave has neither radial nor longitudinal dependency. Neglecting the longitudinal dependency is actually a reasonable approximation for realistic laser beams and is often called the "slowly varying envelope approximation". In this case it is justified if a laser oscillation occurs much faster than the time in which the laser amplitude changes. For a Ti:Sa laser pulse with a wavelength of 800 nm an oscillation occurs in under 3 fs, much shorter than the typical pulse lengths of ~20 fs.

velocity and trajectory in the EM wave at time $t$ is obtained:

$$\dot{\vec{r}}_{quiv.} = \frac{q}{m}\int_0^t d\tau \left[\vec{E}_x \sin(\omega\tau - kr)\right] = \frac{-q\vec{E}_x}{m\omega}\cos(\omega t - kr) \tag{2.7}$$

$$\vec{r}_{quiv.} = \frac{-q\vec{E}_x}{m\omega^2}\sin(\omega t - kr) \tag{2.8}$$

Rewriting the quiver velocity in terms of the normalised vector potential (equation 2.2) gives for the maximum velocity $\dot{r}_{quiv.,\max} = (m_e/m)(q/q_e)a_0 c$. For an electron the factors in brackets are both 1. If the normalised vector potential $a_0$ approaches 1, the quiver velocity approaches $c$ and the electron is accelerated to relativistic velocities within a single cycle of the laser field. The normalised laser vector potential therefore has a convenient threshold between the non-relativistic ($a_0 < 1$) and the relativistic ($a_0 > 1$) regimes. In the relativistic case the initial assumption that $\dot{r} << c$ is no longer fulfilled and the full Lorentz force including the $\vec{B}$-field must be used. For a proton, $m_e/m \sim 1/1800$, and therefore its quiver velocity is reduced by the same fraction and is essentially stationary for the time scales of the laser-plasma interactions discussed in this thesis.[iii]

The maximum of the quiver trajectory is $r_{quiv.,\max} = (m_e/m)(q/q_e)a_0 c/\omega$. For a Ti:Sa laser with $a_0 = 1$ and the assumptions made in this section, the maximum excursion of an electron is $\sim 130$ nm.

### Ponderomotive force

In the above reasoning for the quiver motion only the transverse trajectory due to the electric field was considered (first-order motion). If the EM-wave has a transverse intensity dependence (such as a laser beam as opposed to an infinite plane wave), the oscillatory quiver motion will no longer be centred around a constant point. The particle will quiver *and* "drift" away from regions of high intensity. This can be intuitively understood by considering a particle oscillating in the electric field of a Gaussian laser beam, starting at the high-intensity centre moving outwards. After it has completed the first half oscillation out to its turning point and is just about to swing back in the direction it came from, it experiences a weaker electric field than it did on axis where the beam intensity is maximum. The force returning the particle to the high-intensity centre is therefore also weaker. The resulting net force to describe the "drift" away from high-intensity regions is called the **ponderomotive force** and

[iii] To accelerate protons to relativistic speeds within one optical cycle requires laser intensities on the order of $I_L = 10^{24}$ to $10^{25}$ W/cm$^2$, or $a_0 \sim 1000$. This intensity is beyond the reach of current high-power laser systems.

a derivation in the non-relativistic case considers the motion of the particle *other* than the quiver trajectory $\vec{r}_{quiv.}$, i.e. including changes in the electric field with radial dependence and the $\dot{\vec{r}} \times \vec{B}$ term (second-order motion).[iv] To introduce the radial dependence the electric field is expanded around the quiver trajectory centre position $\vec{r}_0$:

$$\vec{E}(\vec{r}) = \vec{E}(\vec{r}_0) + (\vec{r}_{quiv.} \cdot \vec{\nabla})\vec{E}(r_0) + ...,$$

where the general position vector $\vec{r}$ has been separated into $\vec{r}_{quiv.}$ which follows the particle, and $\vec{r}_0$ which is the centre of the quiver oscillation. Using Faraday's law ($\vec{\nabla} \times \vec{E} = -\frac{d\vec{B}}{dt}$), an expression for $\vec{B}$ in terms of $\vec{E}$ can be obtained:

$$\vec{B}(\vec{r}_0) = -\frac{1}{\omega}\vec{\nabla} \times \vec{E}_0(\vec{r}_0)\cos(\omega t).$$

Using these expressions, the second-order motion is given by subtracting the quiver motion from the full Lorentz force:

$$\frac{d\vec{p}_{\text{pond.}}}{dt} = \frac{d\vec{p}}{dt} - \frac{d\vec{p}_{quiv.}}{dt} = q\left[\underbrace{\vec{E}(\vec{r}) - \vec{E}(\vec{r}_0)}_{(\vec{r}_{quiv.}\cdot\vec{\nabla})\vec{E}(\vec{r}_0)} + \dot{\vec{r}}_{quiv.} \times \vec{B}(\vec{r}_0)\right].$$

The electric field terms $(\vec{E}(\vec{r}) - \vec{E}(\vec{r}_0))$ are replaced by the Taylor expansion term. Substituting the quiver motion into this expression and averaging over a laser period gives:

$$\left\langle \frac{d\vec{p}_{\text{pond.}}}{dt} \right\rangle = -\frac{q^2}{m\omega^2}\frac{1}{2}\left[(\vec{E}(\vec{r}_0) \cdot \vec{\nabla})\vec{E}(\vec{r}_0) + \vec{E}(\vec{r}_0) \times (\vec{\nabla} \times \vec{E}(\vec{r}_0))\right].$$

Applying the vector dot product rule ($(\vec{A} \cdot \vec{\nabla})\vec{A} + \vec{A} \times (\vec{\nabla} \times \vec{A}) = 1/2\vec{\nabla}|A|^2$), results in the non-relativistic ponderomotive force:

$$\vec{F}_{\text{pond.}} = -\frac{1}{4}\frac{q^2}{m\omega^2}\vec{\nabla}|\vec{E}(\vec{r}_0)|^2. \tag{2.9}$$

The motion of an electron in a laser field is thus a combination of the oscillation with the electric field and a drift away from regions of high intensity (due to the negative sign in front of the gradient operator).

[iv] Here only the non-relativistic case is considered. This means that $\dot{\vec{r}}$ term is solely determined by the quiver velocity in the transverse plane. For $\dot{r} \to c$ a significant or even dominant part of $\dot{\vec{r}}$ will point in the direction of propagation due to the magnetic field term of the Lorentz force.

## 2.2. Laser propagation and evolution in under-dense plasmas

Dispersion relation
Laser self-focusing

The terms **over-** and **under-dense plasma** describe whether an inbound electromagnetic wave will propagate through the plasma (under-dense) or be attenuated and reflected at the boundary (over-dense). This depends on the ratio of the EM-wave frequency and the plasma frequency $\omega_L/\omega_p$. If $\omega_L/\omega_p < 1$, the plasma electrons are able to follow the oscillations of the EM-wave and shield its field inside the plasma. A ratio of one is referred to as the critical density and is given by $n_c = \omega^2\langle\gamma\rangle m_e\varepsilon_0/e^2$. For the non-relativistic case and a 800 nm EM-wave, the threshold density is at $1.7 \times 10^{21}\mathrm{cm}^{-3}$. This density is well above the typical values of $\sim 10^{18}\mathrm{cm}^{-3}$ used in the experiments in this work. Therefore an incoming laser beam will propagate into the plasma instead of being mostly reflected by it.

The dispersion relation for a plane EM wave in plasma is:

$$\omega_L^2 = \omega_p^2 + c^2 k_L^2 \tag{2.10}$$

The resulting index of refraction is

$$\eta = \sqrt{1 - \left(\frac{\omega_p}{\omega}\right)^2}. \tag{2.11}$$

It is related to the phase velocity $v_{\mathrm{ph}}$ and the group velocity $v_{\mathrm{g}}$ of the EM-wave as follows:

$$v_{\mathrm{ph}} = \frac{\omega}{k} = \frac{c}{\eta} \tag{2.12}$$

$$v_{\mathrm{g}} = \frac{d\omega}{dk} = \eta \cdot c \tag{2.13}$$

Although the refractive index is generally smaller than one, the group velocity of a laser pulse is always smaller than the vacuum speed of light. The group velocity can also be expressed in terms of a Lorentz gamma factor of $\gamma_g = (1 - v_g^2/c^2)^{-1/2} = \omega_L/\omega_p \propto n^{-1/2}$. Therefore as expected the laser pulse is slowed down more by higher plasma densities. The effect of the laser intensity has been ignored here. The nonlinear correction leads to an increase of the group velocity with higher laser intensity [Schroeder et al. 2011].

### 2.2.1. Laser self-focusing

A laser pulse with high enough power propagating through an under-dense plasma can produce a focusing effect that can counteract diffraction and maintain or even decrease its beam size. The concept behind such "self-focusing" is that the laser-plasma interaction leads to a refractive index which is *high* on-axis and drops off from the centre, i.e. $d\eta/dr < 0$. This leads to slower laser phase fronts on-axis than off-axis and hence the beam focuses towards the axis in what can be referred to as "refractive focusing".

The refractive index of equation 2.11 can be re-written using the definition of the plasma frequency shown in equation 2.5 as

$$\eta \approx 1 - \frac{1}{2}\left(\frac{\omega_{p,0}}{\omega}\right)^2 \frac{n_e}{n_{e,0}\gamma}. \tag{2.14}$$

Here it was assumed that $(\omega_{p,0}/\omega)^2 << 1$ (which is correct to within $\sim 10^{-6}$ even for the highest plasma densities used in this thesis) and the subscripts with zero indicate the "unperturbed" plasma without the influence of the laser. The free parameters are the plasma density $n_e$ and the local relativistic factor of the plasma electrons $\gamma$ (i.e. their relativistic mass). To obtain refractive focusing of the laser beam requires a transverse plasma density profile of $dn_e/dr > 0$ (lower density on-axis) or a larger electron mass on-axis $d\gamma/dr < 0$. Both the plasma density and the relativistic factor of the electrons are influenced by the laser-plasma interaction:

**Relativistic focusing**: The first order motion of an electron in a laser field is the quiver motion as discussed in section 2.1.3. For high laser intensities this motion leads to relativistic electron velocities and a corresponding increase in mass. For a Gaussian beam profile the intensity and hence the quiver velocity is largest on-axis leading also to the largest electron mass on axis.

**Ponderomotive focusing**: The ponderomotive force of the laser pushes electrons away from regions of high intensity. The plasma density is therefore lower on-axis and hence supports self-focusing.

The threshold power for self-focusing including both relativistic and ponderomotive focusing is (see Sun et al. [1987]) $P_L \sim 16.2(\omega/\omega_p)^2$[GW]. For a density of $6 \times 10^{18}\text{cm}^{-3}$ and the ATLAS laser this requires a laser power of $\gtrsim$ 4TW. An ATLAS pulse has a power of approximately 70 TW. Hence, self-focusing is expected in the experiments conducted with the ATLAS laser. From the dependence on $1/\omega_p^2$ it is clear that the necessary laser power to sustain self-focusing increases for lower densities.

Self-focusing is a self-accelerating process: a progressively smaller beam size leads to a higher intensity and hence even higher electron mass and lower density on-axis.

The process depends on modifying the plasma electrons and can continue until all electrons have been expelled from the laser axis. Sun et al. [1987] show that the power required to completely expel all electrons (termed "cavitation") from the laser axis is $P \sim 1.1 P_L$, only slightly above the threshold for self-focusing to begin.

The condition for successful self-focusing is not purely a question of the laser power. As can be seen in figure 2.2, the ponderomotive force of the driver laser pushes a small "bump" of electrons ahead of it. This slightly higher electron density approximately compensates the increase of refractive index caused by the local relativistic mass increase of the electrons (Esarey et al. [2009]; Lu et al. [2007]). Hence, it is not possible to guide short laser pulses ($L = c\tau < \lambda_p$) over long distances (several Rayleigh lengths). For slightly longer pulses ($L \sim \lambda_p$), it has been shown experimentally that guiding can occur so long as the *transverse* beam size is larger than the plasma wavelength ($w_0 > \lambda_p$, see Thomas et al. [2007]). This ensures that the expelled electrons from the laser axis do not return to the axis within the laser pulse. These returning electrons would lead to density variations along the axis which can lead to a modulation or even a breaking up of the laser pulse into filaments.

## 2.3. Plasma wave generation

As was established in section 2.1.3, the ponderomotive force of a laser beam pushes electrons away from regions of high intensity. As is illustrated by figure 2.1, a plasma wakefield is excited which follows the laser pulse. In this section the generation and properties of such plasma waves will be discussed both in the linear ($a_0 << 1$) and the non-linear ($a_0 \gtrsim 1$) regime.

### 2.3.1. Linear plasma wake

The linear regime can be examined using the cold fluid equations (Poisson's, the continuity, and the momentum equations). The plasma wave and the associated wake fields that are excited by a laser beam is described by [Esarey et al. 1996]:

$$\left(\frac{\partial^2}{\partial t^2} + \omega_p^2\right)\frac{\delta n}{n_0} = c^2\nabla^2\frac{a_0^2}{2},$$

$$\left(\frac{\partial^2}{\partial t^2} + \omega_p^2\right)\phi = \omega_p^2\frac{a_0^2}{2},$$

where the laser, represented by $a_0$, drives $\delta n/n_0 = (n - n_0)/n_0$ which is the normalised density perturbation and the associated normalised electrostatic wake

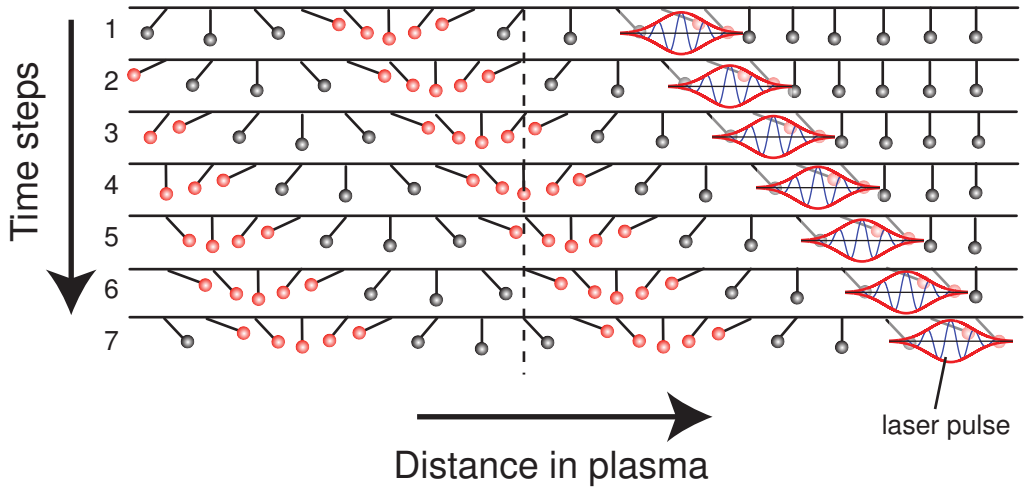


**Figure 2.1. – Simplified picture of plasma wave generation.** The ponderomotive force of a laser pulse propagating through a plasma causes a displacement of electrons which are pulled back to their original position (electrons depicted as balls on a pendulum). Two important aspects are apparent from this picture: 1) the higher density regions (red electrons) follow the laser at the speed of its group velocity through the plasma. 2) The plasma wavelength determines the distance between density peaks. No net transfer of electrons occurs as can be seen by the electron oscillating around the dashed vertical line. Illustration courtesy of M. Fuchs.

$\phi = e\Phi/mc^2$. Following [Esarey et al. 1996] and introducing a co-moving coordinate with the laser pulse ($\xi = z - ct$), the solutions for a Gaussian-like laser pulse $a^2 = a_0^2 \exp(-\frac{2r^2}{r_s^2}) \sin^2(\frac{\pi\xi}{L})$ for $0 < \xi < L$ are:

$$\frac{\delta n}{n_0} = -\frac{\pi}{8} a_0^2 \left[1 + \frac{8}{k_p^2 r_s^2}\left(1 - \frac{2r^2}{r_s^2}\right)\right] \exp\left(-\frac{2r^2}{r_s^2}\right) \sin(k_p \xi), \tag{2.15}$$

$$\frac{E_z}{E_0} = -\frac{\pi}{8} a_0^2 \exp\left(-\frac{2r^2}{r_s^2}\right) \cos(k_p \xi). \tag{2.16}$$

This solution is for a linearly polarised laser and $L = \lambda_p$. $E_0$ is the non-relativistic wavebreaking field. This maximum field for a linear plasma wave can be estimated from Poisson's equation, $\nabla \cdot \vec{E} = -ne/\varepsilon_0$, and assuming that all electrons are participating in the oscillation: $n = n_0 \cos(k_p z - \omega_p t)$. In the 1D case $E = -e/\varepsilon_0 \int n dz = -en_0/(\varepsilon_0 k_p) \sin(k_p z - \omega t)$. Utilising equation 2.5, the cold

non-relativistic wave-breaking field is given by:

$$E_0 = cm_e\omega/e = 96\sqrt{n_0(\mathrm{cm}^{-3})}\,(\mathrm{V/m}) \tag{2.17}$$

The transverse fields can be obtained from the Panofsky-Wenzel theorem which relates the transverse and the longitudinal forces for a particle passing through a region of electromagnetic fields [Vaganian and Henke 1995]: $\partial F_z/\partial r = \partial F_\perp/\partial\xi$.[v] The transverse focusing force is thus given by:

$$F_\perp = \frac{4r}{k_p r_s^2} E_0 e \frac{\pi}{8} a_0^2 \exp\left(-\frac{2r^2}{r_s^2}\right)\sin(k_p\xi) \tag{2.18}$$

From equations 2.16 and 2.18, it can be seen that the accelerating and focusing fields are $\pi/2$ out of phase. Therefore in half of the accelerating phase electrons can be both accelerated *and* contained as a beam in the transverse direction.

### 2.3.2. Non-linear plasma wake

As discussed in previous sections, laser pulses can propagate through underdense plasmas. If the pulse has a high intensity, its ponderomotive force can displace large amounts of electrons and excite large-amplitude plasma waves. A differential equation governing the plasma response in the high-intensity ("non-linear") regime can be derived in 1D Sprangle et al. [1990]. The assumptions in this derivation are:

1. Collisions (and plasma recombination) can be neglected.

2. Quasi-static approximation (QSA): the laser envelope does not evolve during the interaction.

3. Thermal effects can be neglected provided the electron quiver velocity ($\sim c$) is much greater than the thermal velocity.

The calculations are performed in the co-moving coordinate system $\xi$ ($\xi = z - v_g t$). This means the plasma is flowing through a nearly stationary laser pulse which itself is only changing very slowly (QSA). The combination of Poisson's equation for the electric potential, the electron fluid momentum, and continuity equations leads to the plasma response to the laser pulse:

$$\frac{\partial^2\phi}{\partial\xi^2} = \frac{k_p^2}{2}\left(\frac{1+a_0^2}{(1+\phi)^2} - 1\right). \tag{2.19}$$

[v] The forces on the particle come from a single potential, i.e. $F_\perp = -\partial_r\psi$ and $F_z = -\partial_\xi\psi$. It then follows that $\partial_r F_z = \partial_\xi F_\perp$.

The normalised electric potential periodically varies between the minimum and maximum values of:

$$\phi_m = \frac{\hat{E}_{\max}^2}{2} \pm \beta_p \sqrt{\left(1 + \frac{\hat{E}_{\max}^2}{2}\right)^2 - 1}, \tag{2.20}$$

where $\hat{E}_{\max} = E_{\max}/E_0$ is the maximum electric field and $\pm$ is for $\phi_{\max}$ and $\phi_{\min}$. After solving for $\phi$, the density perturbation can be obtained with:

$$\frac{n}{n_0} = \frac{(1 + a_0^2) + (1 + \phi)^2}{2(1 + \phi)^2}. \tag{2.21}$$

The influence of the induced plasma wave on the laser pulse is described by the corresponding wave equation (see Sprangle et al. [1990]) and forms a self-consistent pair of differential equations. For simplicity, only the plasma response is considered here; the laser does not evolve.

Figure 2.2 shows the induced electron density wave and the associated longitudinal electric field driven by a short laser pulse. The density is periodic but is no longer sinusoidal as in the linear regime. The electric field shows the characteristic "sawtooth" shape with an approximately linear dependence with $\xi$ between the density peaks. A non-linear plasma wave can sustain fields larger than in the linear case due to the large-amplitude density peaks. Not only the shape of the plasma response changes, but also the period of the non-linear plasma increases:

$$\lambda_{\mathrm{N}p} = \lambda_p \begin{cases} 1 + \frac{3}{16}\left(\frac{E_{\max}}{E_0}^2\right) & \text{for } \frac{E_{\max}}{E_0} \ll 1, \\ \frac{2}{\pi}\left(\frac{E_{\max}}{E_0} + \frac{E_0}{E_{\max}}\right) & \text{for } \frac{E_{\max}}{E_0} \gg 1. \end{cases} \tag{2.22}$$

For a square laser pulse, an analytical solution to equation 2.19 exists. For an optimum driver-laser length for plasma wave excitation ($L \simeq \lambda_{\mathrm{N}p}/2$), the axial electric field is given by Esarey et al. [2009]:

$$\hat{E}_{\max} = \frac{E_{\max}}{E_0} = \frac{a_0^2/2}{\sqrt{1 + a_0^2/2}}. \tag{2.23}$$

The dependence on $a_0$ has interesting consequences in 3D. For the 1D case the laser intensity can only vary in the propagation direction and is assumed to be infinite transversely. In 3D the radial drop in intensity means that the plasma wavelength also decreases off-axis, leading to curved "horse-shoe" like wakefields (see figure 6.10 for a 3D computer simulation showing this effect).

The validity of these 1D considerations can be checked by comparing the max-

imum electric fields to those measured experimentally. By using a variable-length accelerator and measuring the resulting electron energies, the maximum accelerating field can be obtained by extrapolation. With this method a maximum field of $\approx 160$GV/m was measured for a density of $6.5 \times 10^{18}$cm$^{-3}$ [Popp 2011]. The fields from the 1D theory using the same plasma density and laser parameters can be seen in figure 2.2 to be approximately 310 GV/m. The cold wave-breaking field is 245 GV/m (equation 2.17), and the approximation for a square pulse is 415 GV/m. Although the theoretical values overestimate the measured accelerating field, they give a usable estimate.

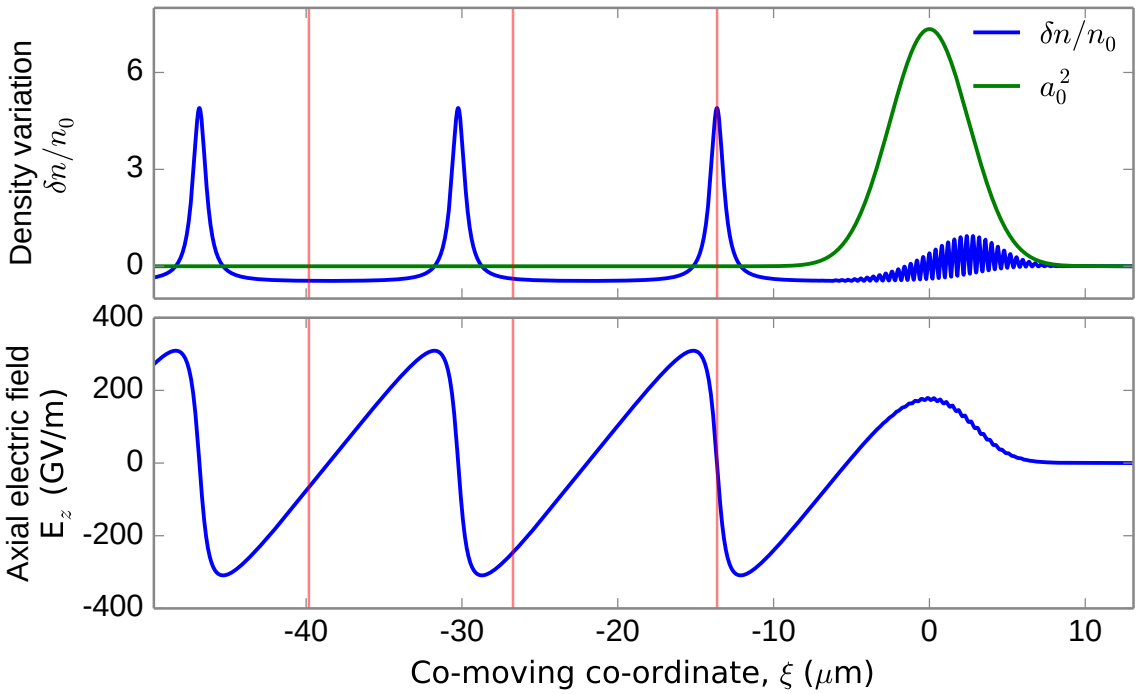


**Figure 2.2. – Non-linear plasma wave generation.** A laser pulse with $a_0 = 2.7$ and 20 fs duration drives a non-linear plasma wave. The density perturbation is obtained by solving equations 2.19 and 2.21. The background plasma density is $6.5 \times 10^{18}$cm$^{-3}$. The vertical red lines illustrate two *linear* plasma wavelengths behind the first density spike trailing the laser (calculated using equation 2.5). Compared with the linear regime, the non-linear case exhibits a longer periodicity and more pronounced density spikes.

## 2.4. Self-injection of electrons

Self-injection
Scalings for the electron beam parameters
Beam-loading

A number of methods can be used to "inject" or "trap" electrons in the plasma wave and allow them to be accelerated by the strong axial electric field. The simplest conceptually and usually also in terms of experimental effort is self-injection. Here the plasma wakefield is driven by the laser until wavebreaking occurs and electrons are "spilled" into the wake-cavity. The wavebreaking process itself is highly non-linear: slight differences in laser and plasma parameters lead to significant changes in the resulting accelerated electron beam [Mangles et al. 2007]. Alternative injection schemes include:

**Ionisation injection:** The target gas is composed of two or more species of gas, for example, hydrogen and nitrogen. The laser intensity is chosen such that the high-Z gas is only fully ionised by the peak laser intensities. In this way, some electrons are ionised at a very specific position in the wakefield and therefore injection can be somewhat controlled.

**Colliding-pulse injection:** By using a second laser pulse (often propagating perpendicularly to the main driver pulse), the superimposed laser intensity of both pulses can be adjusted to inject electrons at a particular position in the wakefield.

**Injection at a plasma density transition:** The plasma density affects both the plasma wavelength and the speed of the laser (and hence the trailing wakefield) through the plasma. Geddes et al. [2008] focused a laser at the downstream edge of a gas jet with a density reduction of 50% over a length of ≈300 µm starting with a plasma wavelength of 7 µm. Although the laser group velocity increases due to the decreasing density, the plasma wavelength also increases leading to slower wake phase front velocity and easier trapping. A modified scheme employing a razor blade to cause a density shockwave was used to generate a similar downramp within just 5 µm [Schmid et al. 2010]. In this scheme electrons are "rephased" by the sudden change of plasma wavelength within the length of just a single plasma wavelength.

The self-injection mechanism will be approached by considering the effects that facilitate injection. The motion of an electron in the potential of a plasma wave can be analysed with the Hamiltonian in the co-moving frame [Esarey and Pilloff 1995]:

$$H(p_z, \xi) = \sqrt{p_z^2 + 1 + a^2} - \beta_p p_z - \phi(\xi). \tag{2.24}$$

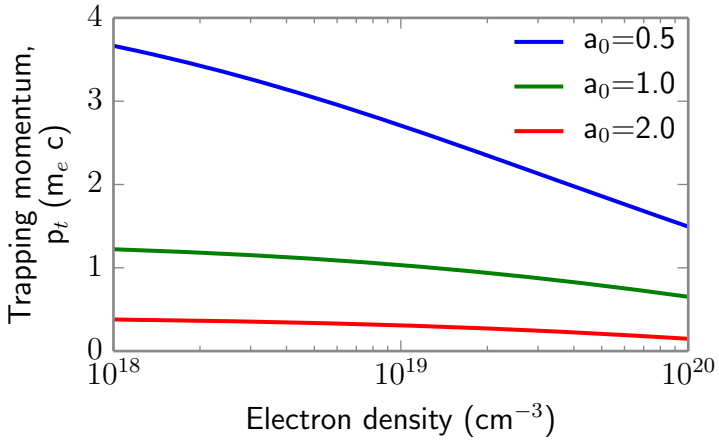


**Figure 2.3. – Effect of laser intensity and plasma density on electron trapping.** A higher laser intensity drives a larger density amplitude plasma wave, allowing electrons with a lower initial momentum to become trapped and accelerated. A higher background plasma density slows down the laser pulse and hence also the trailing plasma wave. The lower plasma wave velocity facilitates electron trapping. The dependence of the plasma wave velocity on the laser intensity dependence is not considered (see main text and Schroeder et al. [2011]).

An electron will become trapped if it has at least reached the velocity of the plasma wave ($\gamma \geq \gamma_p$) at the density peaks of the plasma wave. From this consideration a minimum trapping momentum can be derived [Schroeder et al. 2006]:

$$p_t = \beta_p \gamma_p (1 - \gamma_p \phi_{\min}) - \gamma_p \sqrt{(1 - \gamma_p \phi_{\min})^2 - 1}, \tag{2.25}$$

The lower the minimum trapping momentum, the easier it is for plasma electrons to become trapped by the plasma wave. The trapping threshold can be lowered by decreasing the plasma wave velocity or decreasing the minimum of the electric potential of the wave. The plasma wave velocity is approximately equal to the laser group velocity ($\gamma_p \simeq \gamma_g$) which in turn depends on the plasma density (see equation 2.13). However, the approximation of the plasma wave velocity becomes incorrect for $a_0 \geq 1$. For such high laser intensities the group velocity of the laser pulse *increases*, whereas the plasma wave velocity *decreases* Schroeder et al. [2011] [vi]. The minimum potential depends on the laser intensity through equations 2.20 and 2.23. These dependencies can be seen in figure 2.3.

[vi] For a laser intensity of $a_0 = 2$ and a plasma density $4.4 \times 10^{18}\text{cm}^{-3}$, $\gamma_p \sim 0.9 \cdot \omega_L/\omega_p$ and $\gamma_g \sim 1.2 \cdot \omega_L/\omega_p$. This difference becomes more pronounced with distance from the laser pulse (trailing wakefield buckets slow down more than leading buckets).

An electron trapped by the plasma wake will have passed through the laser and gained energy as it travelled through the plasma wave. When it reaches the rear of the first plasma density peak, it has gained a velocity larger than the plasma wave and is injected into the wake back towards the laser. Such injection is also termed "longitudinal self-injection". Electrons can also be trapped transversely as will be discussed later in the chapter.

### Beam loading

By balancing the energy in the fields of the plasma wake with $N$ particles that travel through these fields, an estimate can be made for the maximum number of electrons that can be "loaded" into the wakefield. The loaded electrons cancel the accelerating electric field and injection stops, defining the beam loading limit. The number of electrons at beam loading is given by [Lu et al. 2007]:

$$N \approx 2.5 \times 10^9 \frac{\lambda_0[\mu\mathrm{m}]}{0.8} \sqrt{\frac{P[\mathrm{TW}]}{100}}. \tag{2.26}$$

For the laser used for this thesis, this estimate gives an upper limit of $\sim 2$ nC of charge that the wake field can support.

## 2.5. Electron acceleration

In section 2.3 the accelerating fields that result from the stimulated plasma wave was discussed. The topics of this section are the longitudinal acceleration and the transverse focusing fields of the plasma wave.

Figure 2.4 shows possible orbits within the potential of a plasma wave behind an intense laser pulse. A trapped orbit (for example orbit '1' in the plot), generally has two solutions for a particular energy. The solutions for a normalised momentum of 250 are illustrated by two red dots in the figure. A given electron energy can be reached during acceleration (left-hand dot), or, after reaching the peak energy at the top of the orbit (dephasing point), during deceleration or dephasing (right-hand dot).

### 2.5.1. Acceleration limits

Laser diffraction
Laser depletion
Electron dephasing

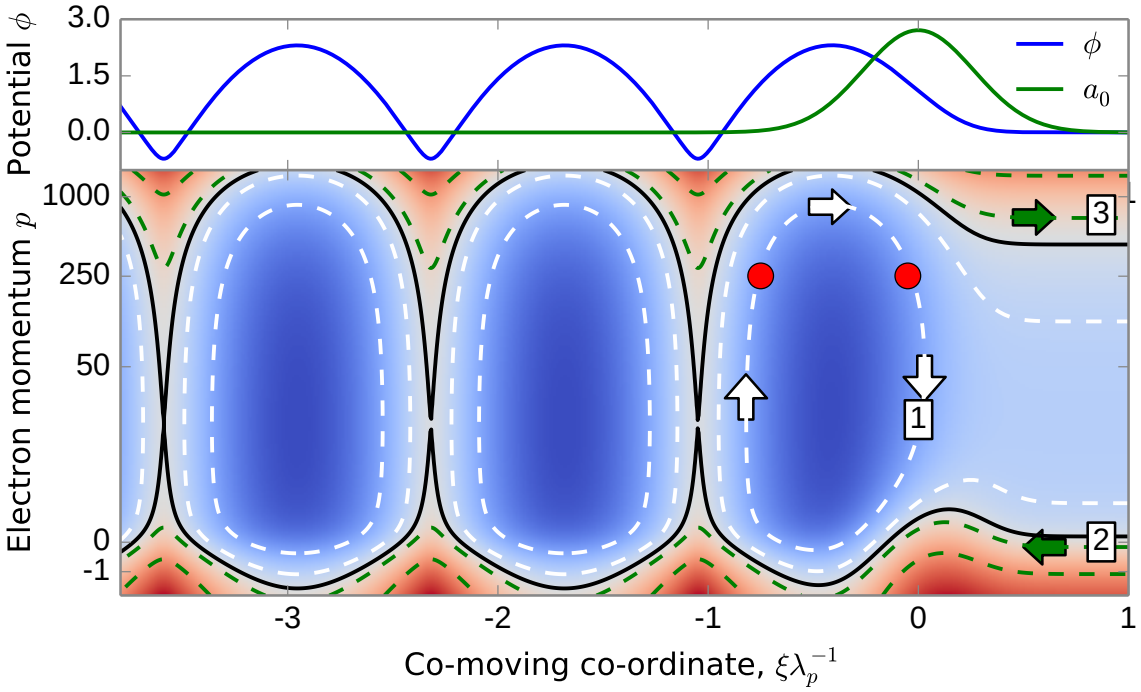


**Figure 2.4. – Phase space of a laser-driven non-linear plasma wave.** Top panel: A laser pulse (green line) excites a plasma wave with a periodic electric potential (blue line). The laser and plasma parameters are the same as in figure 2.2. Bottom panel: Contour lines of constant total energy show possible electron orbits within the potential of the plasma wave. The separatrix (black line) separates the trapped (white) from the untrapped orbits (green). Trapped orbits (1) show an acceleration (white 'up' arrow) as well as a deceleration after the dephasing length (white 'down' arrow). The red dots show two points with the same energy but at different positions within the plasma wave. The untrapped trajectories show an oscillating electron momentum constituting the plasma wave (2) or very high energy electrons which overtake the wake (3).

### Laser diffraction

The cross-sectional size of a freely propagating Gaussian laser beam will have a minimum, called the beam waist $w_0$. On either side of the waist, the beam size will increase due to diffraction according to:

$$w(z) = w_0\sqrt{1+\left(\frac{z}{z_R}\right)^2} \qquad \text{where} \qquad z_R = \frac{\pi w_0^2}{\lambda}. \tag{2.27}$$

The parameter $z_R$ is called the Rayleigh length and gives the distance after which the beam cross-sectional area has doubled. Sometimes the confocal parameter ($b = 2z_R$) is used to describe the distance around a waist (one Rayleigh length either side of the beam focus) in which the intensity is within 50% of the maximum value achieved in focus. To achieve the high intensities required to drive a non-linear plasma wakefield, a typical laser beam has to be focused down to a tens-of-micrometers spot size. For the experiments in this thesis, a focal spot size of $\sim$20 µm was chosen, leading to a confocal parameter of about 3 mm. To maintain a high intensity for a longer interaction distance requires either external guiding in form of a preformed density channel (for example by igniting a high-voltage discharge several nanoseconds before laser arrival, see Karsch et al. [2007]) or by ensuring the laser power is sufficient for self-focusing (see section 2.2.1).

### Laser depletion

To drive the charge separation necessary for a plasma wakefield, the laser loses energy. The wakefield amplitude will therefore continuously decrease. Eventually the laser will have lost a substantial fraction of its energy and will no longer fulfil the self-focusing condition and also diffract away, ultimately ending the acceleration process. An estimate of the length until the laser has lost all of its energy to the plasma can be made by equating the field energy of the plasma wakefield over the depletion length with the energy initially in the laser. For a square temporal pulse, Esarey et al. [2009] obtains the following expression:

$$L_{pd} \approx \frac{\lambda_p^3}{\lambda^2} \times \begin{cases} 2/a_0^2 & \text{for } a_0^2 \ll 1 \\ (\sqrt{2}/\pi)a_0 & \text{for } a_0^2 \gg 1. \end{cases} \tag{2.28}$$

Energy depletion is less severe for lower densities (longer $\lambda_p$ for lower $n_e$).

### Electron dephasing

Trapped electrons typically already have relativistic velocities ($v \to c$) when they first become trapped, whereas the laser pulse and its trailing wakefield propagate at $v_g < c$ (see equation 2.13). The trapped electrons therefore slowly overtake the wake structure and leave the accelerating part of the wakefield. The **dephasing length** is defined as the acceleration length after which electrons reach the zero-crossing of the longitudinal electric field. At this point they have attained their highest kinetic energy and begin to be decelerated by the wake field. An estimate of the dephasing length gives [Esarey et al. 2009]:

$$\Delta v L_d/c = \lambda_p/2$$

$$\Rightarrow L_d \approx \frac{\lambda_p^3}{\lambda^2} \propto n_e^{-3/2}, \tag{2.29}$$

where $\Delta v = (c - v_g)$ represents the difference in velocity of the wake field and the trapped electrons. The above approximation leads to a dephasing length of 3.5 mm for a plasma density of 6 $\times 10^{18}\text{cm}^{-3}$ with a Ti:Sa driver laser.

### 2.5.2. Laser-heating of the electron beam

As discussed in the previous section, the injected electron bunch travels faster than the laser beam and the wakefield. Depending on the laser pulse duration and the interaction length, the injected bunch will at some stage catch up to the back of the laser beam. Here the electrons interact with the laser electric field directly in the polarisation direction (first-order interaction), or with the gradient of the intensity in both transverse directions (second-order motion, see ponderomotive force in section 2.1.3). The electrons are deflected from the axis which causes an increase in beam emittance [Mangles et al. 2006]. This "beam heating" is expected to be more severe in the direction of the laser polarisation but should also be evident perpendicular to it.

## 2.6. Transition to vacuum

The geometry of the gas cell used in the experiments of this thesis results in a mm-scale plasma to vacuum transition at the exit. The effect this transition has on the electron beam envelope can be investigated using an analytical model. While the beam is trapped and accelerated in the plasma wakefield, the strong linear focusing forces keep the beam size small and the normalised emittance remains constant. The evolution of the rms electron beam envelope, $x(s)$, in an ion channel (as in the plasma blow-out regime) neglecting space charge and acceleration is given by (Reiser [2008]):

$$x(s)'' + k_\beta^2 x(s) - \varepsilon^2/x(s)^3 = 0. \tag{2.30}$$

Here $k_\beta$ is the betatron wavenumber. In an ion channel $k_\beta = k_p/\sqrt{2\gamma}$ (Esarey et al. [2002]), where $k_p$ is the plasma wavenumber which depends on the density of the background electrons, $n_e$. The dynamics of the beam envelope are therefore determined by the plasma density and the beam emittance. When the focusing force

of the plasma balances the expansion due to the beam emittance, the size of the beam envelope remains constant with a matched size given by:

$$x_m = \sqrt{\varepsilon / k_\beta}. \tag{2.31}$$

For the parameters in the experiments for this thesis the matched beam size is $x_m \lesssim 0.2\,\mu\text{m}$ and the betatron wavelength is $\sim$0.5 mm.

## 2.7. The bubble regime

The complete lack of electrons behind a driver laser (or electron beam) is referred to as the blowout, bubble, or cavitation regime. By balancing the ponderomotive force of the laser and the restoring force of the ion channel, a relation between the blowout radius, $R$, and the laser intensity is found:

$$k_p w_0 \sim k_p R = \sqrt{a_0}, \tag{2.32}$$

where the approximation $w_0 \sim R$ is confirmed by PIC simulations [Lu et al. 2007]. Given the laser intensity and beam size satisfy equation 2.32, all electrons will be ejected from the laser axis and leave behind the plasma ions. The trajectory of plasma electrons in the fields of the remaining ion channel have been studied by Kostyukov et al. [2010]. The analytical model of the fields inside the bubble assumes a spherical ion cavity. Additional fields such as the laser fields (trapping occurs well behind the laser), the beam-loading fields of already-trapped electrons, and the fields of the electron density spike at the back of the bubble are neglected.

Figure 2.5 shows the numerical solution for the analytical model for three test electrons. As the bubble is following behind the laser pulse, a stationary plasma electron passes from right to left in terms of the co-moving coordinate $\xi$. Trajectories outside of the bubble are not altered by the local bubble fields (red trajectory). An electron which passes through the bubble close to the laser axis (green trajectory) gains negative momentum $p_z$ in the region $\xi > 0$ and decreases the chances of it being trapped by the time it reaches the back of the bubble. The chances for injection are higher if an electron enters the bubble with larger $\rho$ (blue trajectory). In this case, the electron spends less time in the region where $\xi > 0$ being accelerated towards negative $\xi$.

The model here attempts to describe transverse injection into the bubble. In section 2.4 longitudinal injection was discussed. Both regimes have been observed and in general always occur together in self-injection experiments [Corde et al. 2013]. Whereas longitudinal injection occurs early and only for a short time in the laser-plasma interaction, once the laser undergoes self-focusing transverse injection sets in for much longer periods and hence many more electrons are injected. For this

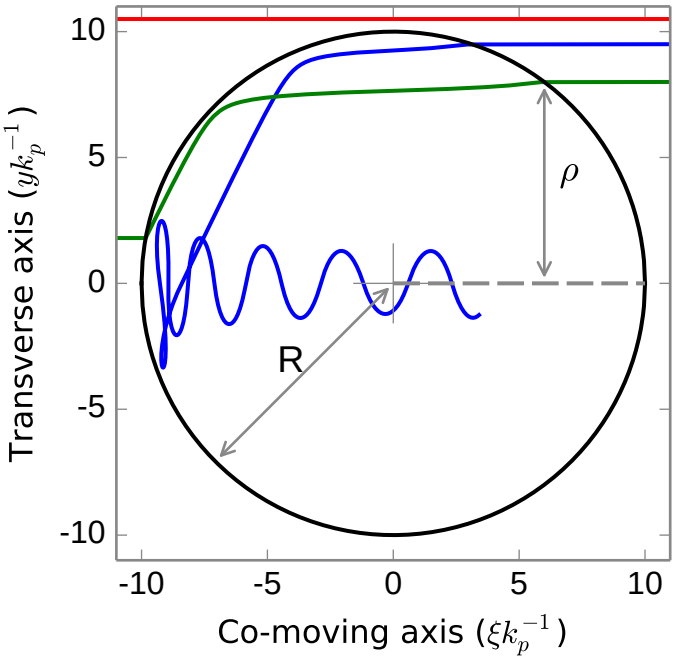


**Figure 2.5. – Analytical model for electron injection into a plasma bubble.** The plasma bubble is modelled as a perfect sphere (radius $R$), completely void of electrons and co-propagating with the laser pulse. Outside the bubble a neutral plasma means that electrons are not deviated (red trajectory, $r > R$). Once an electron enters the bubble its trajectory is changed and can even become trapped and accelerated (blue trajectory). This only occurs for electrons with an entry point $\rho \sim R$ near the top of the bubble sheath (high density layer of electrons forming the bubble sphere).

reason, Corde et al. [2013] suspect that for plasma lengths >2 mm transversely injected electrons dominate over longitudinal ones. Before the laser self-focuses, the laser spot radius is still relatively large, and $a_0$ is still low. Hence the transverse ponderomotive force is smaller and electrons are not deviated as much from the propagation axis. Longitudinally injected electrons are therefore also expected to have a smaller emittance than those trapped with transverse injection.

## 2.8. Summary

Here the concepts relevant to the experimental results in chapter 6 are discussed.

### Scaling of the laser beam size in the plasma

Self-focusing of the laser beam relies on its interaction with the local plasma electrons. It follows that once the laser has expelled all electrons as in the bubble regime, no further self-focusing of the beam can occur. Therefore the condition to reach the bubble regime, equation 2.32, should also give a lower limit to the laser beam size after self-focusing. Through PIC simulations, Lu et al. [2007] found the best guiding of the laser spot with a slight modification to the blowout-condition:

$$k_p w_0 = 2\sqrt{a_0} \tag{2.33}$$

Without knowing exactly how the actual beam size will change during propagation in the plasma [vii], above the critical power the laser beam should contract until condition 2.33 is met. As the beam contracts $w_0$ becomes smaller and $a_0$ correspondingly larger [viii]. Hence equation 2.33 can be rewritten in terms of an evolving beam size and intensity with propagation distance $z$:

$$\begin{aligned} w_0(z) &= \frac{\lambda_p}{\pi}\sqrt{a_0(z)} \\ &= \frac{\lambda_p}{\pi}\sqrt{\frac{w_0(0)a_0(0)}{w_0(z)}} \\ &= \left(\frac{\lambda_p}{\pi}\sqrt{w_0(0)a_0(0)}\right)^{2/3} \\ &\sim n_e^{-1/3}. \end{aligned} \tag{2.34}$$

This relates the laser beam size at plasma blowout (no further self-focusing possible) to the plasma density and the initial laser beam size and intensity before self-focusing. The final relation was obtained by using equation 2.6 to rewrite the plasma wavelength in terms of the plasma density.

### Scaling of the electron beam size

A simple scaling for the injected beam size can be found by making two assumptions:

[vii] Esarey et al. [2009] gives an expression for the beam size as $w(z) = w(0)\left(1 + \frac{P_C}{P}\right) z_R$. However, this relation is valid for a laser strength parameter $a_0 << 1$.

[viii] The normalised laser intensity scales as $a_0 \sim \sqrt{(I)}$ (see equation 2.4). For a constant beam energy and pulse length the intensity scales as $I \sim 1/w_0^2$ giving $a_0 \sim 1/w_0$ and hence $a_0(z)/a_0 = w_0/w_0(z)$.

1. The blowout radius, $r_b$, scales with the laser spot size $w_0$.

2. The injected beam size, $\sigma$, scales with the blowout radius.

The first assumption was predicted by Lu et al. [2007] and further supported by PIC simulations Martins et al. [2010]. The PIC simulations agree well with the assumption that $w_0 \sim r_b$ at injection as well as the entire acceleration length (itself limited by the dephasing and pump depletion).

The second assumption of a proportional scaling between wake radius and injected beam size was also observed in simulations by Lu et al. [2007] and furthermore, has been confirmed experimentally. By measuring the angularly resolved energy spectra of the electron beam [Matsuoka et al. 2014] a correspondence between the wake radius and the radius of the trapped electrons was shown. Further support for the assumption is given by the analytical model discussed in section 2.7 which shows that the injected electrons originate from the sheath electrons at the bubble radius.

From the above assumptions it follows that $\sigma \sim w_0(z)$ and combined with 2.34 it follows that $\sigma \sim n_e^{-1/3}$. The transverse momentum at injection scales as $\theta \sim a_0$ [Lu et al. 2007; Thomas 2010]. In section 2.2.1 it was shown that $a_0(z) \sim 1/w_0(z)$ which leads to the following scalings for the electron beam source parameters:

$$\boxed{\sigma \sim w_0 \sim n_e^{-1/3}} \tag{2.35a}$$

$$\boxed{\theta \sim a_0 \sim n_e^{1/3}} \tag{2.35b}$$

The emittance can be calculated at the waist of the electron beam as $\epsilon \sim \sigma\theta$. It follows from the above approximate scalings that the emittance should therefore not (or only weakly) scale with the plasma density.

# 3. Electron beam transport and characterisation

The analysis of how a charged particle beam will move after it has exited the plasma accelerator is done using the Lorentz force. The analysis presented below is based on those given in [Wille 2001; Wollnik 1987]. Additionally to these, there are many more resources covering the derivation of the basic equations of motion in a beamline, in particular the CERN Accelerator School (CAS) provides much material. Here only the solutions and the associated assumptions will be presented.

## 3.1. Charged particle motion in a magnetic field

Lorentz force
Multipole expansion
Quadrupole field
Equation of motion

---

A charged particle moving in electric and magnetic fields experiences the **Lorentz force**:

$$\vec{F} = q(\vec{E} + \vec{v} \times \vec{B}),$$

where $q$ is the particle charge, $\vec{E}$ and $\vec{B}$ are the electric and magnetic fields, and $\vec{v}$ is the particle velocity. For relativistic particle velocities, the force exerted by both field types are equal if $\vec{E} = c\vec{B}$. To match the force exerted by a 1 T magnetic field (readily achieved using rare-earth magnets), an electric field with $\sim 10^8$ V/m is required, beyond the fields achieved in current RF accelerator technology. This limitation explains why electric fields are generally only used to guide low energy particles. The remainder of this chapter will only consider focusing with magnetic fields.

The coordinate system that will be used is shown in figure 3.1, it moves and rotates along with the design trajectory (often called "orbit") along the beamline. Assuming that the orbit trajectory can be realised by employing some arrangement of fields, the co-moving system allows the analysis of the transverse deviations of a particle

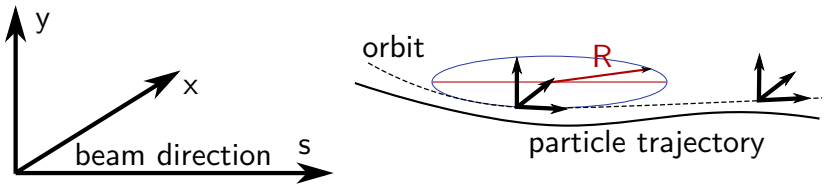


**Figure 3.1.** – The coordinate system is co-moving with the orbit (design trajectory) with $s$ pointing in the direction of motion.

or beam from the orbit. Depending on each particle's initial conditions, its path will be slightly different. The main goal of beam optics is to guide particles as closely as possible along the orbit. The particle velocity is therefore almost exclusively along $s$ with only small transverse values, $\vec{v} \sim (0, 0, v_s)$. Furthermore it is usually the case that only transverse magnetic fields are present (only these can be used to steer the beam) $\vec{B} = (B_x, B_y, 0)$. The problem can be simplified by only treating the motion in $x$ and noting that the results will be identical for $y$. For a particle moving in a uniform magnetic field along $y$, the Lorentz force acts as the centripetal force which makes the particle move on a circle of radius $R$ given by:

$$\begin{aligned} F_x &= -qvB_y = \gamma m_0 v^2/R \\ \Rightarrow -\frac{q}{p}B_y &= \frac{1}{R}, \end{aligned} \tag{3.1}$$

where $p = \gamma m_0 v$ is the relativistic momentum, and $\gamma$ is the Lorentz factor. Generalising to a non-uniform magnetic field, $B_y = B_y(x, s)$ is a function of $x$ and $s$ as the particle moves in the field.[i] It is helpful to expand the magnetic field in a Taylor series around $x = 0$ and analyse the effect of individual terms (called multi poles).

$$B_y = \quad B_y(0) + \quad \left.\frac{dB_y}{dx}\right|_0 x + \quad \frac{1}{2!}\left.\frac{d^2B_y}{dx^2}\right|_0 x^2 + \quad \frac{1}{3!}\left.\frac{d^3B_y}{dx^3}\right|_0 x^3 + \ldots$$

[i] For simplicity the notation $B_y$ contains the functional dependence on $x$ and $s$ implicitly.

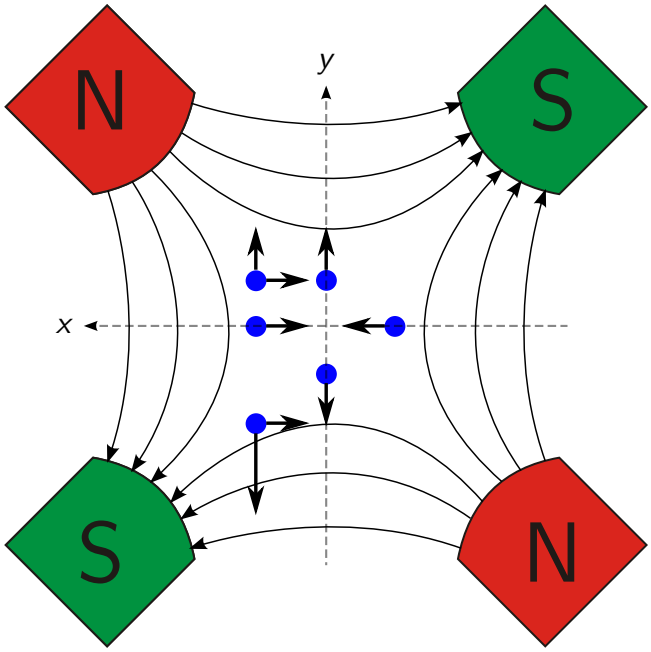


**Figure 3.2. – Magnetic quadrupole field.** Test electrons (blue) travelling into the page and the forces they experience. The quadrupole field is focusing in one plane and defocusing in the other, leading to a line focus at the focal length after the lens. The magnitude of the forces is linearly proportional to the particle distance from the axis (magnitude is indicated by arrow length).

multiplying by $-q/p$ results in:

$$\begin{aligned}
\frac{-q}{p}B_y = \quad & \frac{-q}{p}B_y(0) + \frac{-q}{p}\left.\frac{dB_y}{dx}\right|_0 x + \frac{-q}{p}\frac{1}{2!}\left.\frac{d^2B_y}{dx^2}\right|_0 x^2 + \frac{-q}{p}\frac{1}{3!}\left.\frac{d^3B_y}{dx^3}\right|_0 x^3 + \dots \\
= \quad & \frac{1}{R} + kx + \frac{1}{2!}mx^2 + \frac{1}{3!}ox^3 + \dots \qquad (3.2) \\
= \quad & \text{dipole} + \text{quadrupole} + \text{sextupole} + \text{octupole} + \dots
\end{aligned}$$

The first term gives the curvature $(1/R)$ of the electron in the constant part of the field, the other terms also express a "strength" of the field components but with a higher-order dependence on $x$. The names of the terms of the Taylor expansion refer to the number of magnetic poles necessary to generate a magnetic field with the corresponding dependence with $x$. For example a quadrupole requires four magnetic poles to generate a magnetic field with linear dependence on $x$ (fig. 3.2). To

generate orders higher than quadrupole also inevitably requires magnetic fields that couple the transverse planes (the field component $B_y$ depends on both the $x$ *and* $y$ position). In linear beam optics only drift sections, dipole, and quadrupole magnets are considered. In this simplified model the **transverse planes are uncoupled**, which allows the beam dynamics in the transverse planes to be treated independently. The validity of using linear beam optics in a given experiment depends on the purity of the dipole and quadrupole fields over the size of the beam within the beamline elements. Any terms above the quadrupole are lumped together to be called lens errors or higher-order magnetic field components (HOMFCs) in this thesis[ii]. The effect of HOMFCs on a particle beam is simulated for measured values of the lens magnetic fields setup in section 4.3.1. In section 3.3.2 the effect of coupling of the axes on the electron beam quality is discussed. The remainder of this section deals with linear beam optics.

For an ultra-relativistic electron, $q/p \approx \frac{0.3}{E\,[\mathrm{GeV}]}$. Hence there are convenient expressions for the dipole and quadrupole strengths:

$$1/R \approx \frac{0.3}{E\,[\mathrm{GeV}]} B$$

$$k \approx \frac{0.3}{E\,[\mathrm{GeV}]} \left.\frac{dB}{dx}\right|_0 \tag{3.3}$$

Using the field expansion for the magnetic field, the equations of motion can be derived with the Lorentz force. The details can be found, for example in [Wille 2001], the main steps and assumptions are:

- Get an expression for the position vector $\vec{r}$ of a particle in terms of the coordinates of the co-moving and rotating frame that is following the orbit.
- Cast the Lorentz equation into the orbit coordinates.
- Postulate that the magnetic field $\vec{B} = (0, B_y, 0)$ only has a $y$ component.
- The particles are already ultra-relativistic so that their longitudinal acceleration can be neglected, $\ddot{s} \approx 0$.
- The energy spread $\frac{\Delta p}{p}$ is small.
- Multipoles higher than quadrupole are neglected.

[ii] Higher multipoles can be used to make special corrections to the beam. For example, a sextupole field can be used after a quadrupole to compensate chromatic focusing (focal length increases with electron energy).

The final result is:

$$\boxed{x''(s) + \left(\frac{1}{R^2(s)} - k(s)\right) x(s) = \frac{1}{R(s)} \frac{\Delta p}{p}}, \tag{3.4}$$

and is sometimes referred to as Hill's equation. Note that this equation is in the coordinates of the co-moving system of the orbit. The actual trajectory relative to a stationary system can be very complicated. After the orbit trajectory is defined, equation (3.4) is used to study the transverse dynamics of the beam.

In solving equation (3.4) for drift and quadrupole beamline elements, it is convenient to use matrix equations to relate the initial to the final particle parameters. A particle is transferred through a beamline element (either a drift or a quadrupole lens) using

$$\vec{x} = \boldsymbol{M}\vec{x}_0. \tag{3.5}$$

Here $\vec{x} = (x, x')$ is a vector containing the particle position $x$ and angle $x'$ relative to the $s$ axis after the beamline element, $\vec{x}_0$ contains the corresponding initial values, and $\boldsymbol{M}$ is the **transfer matrix** for the beamline element which describes its action on the particle. For a sequence of beamline elements the transfer matrices are applied one after the other on the particle as in $\vec{x} = \boldsymbol{M_n} \cdot \boldsymbol{M_{n-1}} \cdot \ldots \boldsymbol{M_1} \cdot \vec{x_0}$. The elements of $\boldsymbol{M}$ for different situations will be determined in the next sections.

### 3.1.1. Free drift

In a magnet free region equation 3.4 reduces to $x'' = 0$. Integrating twice gives

$$x' = c_1,$$

$$x = c_1 s + c_2.$$

For $s = 0$ (no drift), the $x$ coordinates remain unchanged ($\vec{x} = \vec{x_0}$). Using these initial conditions and inserting them into the solution above gives the following transfer matrix for a drift of length $d$:

$$\boldsymbol{M}_{\text{drift}} = \begin{pmatrix} 1 & d \\ 0 & 1 \end{pmatrix} \tag{3.6}$$

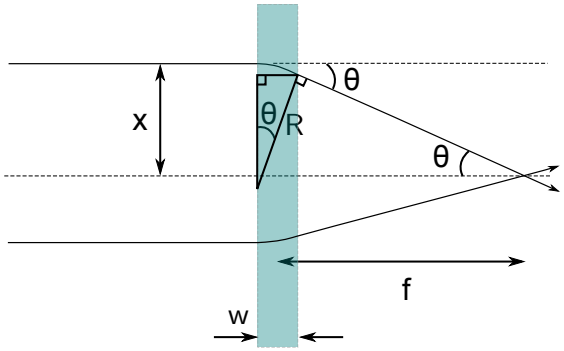


**Figure 3.3.** – Focal length of a quadrupole field in the thin lens approximation.

## 3.1.2. Quadrupole field

### Thin lens approximation

Previously it was shown that an electron in a uniform magnetic field moves on a circle of radius $R$. A quadrupole field introduces a deflection proportional to the offset from its centre, the basic property of a focusing lens in optics. As a first step the action of a thin lens will be discussed by assuming a thin lens of length $w$, and a pure quadrupole field. The second condition ensures that the magnetic field gradient is constant with $x$ which means that $B(x) = dB/dx \cdot x$. The bending radius of a particle in a pure quadrupole field is then dependent on $x$ and is given by:

$$\frac{1}{R(x)} = -\frac{q}{p}B(x) = kx. \tag{3.7}$$

Using the variables defined in figure 3.3, the focal length is given by

$$\begin{aligned} \theta &\approx \frac{w}{R} \\ &= kxw. \end{aligned} \tag{3.8}$$

Because $w$ is short, the position of the particle at the end of the lens can be approximated to be the same as at the beginning. As the particle's transverse position $x$ is considered to be constant as it passes through the lens, $B(x)$ is also constant and hence $R$ stays constant. This results in $\theta \approx x/f$. Combining this with (3.8) gives

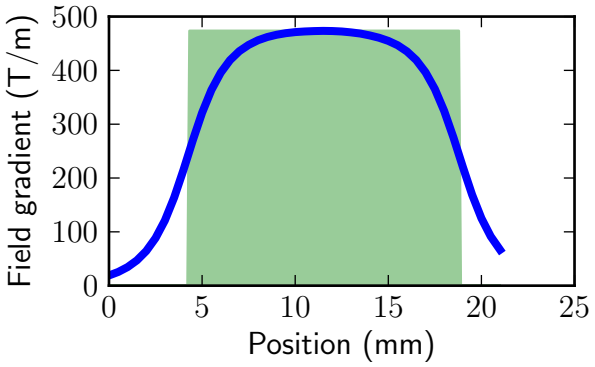


**Figure 3.4. – Hard-edge model.** The magnetic field of a 15 mm long quadrupole (blue) extends past its physical length. The measured gradient for this lens can be approximated by a constant gradient (maximum of the measured field gradient) of length 14.55 mm (green). If the field is measured further to either side of the lens, the length of the hard-edge model lens approaches the physical length of the lens.

$$f = \frac{1}{kw} \tag{3.9}$$

$$\approx \frac{E\,[\mathrm{GeV}]}{0.3 \cdot g \cdot w}. \tag{3.10}$$

$E, g$, and $w$ represent the electron energy in GeV, the magnetic field gradient in T/m, and $w$ the lens length in m. The second equation is a handy approximation of the thin lens focal length and is obtained by inserting equation (3.3). As an example case, a 300 MeV beam passing through a 25 mm, 500 T/m lens results in a focal length of $f = 8$ cm. The focal length obtained by solving the equations of motion for a thick lens is 8.4 cm (equation (3.19)).

### Quadrupole transfer matrix

It was previously stated that for a pure quadrupole field the transverse planes are uncoupled, it therefore suffices to just look at one of the transverse planes. To calculate a beamline it is convenient to use the **hard-edge model** where the fields are zero in drift regions and have a constant value within the physical extent of the magnets (as illustrated in fig. 3.4). For a particle with the nominal momentum (i.e. $\Delta p/p_0 = 0$) in a pure quadrupole field, equation (3.4) simplifies to

$$x''(s) - k(s)x(s) = 0. \tag{3.11}$$

The solutions depend on the sign of $k$. Figure 3.2 shows a quadrupole that is focusing for electrons along the $x$-axis. As both $q$ and $dB_y/dx$ are negative, $k$ is also negative and corresponds to the focusing plane. For positively charged particles, $q$ and therefore also $k$, change sign and the quadrupole field is defocusing. For the focusing case ($k < 0$) the solution is

$$x(s) = A\cos(\sqrt{|k|}s) + B\sin(\sqrt{|k|}s),$$
$$x'(s) = -\sqrt{|k|}A\sin(\sqrt{|k|}s) + \sqrt{|k|}B\cos(\sqrt{|k|}s).$$

The constants of integration $A$ and $B$ are determined by the initial conditions, leading to

$$x(s) = x_0\cos(\sqrt{|k|}s) + \frac{x_0'}{\sqrt{|k|}}\sin(\sqrt{|k|}s)$$
$$x'(s) = -\sqrt{|k|}x_0\sin(\sqrt{|k|}s) + x_0'\cos(\sqrt{|k|}s), \tag{3.12}$$

where $(x_0, x_0')$ are the initial position and angle values of the particle. The solution relates the initial values of the particle at the entrance of the quadrupole to those after it has travelled distance $s$ inside the magnet. In transfer matrix notation this is represented as

$$\boldsymbol{M}_{QF} = \begin{pmatrix} \cos(\sqrt{|k|}s) & \frac{1}{\sqrt{|k|}}\sin(\sqrt{|k|}s) \\ -\sqrt{|k|}\sin(\sqrt{|k|}s) & \cos(\sqrt{|k|}s) \end{pmatrix} \quad \text{for } k < 0 \text{ (\textbf{focusing})}, \tag{3.13a}$$

$$\overset{s\to 0}{\approx} \begin{pmatrix} 1 & 0 \\ -|k|s & 0 \end{pmatrix} = \begin{pmatrix} 1 & 0 \\ -1/f & 1 \end{pmatrix} \quad \text{thin lens approximation,} \tag{3.13b}$$

$$\boldsymbol{M}_{QD} = \begin{pmatrix} \cosh(\sqrt{k}s) & \frac{1}{\sqrt{k}}\sinh(\sqrt{k}s) \\ \sqrt{k}\sinh(\sqrt{k}s) & \cosh(\sqrt{k}s) \end{pmatrix} \quad \text{for } k > 0 \text{ (\textbf{defocusing})}, \tag{3.14}$$

The thin lens transfer matrix (3.13b) has a focal length as was obtained previously in equation (3.10), if the lens length $w$ is substituted for $s$. The defocusing case is the same except for a change of sign ($f < 0$ for a defocusing lens). These matrices can be abbreviated by introducing a shorthand notation for the trigonometric functions

to get

$$\boldsymbol{M}_{QF} = \begin{pmatrix} c_x & s_x \\ -ks_x & c_x \end{pmatrix}, \tag{3.15a}$$

$$\boldsymbol{M}_{QD} = \begin{pmatrix} c_y & s_y \\ ks_y & c_y \end{pmatrix}, \tag{3.15b}$$

$$c_x = \cos(\sqrt{|k|}s), \quad s_x = \frac{1}{\sqrt{|k|}}\sin(\sqrt{|k|}s),$$

$$c_y = \cosh(\sqrt{k}s), \quad s_y = \frac{1}{\sqrt{|k|}}\sinh(\sqrt{k}s).$$

### 3.1.3. Focal length of a "thick" quadrupole lens

Each element of a transfer matrix has a physical significance as it reveals how a final particle coordinate depends on an incoming particle coordinate. With this in mind the transfer equation 3.5 can be written as

$$\begin{pmatrix} x \\ x' \end{pmatrix} = \begin{pmatrix} (x|x_0) & (x|x_0') \\ (x'|x_0) & (x'|x_0') \end{pmatrix} \begin{pmatrix} x_0 \\ x_0' \end{pmatrix}. \tag{3.16}$$

Here the element $(x|x_0)$ for example describes how the position $x$ after the transfer matrix depends on the incoming particle position $x_0$. It also becomes clear that $(x'|x_0)$ should have to do with the refractive power or focal length of a device. This notation is convenient to obtain the focal length of a thick quadrupole lens.

Figure 3.5 shows a parallel ray passing through a thick lens which is bent and crosses the axis at a distance $d$ behind the end of the lens. The transfer matrix of the system starting at the lens entrance and ending where the particle crosses the axis is

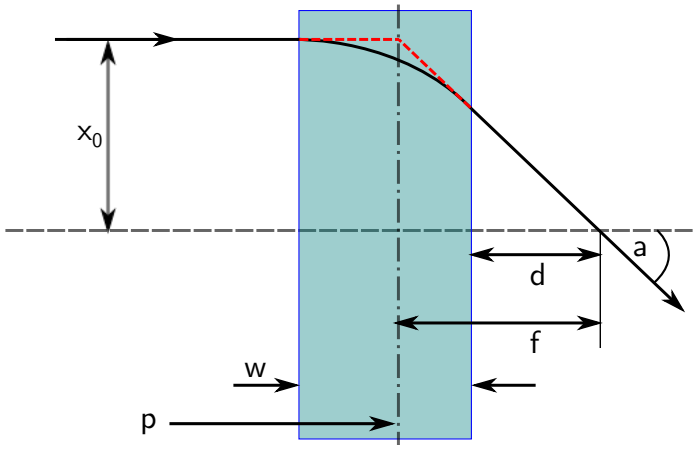


**Figure 3.5. – Determining the focal length of a thick quadrupole.** The focal length, $f$, is defined relative to the principal plane, $p$, which itself is determined by the intersection of the incoming and outgoing rays.

$$\begin{aligned}\boldsymbol{M} &= \boldsymbol{M}_{\text{drift}} \cdot \boldsymbol{M}_{QF} \\ &= \begin{pmatrix} 1 & d \\ 0 & 1 \end{pmatrix} \cdot \begin{pmatrix} c_x & s_x \\ -ks_x & c_x \end{pmatrix} \\ &= \begin{pmatrix} c_x - dks_x & s_x + dc_x \\ -ks_x & c_x \end{pmatrix}. \end{aligned} \tag{3.17}$$

If the $(x|x_0)$ element of $\boldsymbol{M}$ is set to zero, then the position of the outgoing rays have no dependence on their incoming position but only on their angle. Incoming parallel rays are therefore focused to a common point after drift $d$; this defines the focal plane. From these considerations it follows that $c_x - dks_x = 0$, which leads to

$$d = c_x/ks_x. \tag{3.18}$$

For the standard case (300 MeV electrons, 25 mm lens with 500 T/m field gradient), the focal plane lies at $d = 7.1$ cm after the exit of the lens. The focal length can be found by transferring an incoming ray parallel to the optical axis $\vec{x_0} = (x_0, 0)$ through the system transfer matrix (3.17) which results in an outgoing vector

$$\vec{x} = ((c_x - dks_x)x_0, -ks_x x_0) = (0, -ks_x x_0).$$

From figure 3.5 the focal length is given by

$$f = -\frac{x_0}{\tan(x')} = \frac{x_0}{\tan(ks_x x_0)}, \tag{3.19}$$

and also defines the principal plane of the lens (see fig. 3.5). The focal length using this equation and the standard case gives $f = 8.4$ cm, which compares quite well with the thin lens value of 8 cm obtained previously with equation 3.10. The position of the principal plane from the exit of the lens for a paraxial ray ($x_0$ small, $f \to 1/ks_x$) is

$$\begin{aligned} p = d - f = \frac{c_x}{ks_x} - \frac{1}{ks_x} &= k^{-1}\left(\frac{c_x}{s_x} - \frac{1}{s_x}\right) \\ &= -\frac{1}{\sqrt{k}}\tan(\sqrt{k}s/2). \end{aligned} \tag{3.20}$$

From equation 3.20 it follows that the principal plane lies in the centre of the lens ($p = -s/2$) when the argument of the tangent becomes small. For example, for a 25 mm long lens with a field gradient of 500 T/m, $p = -12.8$ mm, very close to the physical centre of the lens at -12.5 mm. It is therefore a reasonable first approximation to use thin lens analysis with the principal planes in the centre of each lens for the devices used in this thesis.

### A note on aberrations

In equation 3.19 the focal length depends on the incoming ray position $x_0$, i.e. a **spherical aberration**. In the experiments for this thesis the beam size is on the order of 0.2 mm so that $\tan(x) \to x$ is a valid approximation and the spherical aberration is negligible. As with other aberrations mentioned later, the detrimental effect on beam imaging is greater when the beam is large when it passes through the lens. The focal length also depends on the parameter $k = q/p \cdot dB/dx$ which depends on the beam energy $p$, i.e. a **chromatic aberration**. Higher beam energies have a longer focal length.

It turns out that both effects are negligible for the experimental part of this thesis. The effect of chromatic aberrations is simulated (and concluded to be negligible) in section 4.3.1. The effect of spherical aberrations, although small, is included in the evaluation of the experimental data by using the transfer matrices for thick lenses.

## 3.2. Particle beams

In this section the analysis of single particles is extended to an ensemble, or particle beam. With this formalism the electron beam can be analysed along the beamline without knowing the exact coordinates of all the individual particles. The transfer matrices for beamline elements that were derived in the previous sections can be applied to quantities that describe the beam as a whole.

### 3.2.1. Beam emittance and Courant-Snyder parameters

In the description of beam optics used in this work, only the forces of the electric and magnetic fields of the beamline elements on the particles are considered; Coulomb collisions between individual particles in the beam are neglected. As the forces in the system are therefore conservative, Liouville's theorem is applicable. This theorem states that the volume occupied by a set of particles in the 6D phase space $(x, p_x, y, p_y, s, p_s)$ is constant in time, i.e. the particles in phase space act like an incompressible fluid. Or stated in another way, particles within an enclosed volume will always remain inside it. This second formulation helps to describe the large number of individual particles as a single beam entity by enclosing (some of) the particles of the beam in a meaningful volume called the **phase space ellipsoid**.

In the absence of coupling between the $x, y$ and $s$ dimensions, the constant 6D phase space can be split into three independent 2D phase spaces. By only considering a mono-energetic beam and neglecting magnetic moments higher than quadrupole (which lead to coupling between the $x$ and $y$ dimensions), this separation is useful as the individual phase space emittances are also conserved and are often called **projected emittances**.

Instead of using the position and their momentum variables, more commonly the related set of variables $(x, x', y, y')$ are used. The $x - x'$ plane is often referred to as *trace-space*, and hence the corresponding beam area in this plane the **trace-space or geometric emittance**, $\varepsilon_{tr.}$. The advantage in using the gradients of the trajectories is that for a beam, this dimension describes the beam divergence, a physically more intuitive measure than $p_x$. The disadvantage is that Liouville's theorem is strictly speaking only valid for the $x - p_x$ phase plane. The result is that the geometric emittance is not constant under acceleration. This can be directly seen from $x' = p_x/p_s = p_x/\gamma\beta mc$. To compensate this deficiency, a normalisation with energy is introduced by multiplying the $x'$ plane by $\gamma\beta$ giving $\varepsilon_n = \gamma\beta\varepsilon_{tr.}$. Here, $\varepsilon_n$, is the **normalised emittance** and is constant even if the beam is accelerated.

### Connection between emittance and Courant-Snyder parameters

As usual only the $x$-plane and its momentum is considered, and it is assumed that the energy spread of the beam is zero ($\delta p = 0$). Furthermore, the $1/R^2$ dipole term is neglected as it is usually small compared with the quadrupole strength. Then equation 3.4 becomes:

$$x''(s) - k(s)x(s) = 0. \tag{3.21}$$

A possible solution is $x(s) = \sqrt{\varepsilon\beta(s)}\cos[\psi(s) + \phi]$. Combining $x(s)$ with its derivative $x'(s)$ and eliminating the terms which depend on $\psi$ leads to:

$$\gamma_{CS}(s)x^2(s) + 2\alpha(s)x(s)x'(s) + \beta(s)x'^2(s) = \varepsilon_{tr.}. \tag{3.22}$$

Here $\alpha(s) = -\beta'(s)/2$ and $\gamma_{CS}(s) = (1 + \alpha^2(s))/\beta(s)$. This relation describes the equation of an ellipse in $x - x'$-space with an area of $\pi\varepsilon_{tr.}$. As discussed above, the trace space emittance is a constant of motion as long as the beam is not accelerated. Equation 3.22 can therefore be used to transfer the beam down a beamline with drifts and quadrupole lenses (see the next section). The beta function gives the size of the electron beam via $x(s) = \sqrt{\varepsilon_{tr.}\beta(s)}$ and the angular divergence is given by $x'(s) = \sqrt{\varepsilon_{tr.}\gamma(s)}$. The Courant-Snyder parameter $\alpha$ determines the rotation angle of the phase space ellipse. In focus, there is no correlation between $x$ and $x'$, the beam ellipse is upright ($\alpha = 0$) and the geometric emittance is the product of the beam size and its divergence, $\varepsilon_{tr.} = \pi x x'$.

## 3.2.2. Propagating the Courant-Snyder parameters along a beamline

In the previous section the emittance was introduced. As the emittance is a constant of motion for the particle beam, it can be used to calculate the evolution of the beam through a beamline. Using equation 3.22 together with the transfer-matrix approach (equation 3.5) gives the following equation for the beam size:

$$x(s_1)^2 = \boldsymbol{M}_{11}^2\epsilon\beta(s_0) - 2\boldsymbol{M}_{11}\boldsymbol{M}_{12}\epsilon\alpha(s_0) + \boldsymbol{M}_{12}^2\epsilon\gamma_{CS}(s_0). \tag{3.23}$$

Here $\boldsymbol{M}_{ij}$ refers to the $ij$ element of the transport matrix which is the product of the drift and quadrupole matrices between $s_0$ and $s_1$. For completeness, all Courant-Snyder parameters can be transferred with the following relation:

$$\mathbf{B}(s_1) = M \cdot \mathbf{B}(s_0) \cdot M^T, \tag{3.24}$$

where M is the product of the transfer matrices of the beamline (see for example Wille [2001]). Here $\mathbf{B}$ is called the beta- or beam-matrix

$$\mathbf{B} = \begin{pmatrix} \beta & -\alpha \\ -\alpha & \gamma_{CS} \end{pmatrix}.$$

Sometimes instead of the beta-matrix the sigma matrix is used, where $\boldsymbol{\sigma} = \varepsilon\mathbf{B}$.

### Coupling of phase space planes

A simpler 2D version of Liouville's theorem requires that the phase space *area* in a 2D subspace remains constant with time. Taking the area enclosed by two vectors $x_1$ and $x_2$, and transforming it through an arbitrary beamline element $\boldsymbol{M}$:

$$A_{initial} = \frac{1}{2}|\vec{x_1} \times \vec{x_2}|$$

$$A_{final} = \frac{1}{2}|\boldsymbol{M}\vec{x_1} \times \boldsymbol{M}\vec{x_2}| \ = \frac{1}{2}|\boldsymbol{M}|\,|\vec{x_1} \times \vec{x_2}|.$$

For the phase space area to remain constant, it follows that $|\boldsymbol{M}| = \det\boldsymbol{M} = 1$. It can be shown that this idea also applies to the full 6D phase space and therefore $\det\boldsymbol{M} = 1$ is indeed a direct consequence of Liouville's theorem. The assertion of a constant phase area in a 2D subspace like it was made above is only valid if there is no coupling between the different dimensions. If there is coupling, then a decrease in the 2D phase area in $x, p_x$ can still be in perfect accordance with the Liouville theorem as it can be compensated by an increase in any of the remaining four dimensions and therefore maintain a constant 6D phase space volume. For example, in a quadrupole lens the kick in $p_x$ increases with its position $x$ such that parallel trajectories converge to a focal point (see section 3.1.2). However, there is also coupling to the $p_s$ dimension as this also affects the kick in $p_x$ (electrons with different energies are deflected differently). This results in an increase in the 2D phase space $x, p_x$ [iii]. For mono-energetic beams ($\delta p_s/p_s = 0$) this problem is not relevant. These ideas have very important consequences for the experimental work in this thesis where observations are only made in the $x, p_x$ plane and conclusions are drawn about the other transverse plane $y, p_y$. Experimentally relevant sources of coupling for the present work are:

1. The unintentional rotation error of the lenses (such that the line foci of each lens are not perfectly perpendicular to each other).

2. Aberrations in the lens magnetic field components; the sextupole and (to a lesser extent) the higher order multipole components.

[iii] This increase is compensated by a decrease in the $p_s$ distribution which is transferred to the $p_x$ distribution.

Both effects do not in principle increase the 6D emittance (in practice it is often difficult to reverse an increase in a transverse plane). However, as only the 2D phase space can be measured in the presented experiment, these sources of coupling have to be minimised to be able to make claims about the total transverse (4D) emittance. For a discussion on the reasons for coupling between the transverse planes, see section 3.3. A quantitative analysis of the experimental consequences of these effects for this thesis is done using simulations in section 4.3.

### 3.2.3. Imaging with quadrupole doublets

Thin lens approximation
Connection between beam waist, minimum spot size, and the image plane

The experiments for this thesis used a lens doublet to image an electron beam source to a plane behind a dipole-magnet spectrometer (see figure 4.1). Hence this beamline configuration will be analysed in further detail in this section.

#### Thin lens approximation

A typical experimental situation requires an electron beam of a given energy to be focused within a fixed total beamline length. The parameters that can be varied are the strength of the focusing lenses (by choosing their length and magnetic field gradient) and their positions in the beamline. In the previous section it was shown that it is reasonable to approximate the magnet lenses used in this thesis as thin lenses. This simplifies the job of finding the required drifts (distances before, after, and between the lenses) to achieve the goal of focusing (or collimating) an electron beam at a desired location behind the accelerator. It turns out that quadrupole doublets offer a compact and flexible solution for imaging beams of several hundred MeV for beamline lengths of $\sim 0.6\,\mathrm{m} \rightarrow \infty$ by changing their positions by only a few centimetres. The thin-lens approximation can also be used to deduce the resulting magnification of the object in the image plane.

Quadrupole lenses are focusing in one plane and defocusing in the perpendicular plane, hence to create a focusing system for imaging in both planes, at least two lenses are required (see fig. 3.6). The transfer matrix from the exit of the accelerator through the doublet and some further (to be determined) drift to a focus is:

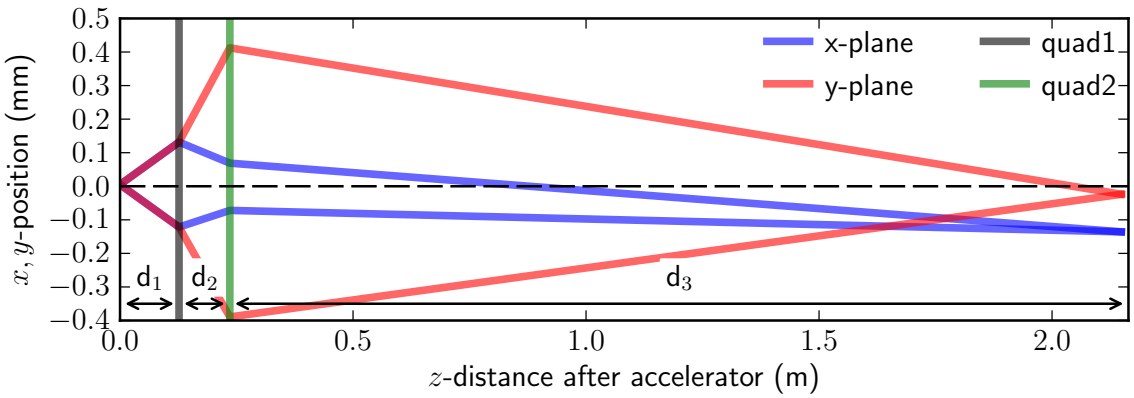


**Figure 3.6. – Electron beam focusing with a lens doublet.** With two or more lenses a net focusing effect in both planes can be achieved (depending on the lens positions $d_1, d_2, d_3$). Here the horizontal and vertical trajectories of two particles with the same initial offset position ($x = 5\,\mu\text{m}$, $y = 5\,\mu\text{m}$) and angles ($x' = \pm 1$ mrad, $y' = \pm 1$ mrad) are shown. Both planes are imaged about 2 m behind the accelerator. The initial transverse offsets lead to a correspondingly magnified offset at the image plane. The different magnifications in each plane lead to an elliptical transverse beam profile at the image position.

$$\begin{aligned} \boldsymbol{M_x} &= \boldsymbol{M}_{\mathrm{d3}} \cdot \boldsymbol{M}_{QD} \cdot \boldsymbol{M}_{\mathrm{d2}} \cdot \boldsymbol{M}_{QF} \cdot \boldsymbol{M}_{\mathrm{d1}} \\ &= \begin{pmatrix} 1 & d_3 \\ 0 & 1 \end{pmatrix} \begin{pmatrix} 1 & 0 \\ -1/f_2 & 1 \end{pmatrix} \begin{pmatrix} 1 & d_2 \\ 0 & 1 \end{pmatrix} \begin{pmatrix} 1 & 0 \\ -1/f_1 & 1 \end{pmatrix} \begin{pmatrix} 1 & d_1 \\ 0 & 1 \end{pmatrix}. \end{aligned} \tag{3.25}$$

The corresponding transport matrix in the $y$-plane is obtained by making the substitutions $f_1, f_2 \to -f_1, -f_2$ as in this plane the quadrupole lenses simply change from focusing to defocusing and vice-versa. For the system to image in the $x$ plane, the $(x|x'_0)$ term of $\boldsymbol{M_x}$ should vanish; i.e. the final position $x$ should not depend on the initial angle $x'_0$. If the same condition is imposed on the $y$-plane, the doublet creates a stigmatic focus (image plane for $x$ and $y$ overlap after the second lens as in fig. 3.6). Setting $(x|x'_0) = (y|y'_0) = 0$ results in the following functions for the drifts and focal lengths of the lenses[iv]:

[iv] The other solutions result in negative drifts and are disregarded. The solutions were obtained using the algebraic solver of the sympy python package.

$$d_2 = \frac{{f_1}^2 d_1 + \sqrt{-a f_1 {d_1}^2}}{{d_1}^2 - {f_1}^2}, \tag{3.26a}$$

$$d_3 = \frac{f_2 \sqrt{-a f_1 {d_1}^2}}{a}, \tag{3.26b}$$

where

$$a = {f_1}^2 f_2 - f_1 {d_1}^2 - f_2 {d_1}^2. \tag{3.26c}$$

With these equations the positions of the lenses (given their focal lengths $f_1$ and $f_2$) can be determines as a function of $d_1$. This formulation is convenient as $d_1$ is often constrained by the experimental setup. On the one hand a small $d_1$ and $d_2$ are important for maintaining a short bunch duration of the electron beam [Weingartner et al. 2011] (see also section 3.3.1), and also to avoid ablation of the lenses due to the diverging driver laser which may be clipped at the lens apertures. It is also desirable to have $d_1 \approx d_2 \ll d_3$ so that the electrons in the defocused plane after lens 1 do not scatter at the aperture of lens 2. As an added benefit, the lens system will be compact and not separated over large parts of the experiment. Furthermore, a certain minimum distance to the gas cell may be required for other parts of the experimental setup. An obvious approach to equations (3.26) is to set the focal lengths of the two lenses to be equal; i.e. $f_1 = -f_2$ (net focusing in both planes requires a positive and a negative lens). It then follows from (3.26b) that $d_1 = d_3$ which violates the requirement to have $d_1 \ll d_3$. This leaves the combination of a weak and a strong lens. To obtain a large value for $d_3$, let $a \to 0$. If the first lens is stronger ($|f_1| < |f_2|$) and positive, then from (3.26c) $a(d_1 = 0) < 0$ (as lens two is negative) and increases with $d_1$. The parameter $a$ becomes zero when

$$d_{1\max} = f_1 \sqrt{\frac{f_2}{f_1 + f_2}}, \tag{3.27}$$

at which point $d_3 \to \infty$ and the lens system focuses particles at infinity, i.e. the beam is collimated. Therefore by substituting the expression for $d_{1\max}$ into equation (3.26a), the lens drifts for collimating the beam are obtained. In the other direction $d_1$ is limited by the denominator in (3.26a) resulting in $d_{1\min} = f_1$. By inspecting (3.26a), it becomes apparent that if the first lens is *weaker* than the second lens, $a$ never reaches zero and therefore it is not possible to find an imaging setup with $d_3 \gg d_1, d_2$.

The $(x|x_0)$ and $(y|y_0)$ elements of $\boldsymbol{M_x}$ and $\boldsymbol{M_y}$ give the magnifications at the image plane:

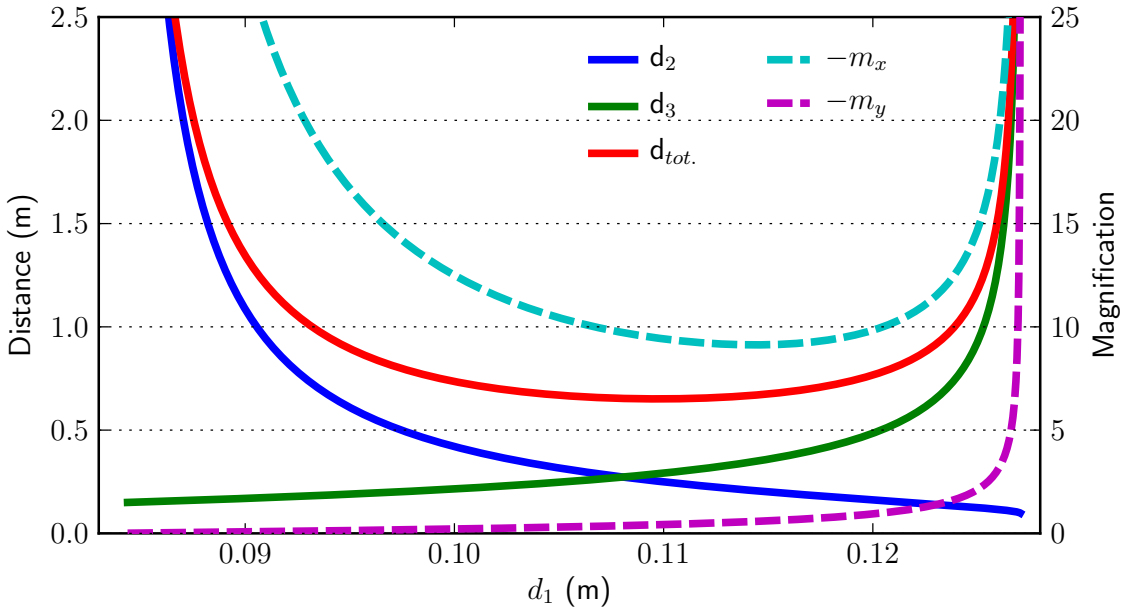


**Figure 3.7. – Generic solutions for the drifts of a stigmatic focusing doublet.** For a given beamline length $d_{tot}\,(= d_1 + d_2 + d_3)$, there are two possible solutions for the set of drifts $d_{1-3}$ (drifts defined in fig. 3.6). To maintain the ultra-short bunch length of LWFA electron beams and to have a compact beam imaging setup, it is preferable to have $d_1 + d_2$ be as small as possible. The lens focal lengths used for this plot correspond to those in the experimental work of this thesis ($f_1 = 8.4$ cm and $f_2 = -14.7$ cm, 300 MeV electron energy), the beamline length was $d_{tot} \sim 2.2$m.

$$m_{x,y} = \begin{cases} 1 - \dfrac{d_2}{f_1} + d_3\dfrac{d_2 - f_1 - f_2}{f_1 f_2} & x\text{-plane}, \quad (3.28a) \\ 1 + \dfrac{d_2}{f_1} + d_3\dfrac{d_2 + f_1 + f_2}{f_1 f_2} & y\text{-plane}, \quad (3.28b) \end{cases}$$

Figure 3.7 shows the lens positions and the resulting magnifications obtained from equations (3.26) and (3.28). The magnifications are not equal in both planes, this asymmetry is a general property of imaging with doublets. At least a triplet arrangement is required for the beam focus to be round. The optimal drift lengths for a fixed beamline length of 2.164 m as in the experiments of this thesis are $d_1 = 12.7$ cm, $d_2 = 10.9$ cm which is close to the numerical solution obtained

for real, full-length lenses of $d_1 = 12.4, d_2 = 9.3$ cm (see section 4.2 for numerical results for a range of electron energies). The lowest point of $d_{tot.}$ is approximately at the mid-point between $d_{1\min}$ and $d_{1\max}$ where also $d_2 \approx d_3$ holds. From these considerations an approximate relation for the minimum possible beamline length can be obtained

$$d_{\text{tot. min}} \approx \frac{1}{2}(d_{1\min} + d_{1\max}) + 2d_2 \tag{3.29}$$

$$= \frac{f_1\left(1 + \sqrt{\frac{f_2}{f_1+f_2}}\right)}{2} + 2\sqrt{f_2(f_1+4f_2)}, \tag{3.30}$$

which for the case shown in figure 3.7 results in $d_{\text{tot. min}} = 0.65$ m. It is clear from the figure that the doublet can focus the beam at any position $d \geq d_{\text{tot. min}}$ by a relatively small change in positions $d_1$ and $d_2$. An approximation of the lens drifts required to be able to collimate a particular beam energy is to use the values that $d_1$ and $d_2$ approach as $d_{\text{tot.}} \to \infty$ (long beam-line approximation):

$$d_{1,\text{long}} = f_1\sqrt{\frac{f_2}{f_1+f_2}} = \frac{E\,[\text{GeV}]}{0.3}\sqrt{\frac{1}{g_1w_1(g_1w_1+g_2w_2)}} \tag{3.31}$$

$$d_{2,\text{long}} \approx \sqrt{f_2(f_1+f_2)} = \frac{E\,[\text{GeV}]}{0.3}\sqrt{\frac{g_1w_1+g_2w_2}{g_1w_1(g_2w_2)^2}}. \tag{3.32}$$

Where the equation for $d_1$ is an upper limit as discussed for equation (3.27), and the equation for $d_2$ is an approximation[v]. The drifts for collimation are therefore linearly dependent on the electron beam energy. The higher the beam energy, the more of the lens aperture must be illuminated where focusing is stronger. For a divergent beam this means longer drifts. The magnification in the image plane can be estimated by setting $d_3 = d_{\text{tot.}} - d_{1,\text{long}} - d_{2,\text{long}}$ and $d_2 = d_{2,\text{long}}$ in (3.28). In the long beamline approximation the third term of equation (3.28a) is the main contributor to the magnification in $x$ ($m_x$ is negative). Here it can be seen that a small $f_1$ (strong lens 1) and a long $f_2$ (weak lens 2, $f_2$ is negative) will lead to a larger magnification. These equations are useful for a quick estimate of possible lens

[v] By substituting $d_1 = f_x$ (doublet-system focal length) $+p_x$ (principal plane) into equation (3.26a) which assumes that the $e^-$-beam source is at the object focal plane of the lens doublet. Substituting equation (3.31) into (3.26a) is also valid, although it gives a more complicated expression with almost identical results.

positions, for actual experiments a numerical simulation[vi] including the thick lens transfer matrices (3.13a) and (3.14) should be used.

### Connection between beam waist, minimum spot size, and the image plane

Using the transfer matrix for the beamline (equation 3.25) and the propagation of the Courant-Snyder parameters (equation 3.24), the difference between a waist, an image, and the minimum beam size can be explored. The three concepts do not necessarily occur at the same position as the conditions required for each are different.

Recalling from equation 3.5 that $\boldsymbol{M}$ relates the position and angle of a particle before and after a beamline, the condition for imaging is that $(x|x'_0) = \boldsymbol{M}_{12} = 0$[vii]. This condition means that the initial angle $x'_0$ has no influence on the final position $x$ of the particle. The fulfilment of the imaging condition does *not* simultaneously guarantee that a beam waist will occur at the image plane.

The distance to a waist in a drift space, $L$, can be determined from any location where the beam matrix is known [Brown et al. 1980]: $L = \alpha/\gamma_{CS}$, where $\alpha$ and $\gamma_{CS}$ are the Courant-Snyder parameters of the beam. The drift of lens 2 can therefore be scanned until $\alpha = 0$ at a target to obtain an upright ellipse (a beam waist). Although it seems counter-intuitive at first, the smallest beam size behind a lens system at a target location is achieved by having a beam waist *before* the target location.

Figure 3.8 shows for which position of lens 2 a beam waist, minimum size, and image can be obtained at the target (a YAG:Ce crystal in the experiments of chapter 6). The relevant information here is that the lens setup in this example (based on the real setup as used in the experiment) can be considered to be imaging the accelerator source when the beam size is minimised at the YAG:Ce crystal. A further criterion for beam imaging can also be used in the experiment. The shot-to-shot position fluctuations of the imaged beam at the YAG:Ce crystal should be smallest when the lens system is imaging. This reduction in fluctuations is a characteristic of an imaging system because $(x|x'_0) = 0$: the pointing angle of the beam at the accelerator exit has no effect on the position of the beam at the image plane. The remaining position fluctuations at the image plane are then actually occurring at the source of the electron beam due to the corresponding fluctuations in the laser beam position (see section 6.2.6).

[vi] For example using the beam simulation code COSY INFINITY[Makino and Berz 2006].
[vii] $\boldsymbol{M}_{12}$ refers to the matrix element in the first row and second column.

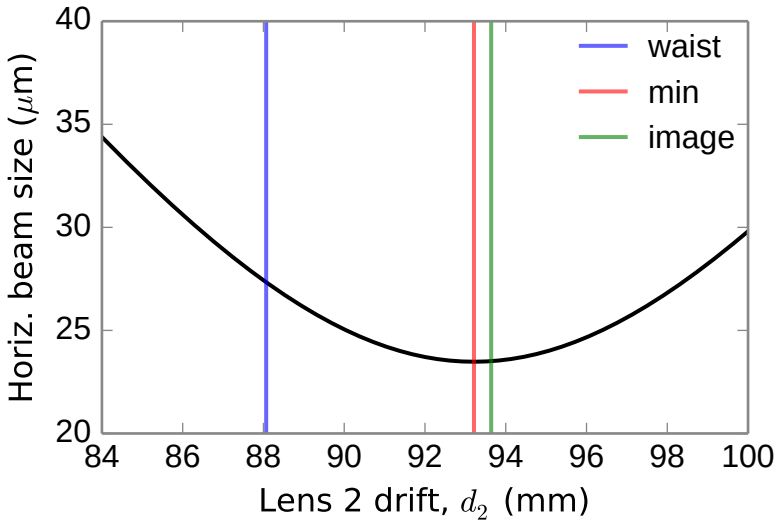


**Figure 3.8. – Beam size at YAG:Ce crystal and relevant imaging positions for lens position scan for conditions as in experiments for this thesis.** The beam has a waist at the YAG:Ce crystal when the drift of lens 2 is about 88 mm. Note that this does not correspond to the drift $d_2$ needed for a minimum beam size. To achieve a minimum beam size at a particular location, the beam waist needs to be *upstream* (in this case larger $d_2$) of the target. The lens system is almost imaging when the beam is smallest at the target.

## 3.3. Detrimental effects during beam transport

This section considers detrimental effects on the beam parameters associated with its transportation along a beamline. Whereas bunch elongation and space charge are present even for perfect transporting optics, rotated lenses and lens aberrations depend on the quality of the experimental equipment and its alignment.

As was mentioned in the previous section, if the transverse planes are not coupled, they can be considered independently and their respective projected emittances are conserved. Coupling occurs when the variables $x/x'$ have an influence on $y/y'$ and vice-versa (this happens for multipoles higher than quadrupole). The measurements made in the later parts of this thesis concern only the horizontal phase space. A coupling between the planes would therefore decrease the accuracy of the experimental measurements and compromise the validity of drawing conclusions about the vertical plane.

### 3.3.1. Bunch elongation

Benefits of short-focal-length devices
Comparison with electromagnet lenses

A useful feature of LWFA electron beams is their ultra-short pulse duration, measured to be a few femtoseconds [Lundh et al. 2011; Buck et al. 2011]. Experiments that rely on this short pulse duration and the associated high current of the beam (such as table-top free-electron lasers [Grüner et al. 2007]), require a beam transport system which causes minimal bunch elongation. Furthermore, it is desirable that the experimental setup is compact, which requires short focal length lenses[viii]. A short focal length can be realised with a large magnetic field gradient, $g$, or by using longer lenses (equation (3.10)). Conventional electro-magnet quadrupole (EMQ) focusing lenses employ current coils to generate field gradients of order 10 T/m whereas gradients of up to 560 T/m have been reported for PMQ lenses [Lim et al. 2005].

To compare these two lens types, simulations were carried out with a particle tracking code [GPT] of a 1 mrad beam (source size 1 µm) with an energy of 200 MeV. The requirement was a focus 2 m behind the accelerator. The PMQ lenses have a gradient of 500 T/m and lengths 17 and 15 mm. The EMQ lenses have a gradient of 10 T/m and the lengths and positions were determined by optimisation with the COSY INFINITY code [Makino and Berz 2006]. The lengths used for the comparison are: $l_{EMQ,1} = 30$ cm and $l_{EMQ,2} = 22$ cm.[ix] Figures 3.9(a) and 3.9(b) show the resulting bunch envelopes and elongation for the two cases. Comparing the beam envelope sizes with the bunch length shows a clear correlation between beam divergence and bunch length increase (especially in the drift between the first and second lenses). Although both cases have lenses of similar focal lengths, the EMQ case shows a greater bunch elongation which comes from the long drift sections with large divergence. Therefore, to **minimise bunch elongation**, lenses with short focal lengths *and* high magnetic field gradients are required. Ideally, the highly divergent LWFA beam is caught as early as possible after its exit from the plasma and collimated to minimise the angles and associated path length differences between particles in the beam. The effect of the initial divergence is shown in figure 3.9(c), the EMQ case always results in a bunch elongation about an order of magnitude more than the PMQ case.

[viii] This follows from the well-known lens-maker's formula: $1/f = 1/s_1 + 1/s_2$, where the variables $s_{1,2}$ denote the object and image plane distances to the lens. A short value for $f$ allows $s_{1,2}$ to be small resulting in a compact beam transport system.

[ix] The EMQ lengths and positions are a compromise between short EMQ lenses (note that $l_{EMQ} \gg l_{PMQ}$ for an equal focal length) and maximising the drift between the last lens and the target at 2 m to allow for other experimental equipment.

As an aside, simulations including space charge show no further increase in bunch length (fig. 3.9(b)). Space charge effects in the *transverse* plane are relevant however and are discussed in section 3.3.3.

Pulsed electric quadrupole lenses have demonstrated even higher magnetic field gradients than PMQ lenses; values of up to 1400 T/m have been achieved [Winkler et al. 2003]. However, this scheme is limited to repetition rates of order ∼1 Hz due to the charging time of the capacitor circuit needed to generate the required high currents. Another possibility is the use of superconducting quadrupole lenses but these devices are expensive and difficult to construct in a compact manner [Datzmann et al. 1999]. A further design is a hybrid lens using permanent magnet material and iron pole wedges to increase the magnetic field. However, an advantage of the "simpler" magnet-only devices over such containing iron poles is due to the linear superposition of the magnetic field contributions of each of the segments. This simplifies the tuning process to reduce unwanted magnetic field moments as discussed in the following section.

### 3.3.2. Transverse phase space coupling

Rotated lenses
Origin of lens field errors
Lens field tuning

A "rotated quadrupole" is a quadrupole field that is neither parallel nor perpendicular to the other quadrupole fields in the beamline. A roll error of a quadrupole field leads to a vertical kick that depends on the horizontal offset of the particles passing through it and vice-versa (see figure 3.10). In the doublet configuration as used in the experiments, the beam is focused and defocused in one plane (FODO) and in the opposite order in the other plane. In the FODO-plane (vertical in fig. 3.10), the size of the electron beam at the second lens has a strong influence on the eventual beam focus. Because of the roll error between the lenses, the beam has a larger extent and hence also a larger focus. Fortunately for a doublet lens setup, only a single lens needs to be rotated to minimise this error in an experiment.

The transfer matrix for a rotated quadrupole has to be 4x4 to include the coupling of the transverse planes. The transfer matrix through a quadrupole rotated by $\theta$ is $\vec{x} = \boldsymbol{R}^{-1}(\theta)\boldsymbol{M}_{quad}\boldsymbol{R}(\theta)\vec{x_0}$ [Conte and MacKay 2008]. Written explicitly:

$$\begin{pmatrix} x \\ x' \\ y \\ y' \end{pmatrix} = \begin{pmatrix} \vec{I}\cos\theta & \vec{I}\sin\theta \\ -\vec{I}\sin\theta & \vec{I}\cos\theta \end{pmatrix} \begin{pmatrix} \boldsymbol{M}_{QF} & 0 \\ 0 & \boldsymbol{M}_{QD} \end{pmatrix} \begin{pmatrix} \vec{I}\cos\theta & -\vec{I}\sin\theta \\ \vec{I}\sin\theta & \vec{I}\cos\theta \end{pmatrix} \begin{pmatrix} x_0 \\ x'_0 \\ y_0 \\ y'_0 \end{pmatrix}$$

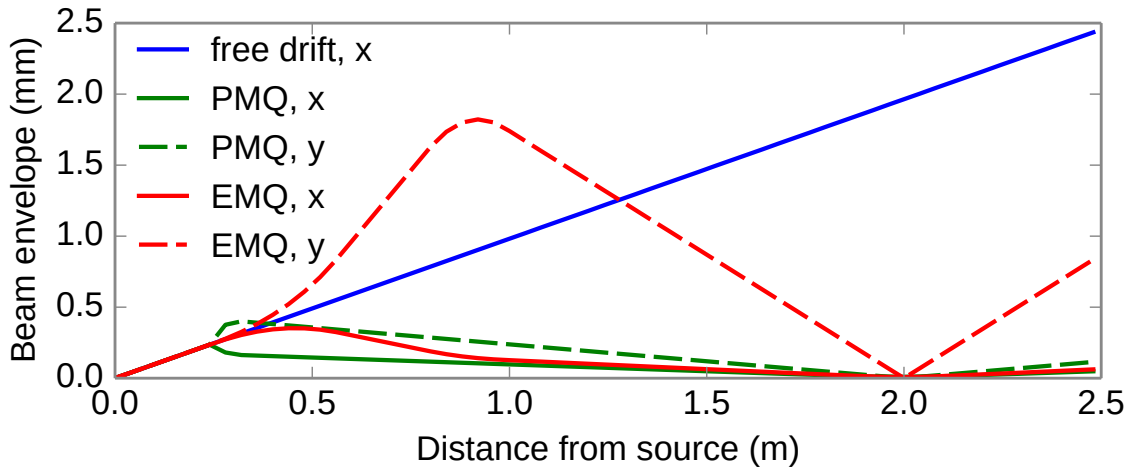


(a)

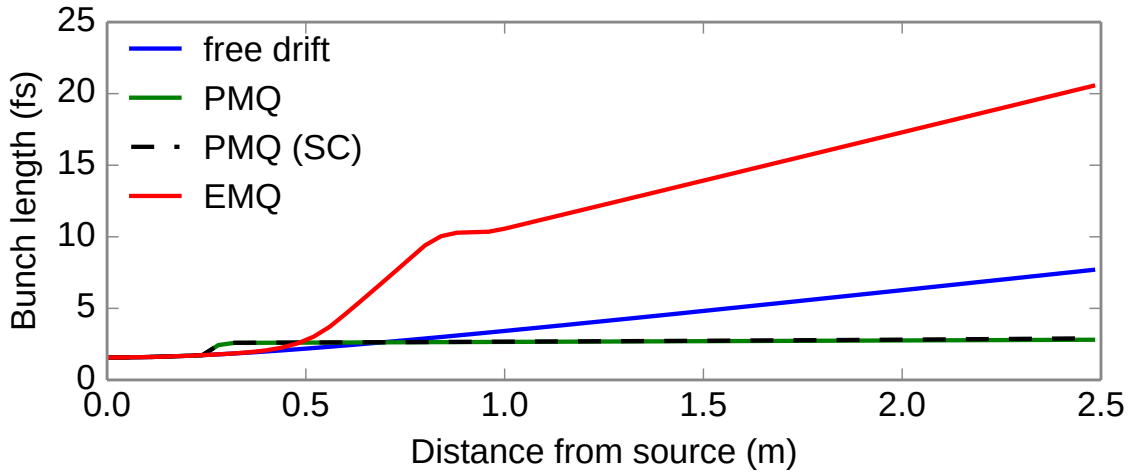


(b)

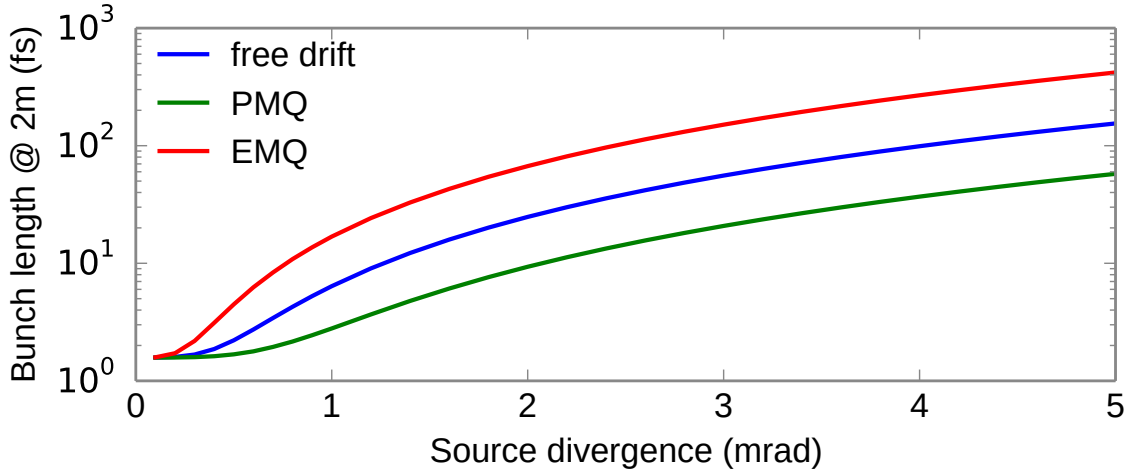


(c)

**Figure 3.9. – Effect of beam transport on bunch transport:** **(a)** Electron beam envelopes in the x- and y-plane for focusing with a PMQ doublet (17 and 15 mm long, 500 T/m) and an EMQ doublet (300 and 220 mm long, 10 T/m). **(b)** Evolution of the bunch duration along the beamline. For the PMQ case, a simulation with space-charge (SC) included is also plotted (the bunch has 15 pC of charge and a bunch length of $\sigma_z = 1.6$ fs). **(c)** Effect of initial divergence on the bunch duration in the focus, 2 m behind the accelerator.

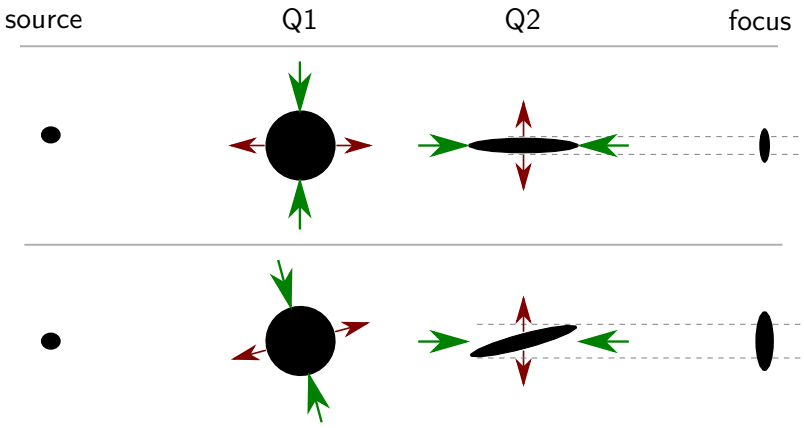


**Figure 3.10. – Effect of a rotated lens in a quadrupole imaging doublet.** The beam starts at the source on the left and passes through the quadrupole lenses Q1 (vertically focusing) and Q2 (horizontally focusing) and then comes to a focus. The upper beamline shows the beam cross section for a set of perpendicular quadrupole lenses. In the bottom beamline the first lens has a "roll" error (rotation around the beam propagation axis).

where $\vec{I}$ represents the 2x2 identity matrix, and $\boldsymbol{M}_{QF}$ and $\boldsymbol{M}_{QD}$ are given by equations 3.13a and 3.14 respectively. For the purposes of this thesis, it is desirable to align the quadrupole lenses such that $\theta = 0°$. The term "skew" quadrupole is sometimes used to refer to the special case where the quadrupole has a rotation of $\theta = 45°$. Quadrupoles with such rotations are for example used to intentionally couple the transverse axes and "distribute" the emittance such as to create a "sheet beam" with a large horizontal to vertical emittance ratio.

### Lens field aberrations

In the previous section a roll error between quadrupole lenses lead to a coupling of the transverse phase planes. This coupling can be resolved by adjusting the angle between the quadrupole fields. A further cause of coupling are aberrations in the quadrupole field. Such aberrations cause a distortion of the beam phase space, which leads to an effective increase in beam emittance. A perfect quadrupole lens contains no multipole moments of higher order, such as sextupole or octupole. The **origin of field errors** in the lenses used in this experiment are due to statistical variations in the magnetisation of the magnet wedges, the imperfect positioning of the wedges themselves, and the finite number of wedges used to create the magnetic field pattern. The optimisation of the field components by carefully shifting individual magnet wedges is shown in [Becker et al. 2009; Raith 2009]. The determination

of the field components works by measuring the radial component of the magnetic field on a circle inside the lens aperture. By making an assumption about the magnetic field due to symmetry[x], the magnetic field is fully characterised inside the aperture. An iterative process of measurement and shifting magnet wedges reduces undesirable multipole components. Any multipole component above the quadrupole introduces non-linear terms in the particle trajectory through the lens and therefore degrades the imaging quality. These multipole terms will be referred to as higher order magnetic field components or HOMFCs. For the lenses employed in this thesis the results of the tuning process along with the simulation of the remaining errors are discussed in the context of particle tracking simulations in section 4.3.1.

### 3.3.3. Space-charge

Free drift
At a waist

The relevance of space-charge or emittance in beam-envelope dynamics can be checked by comparing the corresponding terms in the rms beam envelope equation for an ultrarelativistic beam ($\gamma \gg 1$) in a drift space [Reiser 2008]:

$$x(s)'' - \frac{I}{2I_A\gamma^3 x(s)} - \frac{\epsilon_{norm.}^2}{\gamma^2 x(s)^3} = 0. \tag{3.33}$$

Here $I$ is the peak beam current, $I_A = ec/r_e \approx 17$ kA is the Alfven current, and the beam is assumed to be round in the transverse plane (i.e. $x(s) = y(s)$). The ratio of the space charge and emittance terms gives [Anderson and Rosenzweig 2002]:

$$R_0 = \frac{Ix(s)^2}{2I_A\gamma\varepsilon_{norm.}^2} \tag{3.34}$$

From equations 3.33 and 3.34 it is clear that for a small enough value of $x(s)$, the expansion of the beam is emittance dominated. As an example, the ratio of equation 3.34 can be calculated for the electron beam at the exit of the plasma. For the beam parameters at the exit of the accelerator the values obtained from the experiments of this thesis can be used: $x(0) = 0.9\mu$m, $\gamma = 500$, $\varepsilon_{norm.} = 0.2$ $\pi$·mm·mrad, and for the beam current a recently published experimental value $I = 5$ kA [Lundh et al. 2011]. Substituting these values into equation 3.34 gives $R_0 = 6 \times 10^{-3}$, so the beam expansion is initially dominated by the emittance (divergence) of the beam. After the beam passes through the lenses it is focused at a distance 2 m away

[x] In the lens centre the longitudinal magnetic field is zero. This assumption can be checked by using a 3D Hall probe.

and so propagates for this distance with a beam size of ∼30 µm in the horizontal plane. Using $x(s) = 30\,\mu m$ gives $R_0 = 6.6$, indicating that space charge dominates over the emittance in the drift section to the focus. This is plausible as behind the lens system the beam is almost collimated and hence beam expansion is due to space charge. There are two effects that reduce the severity of this space-charge dominance: firstly the space charge term by itself scales inversely with the beam size so that its absolute effect is not so strong for the larger beam, and secondly in the experiment the beam is dispersed vertically by the dipole magnet spectrometer which reduces the beam density and therefore also the space charge forces. In the experimental part of this work, these effects are simulated with the help of a particle simulation code [GPT].

The effect of space charge on the longitudinal (temporal) bunch profile was touched on in section 3.3.1 and found not to be relevant in terms of bunch length (it is important when considering the energy chirp of the beam however [Grüner et al. 2009]). Space charge increases the transverse emittance and can become noticeable for a quadrupole scan. In the work of [Anderson and Rosenzweig 2002] it is shown that space charge causes an asymmetry around the minimum spot size for a quadrupole scan with a strong space-charge beam. To see this figure 3.11 shows a beam envelope with and without space charge according to equation 3.33. At the beam source, the divergence is high and the additional effect of the space-charge is negligible (the beam is emittance dominated). In the long drift section the space-charge beam expands faster due to the coulomb explosion. In the context of the emittance measurements made for this thesis, the effect of space charge on a lens scan (see section 3.4.1) is shown in figure 3.12. Two effects are apparent from this figure:

1. The base (the turning point) of the curve of the beam size "shifts" to larger lens 2 drifts. Due to the additional space charge forces the doublet needs to have stronger focusing (larger drift lens 2) to focus the beam at the same position

2. The curve becomes asymmetrical about the minimum. For points to the left of the minimum (weaker focusing), the flank is flatter than for points on the right side (stronger focusing). For larger drifts the doublet is stronger focusing and hence the beam goes through a waist further upstream (see figure 3.11). This leads to longer drifts where the divergence of the beam is high and so the effect of space charge is smaller compared to the high (emittance dominated) divergence of the beam. This means that the flanks of the space-charge and non-space-charge curves approach each other for large lens 2 drifts. Similarly the flanks on the left side approach each other as the doublet focusing is eventually so weak that the source beam divergence is hardly altered and remains large (emittance dominated). As the flanks approach each other and the turning point of the space-charge beam is shifted, the curve becomes asymmetric.

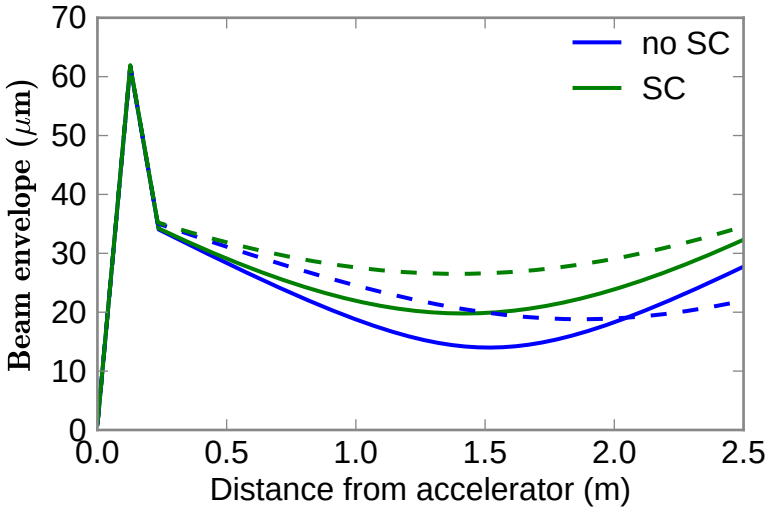


**Figure 3.11. – Effect of space charge force on beam envelope.** Solution to equation 3.33 using thin lenses. The drift between lens 1 and lens 2 is 109 mm (solid lines, "stronger focusing") and 105 mm (dashed lines, "weaker focusing").

## 3.4. Emittance measurement for LWFA beams

The basis for retrieving the emittance from beam-profile measurements with quadrupoles is equation 3.23, reproduced here again for convenience:

$$\sigma(s_1)^2 = M_{11}^2\epsilon\beta(s_0) - 2M_{11}M_{12}\epsilon\alpha(s_0) + M_{12}^2\epsilon\gamma_{CS}(s_0).$$

By measuring the beam size $\sigma(s_1)$ for various $M$, the Courant-Snyder parameters and the emittance are found using a least-squares fit algorithm. In a typical quadrupole scan measurement, $M$ is varied by changing the quadrupole strength such that the beam passes through a focus at $s_1$ for the best accuracy. For the experiments of this thesis the quadrupole strength is fixed so the position of a lens is varied, or $\sigma(s_1)$ is measured for different beam energies.

In terms of accuracy of the retrieved parameters, it is best to measure the beam size around the image plane. Here the electron beam source size is imaged, and hence a direct linear dependence between source size and measured beam size occurs. Furthermore, by imaging the electron beam source with an appropriate magnification, it becomes easier to resolve the small source size of approximately 1 µm expected of LWFA beams.

The limitations of quadrupole scan techniques are:

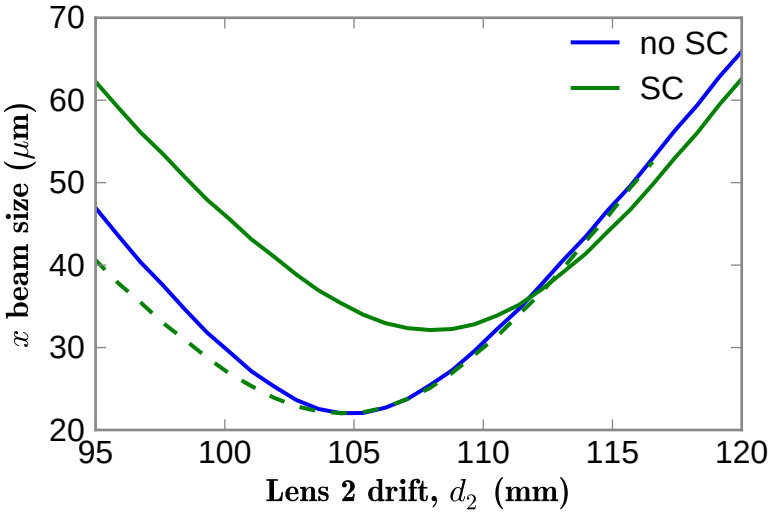


**Figure 3.12. – Effect of space charge force on lens 2 position scan**. Solution to equation 3.33 using thin lenses for the beam size at the YAG:Ce crystal. The green dashed line is an offset version of the green solid curve to facilitate the comparison to the non-space-charge case. The space charge beam leads to a flatter curve relative to the non-space charge case for smaller lens 2 drifts.

1. the maximum measurable energy is limited by what can be focused within the beamline.

2. The semi-destructive nature of the measurement; the beam is focused which may or may not be a hindrance for further experiments with the electron beam.

3. The long drift lengths can lead to an overestimate of the emittance for beams which are affected by strong space charge.

4. The quadrupole lenses need to have low field aberrations for an accurate emittance estimate.

### 3.4.1. Quadrupole lens position scan

For this method, the position of lens 2 is altered (this is the variation in $M$) and the change in beam size is measured at $s_1$. Figure 3.13 shows the effect of the lens-position variation for different initial electron beam parameters. The height of the parabola is mainly determined by the electron beam source size, the opening angle is mainly determined by the source divergence. Here it becomes clear that the source

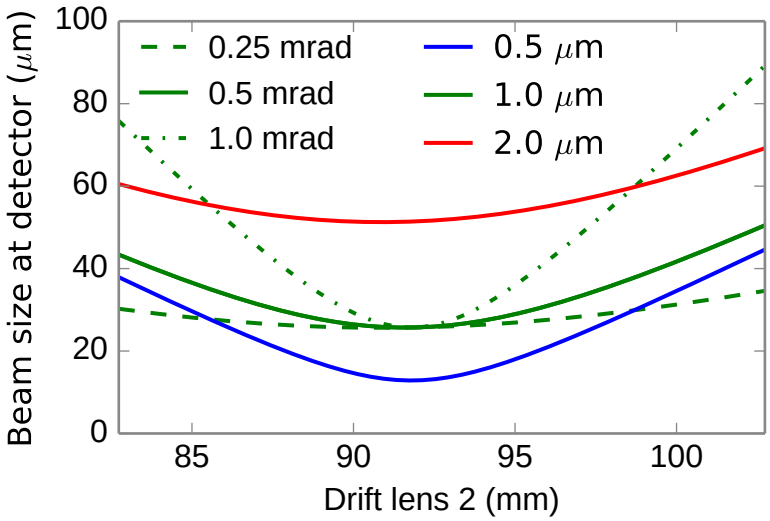


**Figure 3.13. – Effect of changing position of lens 2 on electron beam size at YAG:Ce crystal.** The curves of different divergence (0.25, 0.5, 1 mrad) assume a source size of 1 µm. The source size curves (0.5 µm, 1 µm, 2 µm) assume a divergence of 0.5 mrad. The electron energy affects the "horizontal position" of the curves.

size is best determined near the minimum beam size at the target position[xi]. Outside of the minimum-beam-size region, the dependence on the source size diminishes in comparison to the dependence on the beam divergence.

### 3.4.2. Single-shot "quadrupole scan"

An alternative way to obtain the emittance is to scan the beam energy as opposed to the position of a lens. In the experiments for this thesis the beam size for a small range of energies can be evaluated for each shot. Depending on the energy being measured (which determines the associated dispersion of the spectrometer) and the field of view of the optical imaging equipment, the beam width of electrons within a bandwidth of about 4 MeV can be measured. The variation of the natural emittance over this energy window is about ±1%. Therefore the electrons within the 4 MeV energy window will at least have a small variation due to adiabatic damping during acceleration. The question is whether the electrons which eventually have this range of energies are injected into the plasma wakefield under the same conditions. It has been shown in experiments that the longitudinal electric fields in the wakefield reach

[xi] When the lens position is adjusted to give the minimum beam size at the target, the beam is effectively being imaged from the source to the target (see figure 3.8).

values of $\sim 100$ GeV/m [Popp 2011]. For such large accelerating fields and assuming that electrons are trapped and accelerated to their final energy (ignore dephasing), electrons in a bandwidth of 4 MeV were injected within 4 MeV/100 GeVm$^{-1}$ = 40 µm. Popp [2011] also contains simulations with parameters like in the experiments presented here. The laser beam undergoes self-focusing at a rate of about 18 µm per mm of propagation distance until it oscillates around a 10 µm beam size. Within a 40 µm injection distance the laser spot size therefore changes by at most 1 µm. From the discussion in the summary of chapter 2 (section 2.8), the injected beam size depends on the laser beam size. Although the change of the laser beam during injection is not completely negligible, it is expected to be small and therefore the emittance of electrons within the 4 MeV window is considered constant for the analysis of the experimental data.

### 3.4.3. Other emittance measurement methods

**Multiple profile monitors:** The beam size is measured at multiple locations along the beamline separated by drift spaces. For very stable conventional accelerators, the profile monitors can be individually inserted into the beam and so the associated scattering is minimised. The measurement is taken at three or more different locations, ideally around the beam waist. Without any further focusing this requirement is fulfilled at the electron beam source. This method has recently been applied to LWFA beams by Krus et al. [2015], which measured an emittance of 22 $\pi$·mm·mrad for a 750 MeV electron beam. The reference discusses the need to have the beam profile measurement close to the accelerator exit for an accurate result. For high-power laser beams this is problematic due to the destruction of the screen by the laser.

**Pepper pot:** The beam is sent through a mask which contains holes ("pepper pot") where the beam can pass undisturbed and the rest is scattered by the mask material. The divergence of the individual unscattered beamlets can be obtained by measuring the spot size after a drift length behind the pepper pot. The scattered parts of the beam result in background noise for the measurement. Published results for LWFA beams: Fritzler et al. [2004]; Sears et al. [2010a]; Brunetti et al. [2010]; Manahan et al. [2014]. The technique is traditionally used for low energy beams where scattering of the beam is still significant with thin, high-density material masks. Further work has extended the energy range up to 3 GeV, [Thomas et al. 2013], however the construction of the pepper pot becomes increasingly challenging the higher the beam energy. Aside from this challenge, a general problem for this method is the characteristic phase space of plasma-accelerated electrons with the large aspect ratio between the electron beam source size and its divergence. The resulting poor

accuracy is discussed in Cianchi et al. [2013].

**Betatron radiation**: The electron beam source size is deduced from the betatron radiation emitted by the electrons during their acceleration in the plasma. This information can be combined with a simultaneous measurement of the electron beam spectra and divergence. Published results for LWFA beams: [Kneip et al. 2012; Plateau et al. 2012; Schnell et al. 2012]. This method combines the beam size in the plasma with the divergence of the beam after it has exited the plasma. Hence the deduced emittance does not consider the effect of the plasma density downramp which can alter the divergence and beam size (see section 2.6).

# 4. Experimental setup and measurement limitations

This chapter introduces the experimental setup used to obtain the results of the subsequent two chapters (figure 4.1). During the course of this thesis the laser system was upgraded and various modifications were made to the target chamber and diagnostics. The modifications to the setup that are relevant to the experimental results will be mentioned. The errors and limitations of the setup critically influence the conclusions drawn from the experimental results, hence these are also discussed in detail here.

## 4.1. Electron acceleration

### 4.1.1. Laser system

Part of the results of this thesis were obtained prior to the 2009/2010 laser upgrade which resulted in a power boost from 20 to 80 TW. For all experiments the laser was focused with an off-axis parabola with focal length 1.54 m into the gas target. The relevant laser parameters are given in table 4.1. The ATLAS laser system consists of a series of Titanium-doped sapphire crystal amplifiers employing the chirped-pulse amplification (CPA) technique. Prior to this technique, pulse intensities were severely limited by the damage threshold of the amplifying crystals, requiring large (and expensive) crystals to spread the energy of high intensity beams over a large area. CPA spreads the pulse energy in time by introducing path length differences between frequency components of the laser using an arrangement of gratings and/or prisms. The laser can then be compressed after the final amplification stage to obtain a high power for the experiment.

For the ATLAS-80 upgrade, additional power amplifiers increase the beam energy but also an additional new component (an acousto-optic modulator, "*MAZZLER*") also decreased the pulse length (for details see [Popp 2011]). To achieve wavebreaking and self-injection, experiments with the ATLAS-20 relied on the self-focusing and -compression of the laser in the plasma to reach the required intensities [Osterhoff et al. 2008]. The power boost from the upgrade improved the stability of the electron acceleration experiment as the higher laser intensity reduced the need

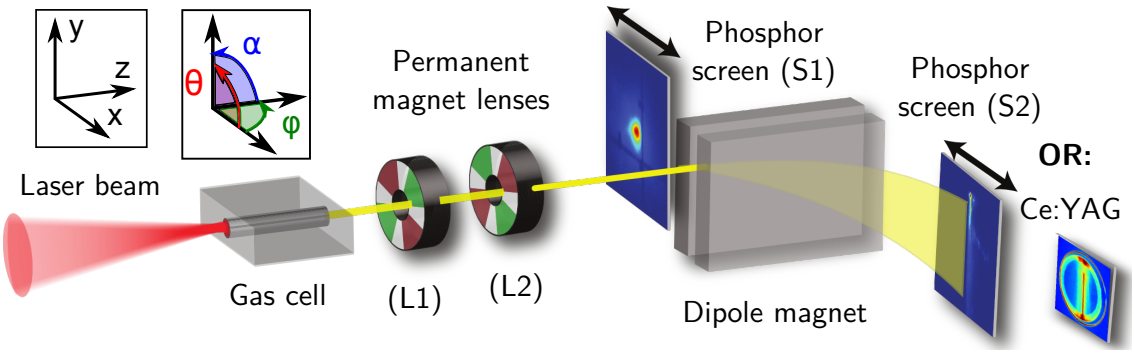


**Figure 4.1. – General experimental setup.** The ATLAS laser beam is focused into a hydrogen-filled gas cell, ionises the gas and excites a plasma wakefield. The plasma wave breaks and electrons are injected and accelerated by the wakefield. The electrons pass through a pair of magnetic quadrupole lenses 10 to 20 cm behind the gas cell which can focus, collimate, and steer the electron beam. Both lenses have a measured field gradient of ∼500 T/m and are between 15 and 25 mm long. The spatial characteristics of the electron beam are observed on a removable scintillating screen (S1), and the spectral profile behind a dipole magnet with a second scintillating screen (S2). Alternatively to S2, a YAG:Ce crystal (diameter 10 mm, thickness 0.3 mm) with high spatial resolution can be used to observe a ∼3 MeV part of the spectrum and displaced vertically to observe different parts of the spectrum. The exact distances, lens lengths, and dipole magnet strength changed during the course of the thesis and are given at each relevant experimental section.

to rely on the non-linear processes in the plasma to shape the pulse to a condition where it could reach wave breaking.

**Table 4.1. – Laser parameters** $E$: laser pulse energy, $\tau$: pulse duration, $w_0$: beam size at focus, $I$: focused intensity, $a_0$: normalised laser vector potential. The parameter $a_0$ is calculated using equation 2.4

| | E (J) | $\tau$ (fs) | $w_0$ ($\mu$m) | $I$ [Wcm$^{-2}$] | $a_0$ |
|---|---|---|---|---|---|
| ATLAS-20 | 0.85 | 42 | 19.5 | $1.7 \times 10^{18}$ | 0.9 |
| ATLAS-80 | 1.7 | 23 | 18.7 | $1.3 \times 10^{19}$ | 2.5 |

### 4.1.2. Gas target

Pulsed gas capillary
Variable-length gas cell

The two types of gas targets that were used for the experiments of this thesis were a 15 mm long capillary and a variable-length (2 to 14 mm) gas cell. In both cases the target geometry and the gas-filling conditions were chosen such that a reproducible, homogeneous gas distribution was achieved in the experiment. The gas target was filled with hydrogen gas sufficiently early ($>$ 50 ms) before the arrival of the laser; this means that gas turbulences are minimised and the valve opening process ($\sim$2 ms) has no influence on the density distribution.

The ionisation of the hydrogen gas to plasma was done by the driver laser itself without pre-ionisation with an electrical discharge.

#### Pulsed gas capillary

The capillary gas target consists of two sapphire blocks, each with a half-cylindrical groove. When pressed together they form a 15 mm long, 250 µm diameter channel (figure 4.2). These targets are very durable offering operation over several thousand laser shots [Osterhoff 2008] and were typically operated at 0.1 Hz synchronised to the laser pulse. As opposed to experiments with a pre-ionisation electrical discharge, the exact diameter of the capillary is not important for the electron beam properties as experiments with different sized capillaries showed [Osterhoff et al. 2008].

#### Variable-length gas cell

The variable length gas cell consists of a cylinder with a movable piston inside which can be used to set the length of the gas volume that the laser interacts with. As the diameter of the capillary proved itself to be unimportant for the acceleration process, the difference between this target and the pulsed gas capillary is the different geometry of the gas entrance and exit holes and the acceleration length. The gas-inlet holes and the gas valve opening times were again chosen to produce a homogeneous gas density distribution. The length variability of the gas cell was used to study the effects of a varying interaction length on the energy gain and charge of the accelerated electron beam and gives information about the dephasing of the electron beam with the accelerating wakefield [Popp 2011].

The density profile within the gas cell could be investigated using transparent gas cells. Until then, computational fluid dynamics simulations are necessary to get an idea of the density profile inside and at the entrance and exit of the gas cell.

The OpenFOAM simulation presented here takes advantage of the symmetry of

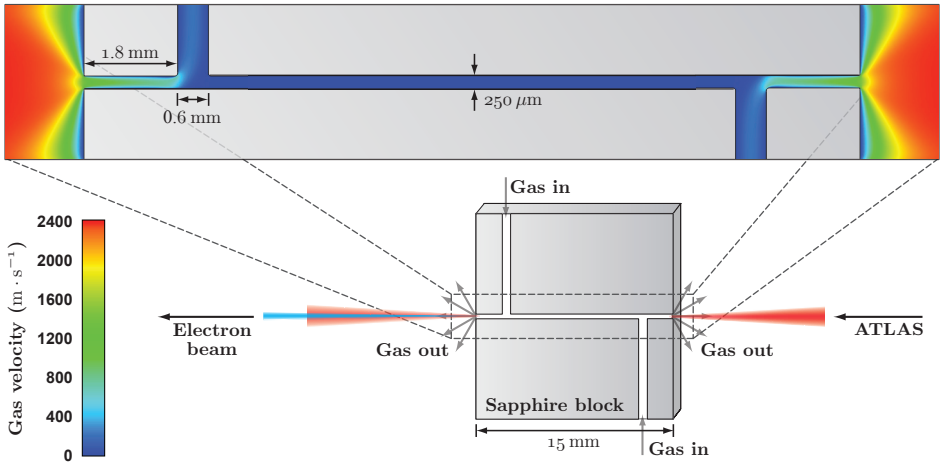


**Figure 4.2. – Capillary gas target.** The velocity distribution inside the capillary was simulated with the fluid dynamics code FLUENT. After the initial valve opening the gas settles down to become almost stationary and results in very reproducible conditions for electron acceleration. Illustration taken from [Osterhoff 2008].

the gas cell and only considers an 1/8 wedge of the entire volume and employs appropriate boundary conditions to model the real gas cell. Even though the area of the gas inlets going into the gas cell (8 × 1 mm inlets) is four times that of the outlets (2 × 1 mm inlets), it is clear from figure 4.3 that the pressure inside the gas cell does not simply correspond to the pressure in the gas inlets. The electron densities that are mentioned in the experimental section is calculated from the backing pressure at the gas cell inlets; the actual electron density in the gas cell is therefore lower.

## 4.2. Electron beam focusing devices

Lens geometry and magnetic parameters
Choice of experimental setup

The magnetic lenses used to image the electron beams consisted of 12 wedges of permanent magnet material, $Nd_2Fe_{14}B$, with a remanent field of 1.3 T. Figure 4.4 shows how the magnet wedges are magnetised and arranged to produce a quadrupole field resulting in a surface magnetisation of 1.5 T, and a magnetic field gradient of ∼500 T/m [Eichner et al. 2007]. The high field gradient is possible due to the small bore radius of only 3 mm, the outer diameter is 35 mm.

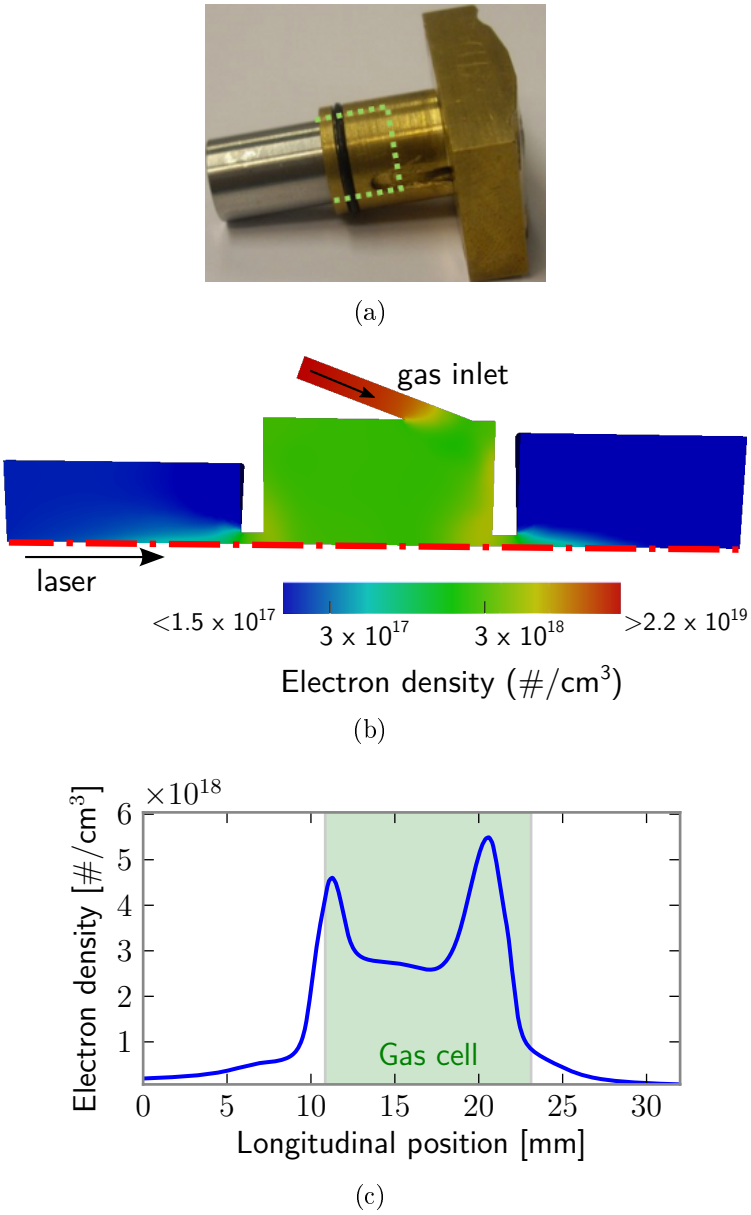


**Figure 4.3.** – **Variable-length gas cell.** a) Photograph of the gas target. b) Fluid dynamics simulation with OpenFOAM of the density in the gas cell after 5 ms with 100 mbar inlet pressure. The red dash-dotted line represents a symmetry axis in the simulation (a $45°$ wedge is sufficient to model the gas cell), the laser propagation axis, and also indicates where the lineout is taken for the density profile plotted in c). The low-density (blue) regions on either side of the gas cell are the vacuum outside of the gas cell. Simulation courtesy of S.W. Chou.

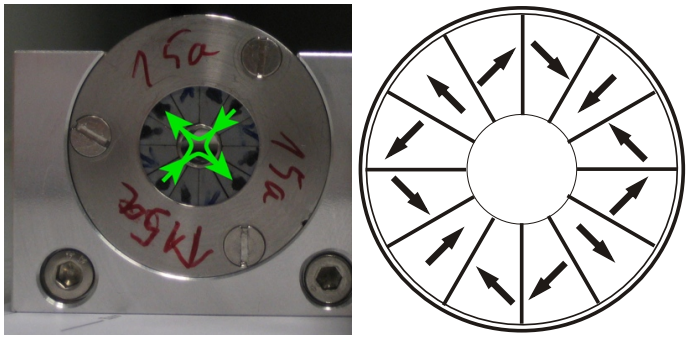

**Figure 4.4. – Magnetic quadrupole lenses.** A mounted quadrupole lens and a schematic diagram showing the 12 NdFeB wedges and their magnetisation.

In section 3.2.3 it was shown that by using a quadrupole doublet for imaging, the magnification is different for the two transverse planes. In general the beam therefore has an elliptical transverse shape at a set position behind the lenses. From figure 4.1 it is clear that at the position of the YAG:Ce crystal, only one transverse plane contains information about the beam size because the other is spectrally dispersed by the dipole magnet. The decision has to be made in which plane a large magnification and in which plane a small magnification most benefits the experiment. Figure 4.5 shows the chosen configuration: the size of the beam was measured in the horizontal plane (large magnification), the vertical plane (small magnification) was dispersed by the dipole magnet. The reasons for this choice were:

1. The larger magnification of the beam horizontally reduced the effect of resolution smearing from the imaging optics (discussed in detail in section 4.4.4). The real beam size is added in quadrature (assuming a Gaussian point-spread function for the optics) with the optics resolution. A large horizontal magnification is therefore beneficial.

2. The potential errors caused by fluctuations in electron beam source position and source pointing should be minimised. The source *pointing* fluctuations do not result in any changes at the YAG:Ce crystal (assuming there is perfect point-to-point imaging of the source). However, the source *position* fluctuations are magnified and lead to fluctuations in the position on the YAG:Ce crystal (see measurements of this in section 6.2.6). This does not influence the measured width of the focus, only its position. This fluctuation is important in the vertical direction as a position offset changes the energy of the electrons arriving at a fixed vertical position of the YAG:Ce crystal. Due to the lens chromaticity the electron beam width depends on the energy and therefore the measured width would fluctuate from shot to shot. It is therefore best to have

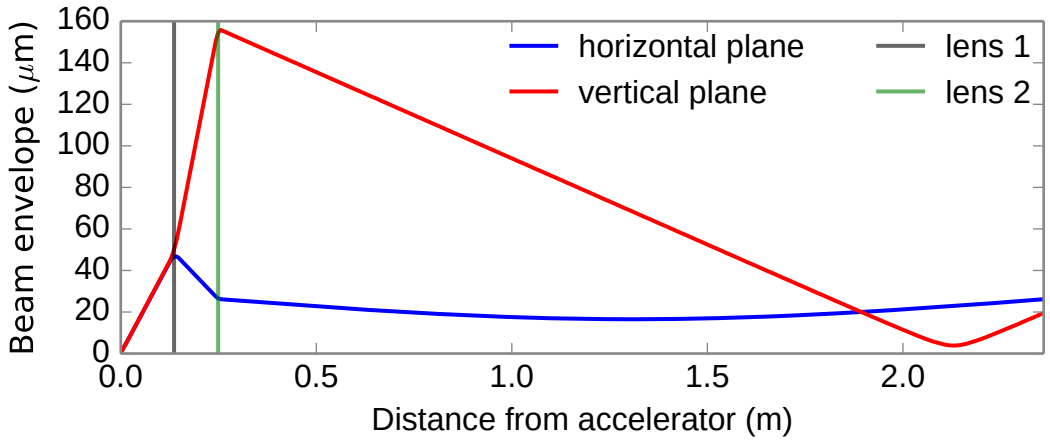


**Figure 4.5. – Simulated beam envelope from the accelerator to the YAG:Ce crystal.** The source beam size and divergence is as measured experimentally (0.9 µm and 0.4 mrad respectively), the quadrupole lenses are positioned at approximately 12 and 24 cm. The lens magnetic fields are discussed in section 4.3 and shown in figures 4.6 and 4.7.

a small magnification in the vertical plane. A rough estimate of this effect based on experimental data is made in section 6.2.6.

3. The small magnification vertically means that there is less overlap of different electron energies (see the discussion in section 4.3.1).

## 4.3. Simulations of electron beam transport

The goal of this thesis was to investigate the emittance of electron beams generated by a laser-wakefield accelerator. As the chosen measurement was performed approximately 2 meters downstream from the accelerator exit, it is necessary to investigate how the beam is influenced over this distance. By using a particle tracking code [GPT], the electron beam can be simulated from the accelerator exit through the magnetic lenses to the YAG:Ce crystal beam-size diagnostic. The relevant parameters which affect the electron beam focusing (and potentially the retrieved emittance) are:

**Lens field aberrations:** A coupling between the transverse phase space planes leads to an unwanted exchange between them. The goal of the measurement is to make assertions about the beam emittance as it is when the beam leaves the plasma; coupling between the transverse planes should therefore be minimised.

**Lens positioning errors:** Transverse positioning errors such that the electron beam no longer passes through the magnetic centre of the lens. This leads to an additional dipole moment which deflects the beam and also means that the beam passes through the stronger lens aberrations at the outer parts of the aperture. Rotational errors of the lenses leads to coupling between the transverse planes.

Another important effect is space charge: although space charge forces are unavoidable and therefore not really "experimental errors", they do increase the emittance relative to its value at the accelerator exit which is the value to be determined. This effect was discussed in section 3.3.3 and is simulated with a tracking code in the experimental section 6.2.1.

### 4.3.1. Lens aberrations

Measured magnetic fields of lenses
Imaging errors and retrieved emittance
Chromatic effects

Chapter 3 discussed the origin of lens aberrations and that higher-order field components (HOMFCs) lead to coupling between the transverse phase spaces. This section investigates how the situation looks in real life by simulating an electron beam travelling through the beamline with the lenses positioned as in the experiment with magnetic fields taken from actual measurements. The experimentally derived emittances are increased by lens aberrations and therefore well-tuned quadrupole lenses improve the accuracy of the results. Only partially covered here is a realistic simulation of the effect of the fringe fields of the quadrupole lenses. Although the simulations here include the measured gradient fall-off as opposed to the simpler hard-edge model, the measured field only includes the transverse magnetic fields (radial and azimuthal). For a realistic simulation the longitudinal fields would need to be included which are especially relevant in the fringe-field region (outside of the physical extent of the lens).

From figure 4.5 it is clear that the beam size is largest in the second lens in the quadrupole doublet due to the defocusing of the beam in the vertical plane in the first lens. Lens aberrations become more important if an electron beam has a large beam size in the lens due to the dependence of HOMFCs on the radial distance from the magnetic centre. In the work of Becker et al. [2009] this dependence is shown experimentally by illuminating larger proportions of the lens aperture with an electron beam. It is therefore most important that the second lens of the doublet should have low aberrations. The decomposed magnetic fields of the lenses used in the experiment are shown in figures 4.6 (first lens, 25 mm long) and 4.7 (second lens, 15 mm long). This data was obtained as discussed in [Becker et al. 2009; Raith 2009]

by measuring the radial magnetic field on a circular path inside the lens aperture using a Hall probe. For the 15 mm lens an iterative tuning algorithm was applied to the lens to reduce the sextupoles (as described in the references above) which shows a reduction of the sextupole components without increasing the remaining HOMFCs. This leads to an improved imaging quality of the lens.

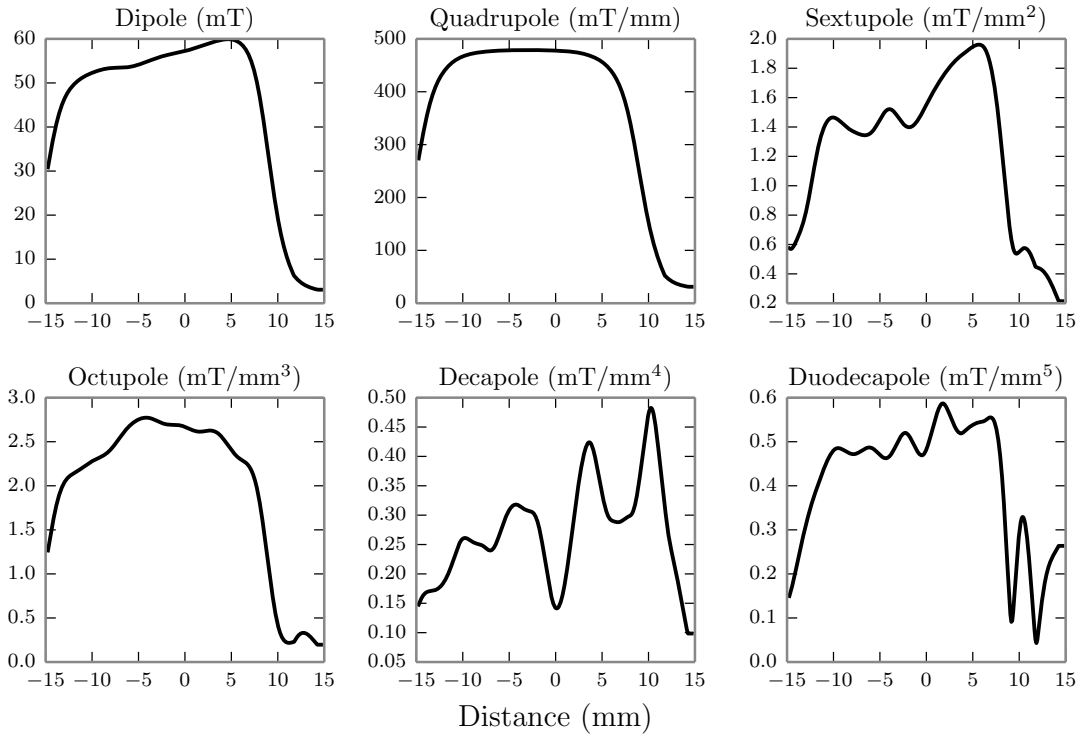


**Figure 4.6. – Magnetic multipole components of the 25 mm lens.** The magnetic field inside the lens is shown decomposed into its multipole moments. Due to the small beam size at this lens and the relatively small sextupole moment, the 25 mm lens was not tuned any further for the experiment.

### Effect on retrieved emittance

How do lens aberrations and the tuning effort affect the retrieved emittances in the experiment? To answer this a particle tracking code [GPT] was used to track an electron beam from its source at the accelerator exit through the **measured** magnetic fields of the lenses to the focus at the YAG:Ce crystal. Figure 4.8(a) shows the resulting beam size for untuned lenses and their "perfect" lens equivalents.

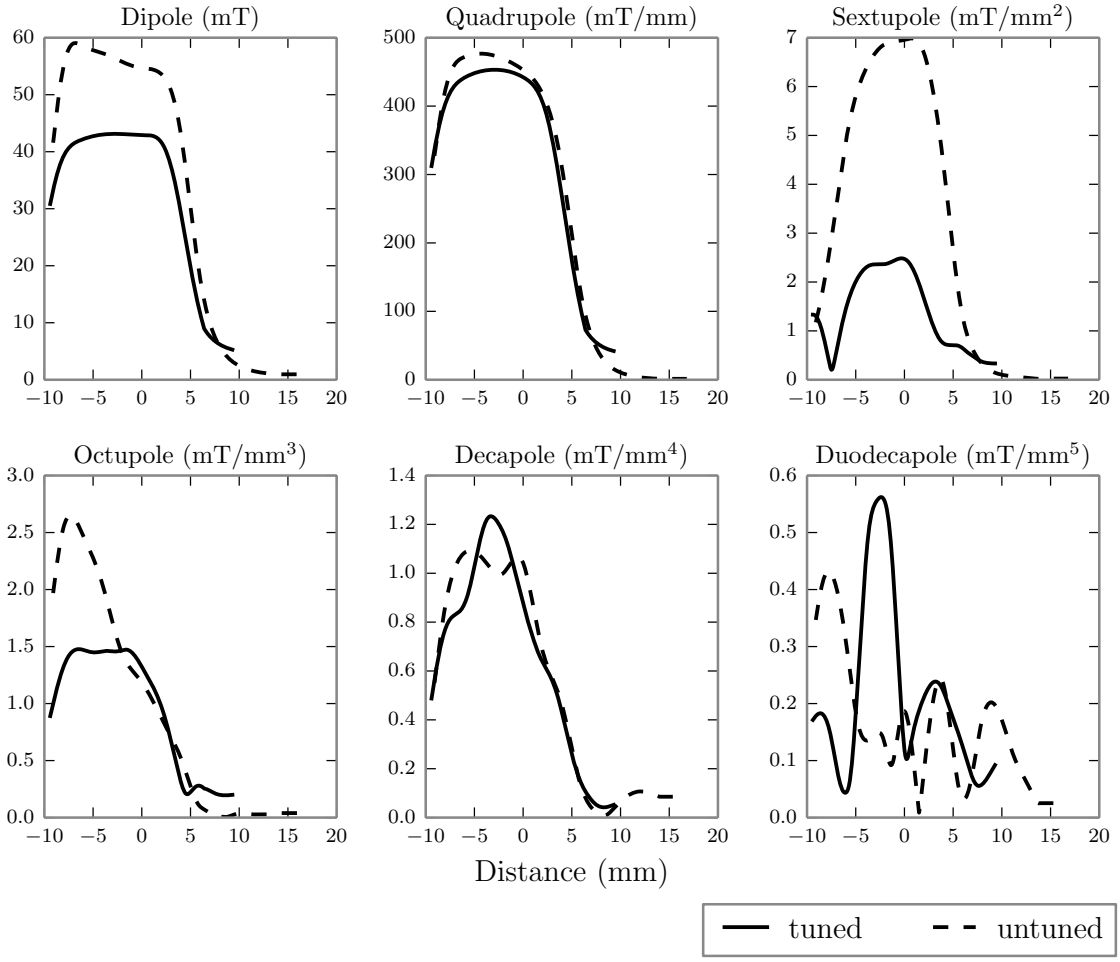


**Figure 4.7. – Magnetic multipole components of the 15 mm lens.** The magnetic field inside the lens is shown decomposed into its multipole moments. The tuning effort was focused on minimising the sextupole moment due to its strong impact on the imaging quality of the beam (see next figures)

The "perfect" lens equivalents are derived from the measured fields by removing all orders above the quadrupole in the simulation. This means that there is no coupling between the transverse phase spaces of the beam which improves the accuracy of the retrieval of the emittance in the horizontal plane. The retrieved emittance from the "untuned" lenses case is 3.1% larger than the "perfect" lenses case. The error arises almost exclusively from the larger beam focus which corresponds strongly to the retrieved source beam size. The flanks of the curves are very similar and hence the retrieved source divergence is not influenced as strongly by the HOMFCs.

Hence, sextupole components lead to an over-estimate of the source beam size and consequently also of the retrieved emittance. For the case of the tuned lenses the difference to the corresponding "perfect" lenses with no orders above quadrupole is only 0.7%. The lens aberrations were therefore disregarded in the retrieval of the emittance.

### Chromatic effects

As the focusing power of the magnetic lenses depends on the electron energy (see section 3.1.3), the position of the lens doublet needs to be adjusted for each energy to image from the electron beam source at the accelerator exit to the YAG:Ce crystal. Electrons with energies other than the target energy have a different beam size at the YAG:Ce crystal and would influence the emittance measurement if these electrons cannot be distinguished. To mitigate the influence of the large energy spread of the electron bunches, the emittance-retrieval experiment is conceived to be spectrally resolved; the beam size is measured behind a dipole magnet spectrometer and so each energy is dispersed to a different vertical position at the target plane. Nevertheless, in the experiment an overlap of energies is still expected which depends on the divergence and size of the electron beam source and the vertical acceptance used for the emittance analysis of electrons behind the spectrometer. In the data analysis all particles that are within 50 µm of the position for the nominal energy are included in the emittance calculation. This approximately corresponds to a vertical height of 20 pixel rows which are summed over in section 6.2 to obtain a good signal from which the emittance is retrieved. Figure 4.9 shows the energy distribution within the vertical acceptance around the nominal energy of 300 MeV for an electron beam with initial parameters of 0.9 µm (source size) and 0.4 mrad (source divergence). For this simulation the figure shows that basically all particles are within ±0.05 MeV of the nominal energy. According to the transfer function for the beamline, this corresponds to a difference in beam size of about 50 nm at the YAG:Ce crystal, a negligible difference compared to the total expected beam size of about 25 µm. For the measurements conducted at electron energies below 300 MeV, the larger dispersion of the spectrometer reduces the spread of energies within the vertical acceptance even further. This discussion shows why it is helpful to have a small vertical magnification. However for this experiment even the larger horizontal magnification ($M_{\mathrm{horizontal}} \sim 30$, $M_{\mathrm{vertical}} \sim 6$) would still result in a negligible spread of energies within the vertical acceptance window of 50 µm. Therefore this error, represented by $\sigma_{\delta E}$, will be neglected.

The previous paragraph discussed the effect of the electron beam *divergence* on the measured beam energy and beam width. For a freely drifting beam without magnetic lenses, the *pointing* of the electron beam will affect the absolute energy that is measured as the beam enters the dipole magnet with different angles and

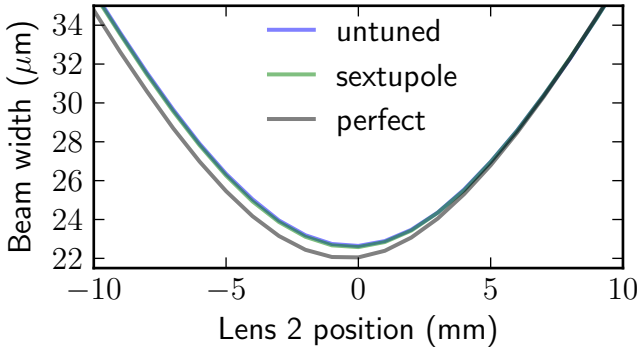


(a)

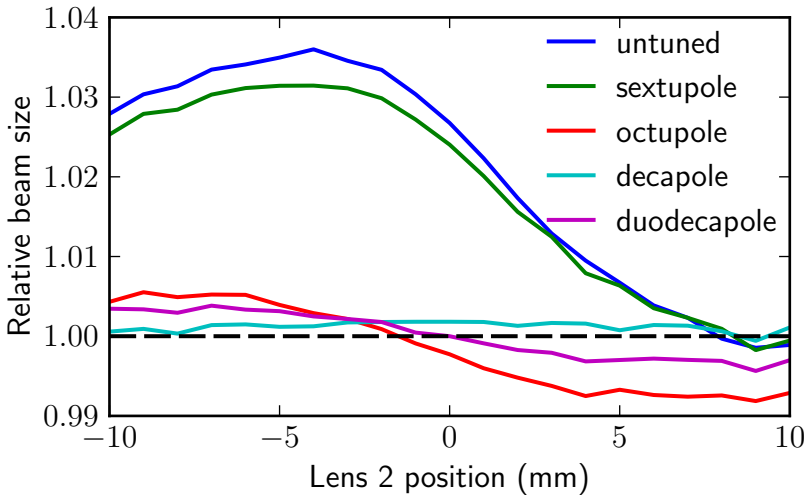


(b)

**Figure 4.8. – Simulation of the effect of lens aberrations.** a) Expected beam size at YAG:Ce crystal after a quadrupole doublet for a position scan of the second lens. The 'perfect' lenses line shows ideal beam imaging: all orders above quadrupole are removed from the measured magnetic field components of the lenses. The 'sextupoles' (green) line results when all orders above sextupole are removed, the blue line when no field components are removed (measured *untuned* lenses). b) The relative beam size (normalised to the beam size after a perfect lens system) when individual HOMFCs are added to the 'perfect' lenses. The sextupole component has the dominant effect of the unwanted multipoles; it alone increases the beam focus size by approximately 3%.

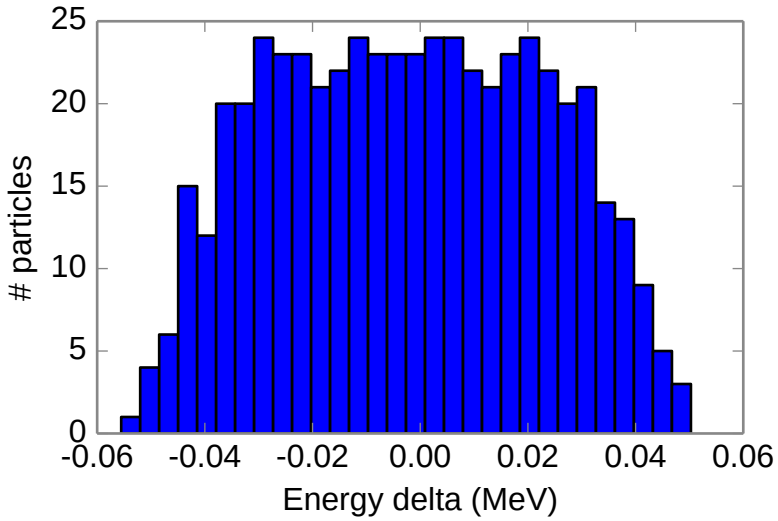


**Figure 4.9. – Distribution of electron energy offsets around nominal energy due to divergent electron beam.** The distribution results after tracking a uniform energy distribution through a quadrupole doublet and a dipole magnet spectrometer and taking the electrons within a $50\,\mu\mathrm{m}$ vertical window as used in the data analysis. The electron beam source has the same parameters as those obtained from the experimental data in table 6.1 for 300 MeV.

offsets from shot to shot. For a beam imaging system as used in this thesis, the beam pointing has virtually no effect on the measured energy: figures 4.10d and 6.2d show that for the imaged beam energy all pointing angles are imaged to the same point.

### 4.3.2. Misaligned lenses

Translation errors
Rotation errors

The previous section looked at the influence of lens errors on the electron beam focus at the YAG:Ce crystal. The focusing action of the lenses mainly depends on their magnetic fields and their $z$ (longitudinal) position. In the experiment motorised translation and rotation stages were used to position the quadrupole lenses. Ideally, the horizontal and vertical focusing planes of the two lenses are perpendicular to each other and the beam propagation axis passes through the magnetic centres of the lenses. The possible deviations from a perfect alignment come from errors in the $x, y, z$ positions and the angles $\alpha, \theta, \phi$ (also referred to as the pitch, roll, and yaw

angles, see fig. 4.1). As in the previous section, GPT particle tracking simulations with measured lens field maps will be used to look at how positioning errors affect the electron beam focus and the retrieved emittance.

### Transverse offset

In a perfect quadrupole field a transverse offset results in an additional dipole moment on top of the quadrupole field. A dipole moment "kicks" a beam transversely without affecting its transverse emittance, nor the longitudinal position of a downstream focus[i]. A dipole deflection happens whenever the beam axis and the lens axes do not align (see figure 4.10 b and c.)

In the experiment both transverse planes of the electron beam were imaged at the YAG:Ce crystal. This means that a transverse offset of the source (due to laser pointing fluctuations) or of the doublet system leads to a magnified offset at the YAG:Ce crystal (see figure 4.10c).

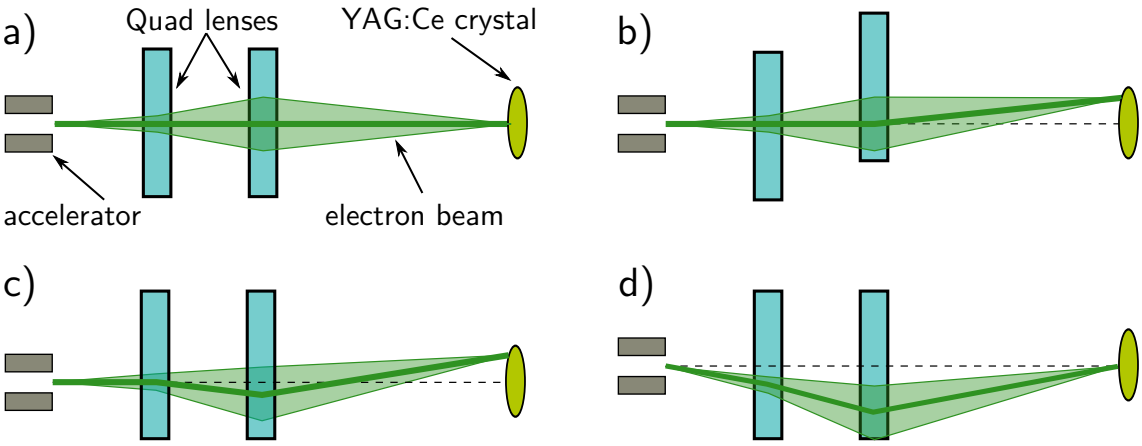


**Figure 4.10. – Offset of beam axis to lenses' axes.** The schematic drawings are valid if the lenses are positioned such that they image the object (electron beam source) to the YAG:Ce crystal. a) Perfect axes alignment. b) One lens transversely offset leads to an offset of the image. c) An offset of both lenses also results in an offset image. This is equivalent to a transverse shift of the object (electron beam source). d) If the source beam leaves the accelerator at an angle, the image position remains unchanged.

[i]More precisely, the beam's *path length* from the lens to its focus is not affected by a dipole. Therefore the longitudinal position is unchanged by the additional dipole provided that the transverse deflection is small compared to the distance to the focus.

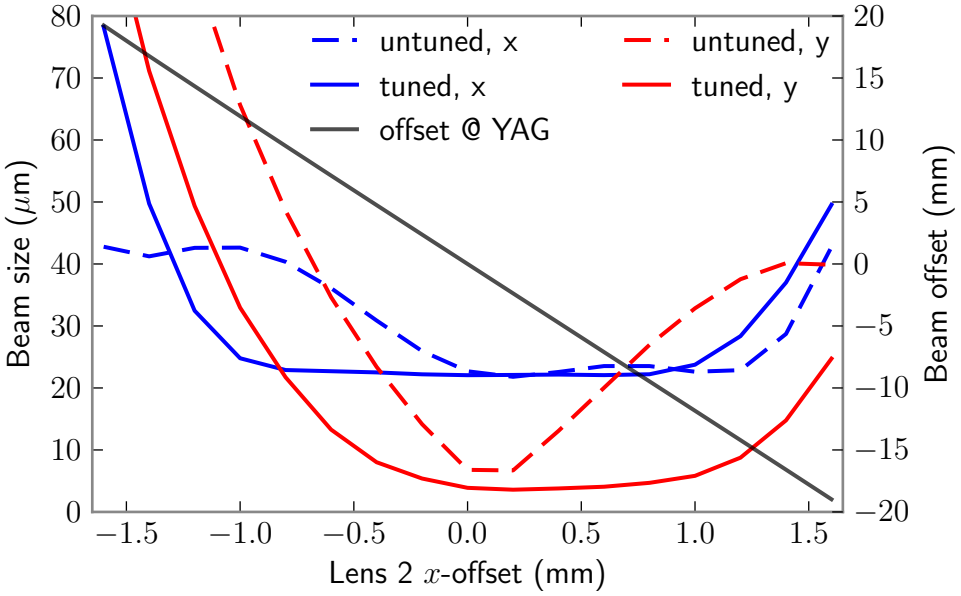


**Figure 4.11. – Effect of transverse lens offset on the imaged beam size.** Due to the lens offset, the beam passes through outer regions of the magnetic lens and therefore in general leads to a larger horizontal (blue lines) and vertical (red lines) beam size at the YAG:Ce crystal. The tuned lens (solid lines) show a larger plateau in which a transverse lens 2 offset has no effect on the beam size than the untuned lens (dashed lines).

For a realistic lens with lens aberrations the transverse offset also plays a role in the imaging of the beam. The beam envelope now passes through more outer parts of the lens aperture where the HOMFCs are stronger (compare a) and b) of fig. 4.10). For the tuned lenses as used in the experiments for this thesis, the focus size is smeared for offsets of $> \pm 0.8\ mm$ (see figure 4.11, the result is similar for an offset in $y$). Such a transverse lens offset and the corresponding dipole deflection would lead to a transverse offset of the beam of $\sim 5$ mm at the phosphor screen at S1 (see figure 4.1), and $\sim 10$ mm at the YAG:Ce crystal at S2. Such an offset is easily detectable even with the shot-to-shot fluctuations of the LWFA electron source. For 300 MeV electrons, a 10 mm vertical deflection would lead to an offset in the measured energy of 17 MeV. Such an energy offset would be noticeable in the experiment due to discrepancy between lens positions required to focus a particular energy (as a guide to the accuracy with which the electron beam energy is focused, see figure 6.2). Therefore by monitoring the energy offset and the transverse offset of the beam image, the transverse lens position can be optimised to eliminate smearing of the electron beam focus.

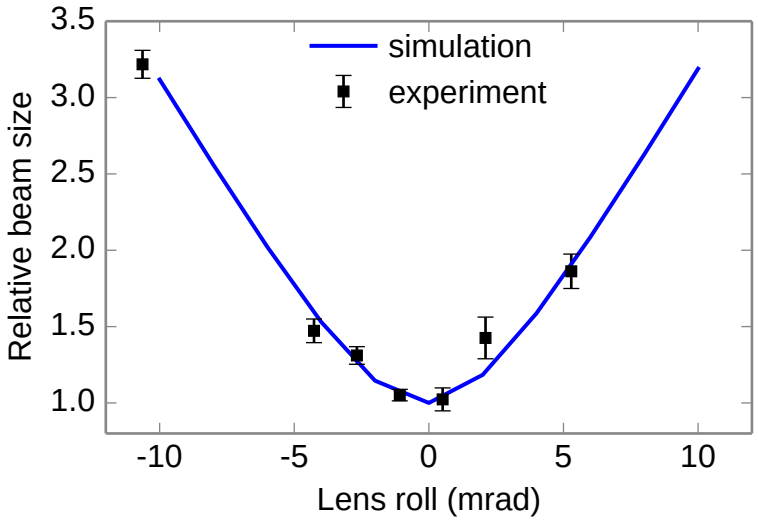


**Figure 4.12. – Effect of lens roll on the horizontal electron beam size at the focal position.** Lens 2 is rotated around the beam propagation axis. The simulation curve corresponds to a beam with a horizontal source size of $0.62\,\mu\mathrm{m}$ and a vertical divergence of 0.46 mrad. The error bars represent a standard deviation of the experimental data.

### Rotation errors

Figure 4.12 shows experimental data of the horizontal beam size at the target position when the roll of a quadrupole is scanned. It is the horizontal ($x$) source size which mainly determines the parabola "height" (the rms beam size at which the base of the parabola is), and the vertical ($y$) divergence which determines the parabola opening angle. This dependence is in contrast to the method shown in figure 3.13; where the parabola shape is determined solely by the horizontal electron beam source parameters. Figure 3.10 helps to understand why the divergence of the plane that is defocused by the first quadrupole has the dominant role in the parabola flanks in figure 4.12. A large source divergence leads to a large extent of the line focus after the first lens. Subsequently, the effect of a lens rotation is more severe on the size of the final beam focus. From figure 4.12 it can be seen that a lens roll angle of just 5 mrad will almost double the measured beam width at the YAG:Ce crystal and correspondingly increase the retrieved emittance. In the experiments for this thesis the roll angle was therefore carefully adjusted by scanning and finding the smallest horizontal beam size at the YAG:Ce crystal.

Fortunately, the other possible rotation errors, pitch and yaw, have very little effect on the focused beam size; for the present experiment alignment errors of 30 mrad only increase the beam size by 5%. This has also been found in other

practical applications involving PMQ lenses [Lim et al. 2005; Emma and Nuhn 2000]. As a result of the discussions regarding the transverse offset above, the experimental setup was realised such that both lenses could be independently positioned in $x, y, z$ coordinates by motorised translation stages and one lens to be rotated about the electron beam axis (roll angle).

## 4.4. Electron beam diagnostics

### 4.4.1. Dipole magnet spectrometer

To spectrally resolve the electron beams from the plasma accelerator a dipole magnet spectrometer is used. Electrons passing through a magnetic field will be deflected according to equation 3.1. The spectrometer is constructed such that the magnetic field is transverse to the beam axis and hence deflects the beam vertically. After an additional drift length behind the dipole magnet, the beam passes through a 2 mm thick stretch of aluminium to exit the vacuum chamber and through a scintillating phosphor screen. The emitted light from the scintillating screen is detected by a CCD camera. In this way the electron beam is separated from the laser beam which is important for detecting the relatively weak signal from the scintillating screen. The electron beam will scatter somewhat while passing through the 2 mm aluminium chamber door. According to equation 4.1, a 200 MeV electron beam has a scatter angle of 9 mrad after passing through the aluminium, which after 2 mm results in a spot size of 18 µm. Compared with the measured beam sizes on the order of $\approx$ 1mm and the resolution of the scintillating screen itself ($\approx$200 µm), this effect can be neglected.

The magnetic field of the dipole magnet (including the fringe field) was measured using a Hall probe. To calibrate the correspondence between electron energy and deflection, the measured field was included in a particle tracking simulation [GPT]. The results can be seen in figure 4.13. A weakness of this diagnostic is that the measured energy depends on the position and angle with which electrons enter the dipole magnet. For a LWFA electron beam source the large divergences and pointing angles of the beams will lead to incorrect spectral measurements. The problem can be addressed by imaging the electron beam from the beam source to the scintillating screen behind the magnet (see section 6.1.3).

### 4.4.2. Scintillating phosphor screens

The most convenient method for measuring the electron beam position and size is by using scintillating phosphor screens. They have a high light yield that is linearly proportional to the electron beam charge for many orders of magnitude [Buck et al.

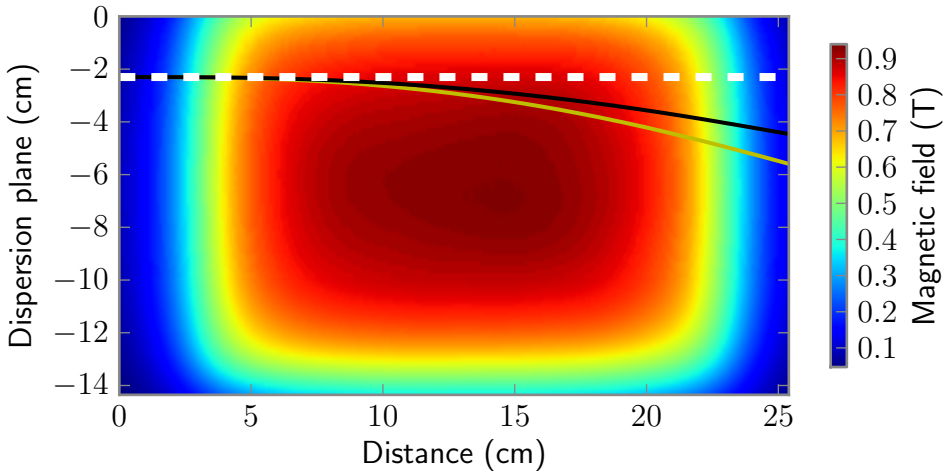


**Figure 4.13. – Calibration of the dipole magnet electron spectrometer.** The measured magnetic field of the electron spectrometer is fed into a particle tracking simulation: black line 300 MeV, yellow line 200 MeV, white line infinite energy. The simulated deflection along with the drift behind the spectrometer calibrates the spectrometer for the experiment.

2010]. The spatial resolution is relatively poor at $\sigma \sim 200\mu$m for the screens used in these experiments (CAWO OG 16 [CAWO, Website accessed: 08.10.2017.]), but sufficient to make meaningful beam profile measurements $\sim 1$ m after the accelerator exit (position S1 in figure 4.1).

### 4.4.3. Scintillating YAG:Ce crystal

Basic properties
Limitations to the spatial resolution

YAG:Ce crystals are used for high resolution beam profile measurements while still providing a relatively high light yield per beam charge. If the beam charge is too low, a phosphor screen (see previous section) with a higher light yield can be used (although with lower resolution). For high-charge beams, a setup using an optical transition radiation (OTR) screen provides the highest resolution. OTR screens are not suitable for beam profile measurements if the wavelengths that are detected are similar to the length of the emitting electron beam bunch itself. In this case the OTR can become coherent and the signal is no longer linearly but quadratically

proportional to the beam charge. For the case of LWFA electrons where the time profile of the bunch may have substructures, coherent and incoherent contributions to the beam profile signal may be difficult to distinguish.[ii].

| | |
|---|---|
| Chemical formula | $Y_3Al_5O_{12}$ |
| Index of Refraction | 1.82 |
| Wavelength of Peak Emission [nm] | 525 |
| Density [g/cm$^3$] | 4.57 |
| Radiation Length [cm] | 3.5 |
| Photon Yield [photons/MeV-deposited-energy] | $35 \times 10^3$ |
| Cerium Concentration (with respect to Y) | 0.18% |
| Decay constant [ns] | 70 |

**Table 4.2.** – Details of YAG:Ce crystal material [Crytur, Website accessed: 11.07.2011.]

Factors limiting the **spatial resolution of YAG:Ce crystals** have been discussed in the literature [Lumpkin et al. 1999; Murokh et al. 2000], the second reference also contains a basic review of the scintillation process itself. Resolution limiting factors can be put into two categories: collective beam effects and single-electron effects that are independent of the beam charge density.

**Collective effects:**

1. Saturation of the YAG:Ce crystal scintillation sites. If the number of electron-hole pairs in the crystal generated by the electron beam approaches or exceeds the number of scintillation sites, the signal will saturate.
2. Secondary particles showers. Ionised electrons from collisions are accelerated by the space charge field of the beam and in turn generate electron-hole pairs or further electrons/x-rays.

Lumpkin et al. [1999] compared the resolution of YAG:Ce crystals and OTR screens for a range of beam intensities, $\Sigma$, at the screen. The screens showed an equivalent spatial resolution for a focused beam of $40 \times 400$ $\mu$m size with 1.9 nC charge giving a beam intensity of $\Sigma = 0.2$ pC/$\mu$m$^2$. Murokh et al. [2000] comes to a value of $\Sigma \sim 0.04$ pC/$\mu$m$^2$ for the onset of resolution degradation due to

[ii] This aspect is an interesting method to determine the bunch duration. For LWFA electrons, bunches with lengths of ~5 fs and with a beam current of 5 kA have been measured using coherent transition radiation [Lundh et al. 2011].

collective effects for a YAG:Ce crystal. For the measurements of this thesis, electron beams were focused transversely to $\sigma_x \sim 20$ $\mu$m, and were energetically dispersed $\sim 1$ MeV/mm vertically (from the tracking simulations for the spectrometer). Given a measured spectral charge density of 0.2 pC/MeV [Popp 2011], results in a beam intensity of $\Sigma = 1 \times 10^{-5}$ pC/$\mu$m$^2$. As this beam intensity is many orders of magnitude smaller than for the above cases where collective effects become relevant, collective effects will be neglected for these measurements.

**Single electron effects:**

1. Scattering of electrons in the crystal increase the beam size.
2. Secondary x-rays and electrons causing additional scintillation in the crystal.
3. Depth of field blurring (discussed in section 4.4.4). The crystal is an extended radiation source as electrons generate light along its entire length as they pass through it. This extended source causes blurring at the detector depending on the details of the imaging optics.

The scattering of charged particles passing through matter (termed **multiple Coulomb scattering (MCS)**) was reviewed by Lynch and Dahl [1991]. They compared often-used approximate equations with Monte Carlo simulations based on a modified form of Molière scattering by Bethe [Bethe 1953] (which compares well with experimental data for heavy particles and is often also quoted for electron beams). They give the following as a good approximation for the rms scattered angle of a charged particle beam:

$$\theta_{MCS} = \frac{13.6}{p[\mathrm{MeV/c}]\beta}\sqrt{X/X_0}[1 + 0.088\ \log_{10}(X/X_0)] \tag{4.1}$$

with $p$ being the beam momentum, $\beta = v/c$ is the normalised beam velocity, $X$ and $X_0$ are the material thickness and radiation length respectively. It agrees to within 11% of the modified Molière theory for $10^{-3} < X/X_0 < 1000$. A 300 MeV beam passing through a 300 $\mu$m YAG:Ce crystal results in $\theta_{MCS} = 3.4$ mrad. This leads to an apparent increase of $\sigma_{MCS} \leq 1.0\mu$m for the rms beam size in the crystal, where the equality is valid for the apparent beam size *at the exit of the crystal*. The detected scintillation signal is generated by the electron beam along the entire crystal length, therefore $\sigma_{MCS} = 1.0\mu$m represents an upper limit.

As the electron beam propagates through the crystal, it generates **secondary particles** called knock-on electrons and photons, or $\delta$-rays (delta-rays). Secondary photons are emitted due to *Bremsstrahlung* of the beam electrons and are emitted in a cone with angle $1/\gamma$ relative to the electron path. For an incoming 300 MeV beam this corresponds to an angle $\theta_{Brems.} = 1.7$ mrad or an apparent increase of the

rms beam size of $\sigma_{Brems.} \leq 0.5\mu$m. As for the case of MCS above, the equality is an upper limit as it represents the beam size at the exit of the crystal. Low energy secondary electrons from Coulomb interactions with the beam can be scattered at larger angles and subsequently cause scintillation far from the primary electron, resulting in a transverse smearing out of the signal. The amount of smearing depends on the distance that a secondary electron can travel away from the primary electron in the crystal before exciting a scintillation site. The average path length of an electron in a material until it comes to rest (often called "range") is a function of its initial kinetic energy. The range of secondary electrons is shown for the case of fast electrons in a YAG:Ce crystal in figure 4.14(a). Figure 4.14(b) shows the spectrum of secondary electrons generated by an incident ultra-relativistic electron per distance travelled in a YAG:Ce crystal as calculated with [Nakamura 2010; Grupen 2001]

$$\frac{d^2N}{dTdx} = 2\pi r_e^2 m_e c^2 N_A \frac{Z}{A}\frac{1}{\beta^2 T^2}\rho. \tag{4.2}$$

Here $N$ is the number of generated secondary electrons, $T$ is the kinetic energy of the secondary electrons, $x$ is the distance travelled in the scattering material, $r_e$ the classical electron radius, $m_e c^2$ the electron rest mass energy, $N_A$ Avogadro's number, $Z$ and $A$ are the atomic number and weight, and $\rho$ is the material density. This equation is derived from the Coulomb scattering of two charged particles and neglects the binding energy of the secondary electrons to their parent ions. This assumption is valid as long as the transferred energy is much larger than the so-called mean excitation energy, $I$, of the material i.e. $T \gg I$ which is fulfilled above 1 keV.

By integrating equation 4.2 one arrives at a formula for calculating the number of secondary electrons generated along the length of the crystal with an energy above a given energy $T_1$:

$$\begin{aligned} P(T > T_1) = & \int_0^l dx \int_{T_1}^{T_{max}} \frac{d^2N}{dTdx} dT \\ \approx & 153\ \frac{\rho[g/cm^3]}{\beta^2}\frac{Z}{A}\frac{l[cm]}{T_1[keV]}. \end{aligned} \tag{4.3}$$

Here $l$ is the length of the scattering material, and $T_{max}$ the maximum possible transferred energy [iii].

To introduce a 3% error in the measurement of a 20 $\mu$m electron beam focus, a resolution error of $\sigma_\delta = 5\mu$m would be required (assuming Gaussian addition of

[iii] Half of the primary electron's kinetic energy due to the indistinguishability of primary and secondary electron.

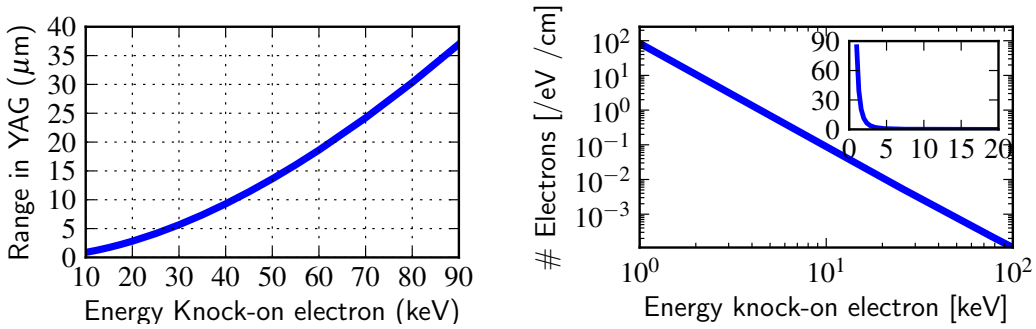


(a) (b)

**Figure 4.14. – Properties of secondary ("knock-on") electrons in YAG:Ce crystal.** a) Range of fast electrons in a YAG:Ce crystal. The stopping power (energy loss per distance travelled in the material) and the resulting range of the electrons were calculated using [NIS]. b) Spectrum of secondary electrons per unit energy bin generated by a single incident ultra-relativistic electron travelling a unit length in a YAG:Ce crystal (inset: main plot with linear scale).

errors). According to figure 4.14(a), this requires secondary electrons with an energy of >25 keV. Using equation 4.3, it can be calculated that each electron produces $P(25\text{ keV}) = 0.39$ secondary electrons with an energy sufficient to travel 5 $\mu$m or more. To judge whether such secondary electrons will smear the main beam profile, the deposited energy of each is considered as this is directly related to the number of scintillated photons (see table 4.2). The energy of the secondary electrons generated by each incident beam electron is approximately $0.39 \times 25\text{keV} \sim 10\text{keV}$. The energy deposited by electrons from the main beam can be obtained from the stopping power using [NIS]: for 300 MeV electrons, a YAG:Ce crystal of length 300 µm with a density of 4.57 g/cm$^2$ the deposited energy is 2.7 MeV per electron. As the deposited energy from "harmful" secondary electrons is 1/270 for this rough calculation, their effect on the degradation of the spatial resolution of the YAG:Ce crystal can therefore be neglected.

### 4.4.4. Optical imaging of the electron beam focus

Diffraction limit
Depth of source and optical aberrations

The light generated by the electron beam passing through the YAG:Ce crystal needs to be carefully imaged to obtain an accurate measurement for the beam focus size. The optical imaging setup is shown in figure 4.15. This section shows the

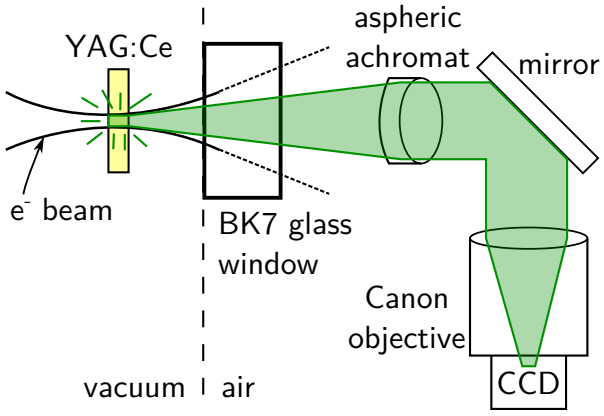


**Figure 4.15. – Setup for observing electron beam focus.** The $\sim 20\,\mu m$ electron beam focus passes through a YAG:Ce crystal and deposits a small amount of energy; some of which is emitted as light in all directions with a peak wavelength of about 530 nm. Part of the emitted light passes through a BK7 glass window out of the vacuum chamber and is collected by an Edmund optics f/2 50 mm aspheric achromat and together with a Canon f/2 135 mm camera objective (both working at an infinite conjugate ratio), is imaged to a CCD camera.

influence of various optical effects to justify how the imaging setup was chosen for the experiments. For an optical imaging system it is convenient to define a **point-spread function (PSF)**. The PSF is the observed light pattern at the image plane from a point light source at the object plane. The PSF is a system response of the imaging system and depends entirely on the imaging system (lens aberrations, alignment errors etc.) and *not* on the object being imaged. The convolution of the real object with the PSF gives the image observed at the image plane. Conversely, if the PSF of the imaging system is known, the observed image can be deconvoluted to obtain the original object. In the following sections the PSF of various optical effects are discussed.

### Diffraction limit

The resolution of a conventional optics system is ultimately limited by diffraction which depends on the light wavelength and the acceptance aperture of the imaging system. For the case of circular lenses, the image of a point source object is given by the Airy pattern [Hecht 2002], which is plotted in figure 4.16 together with a Gaussian curve. The width of the Airy function as well as a Gaussian approximation to it are given by

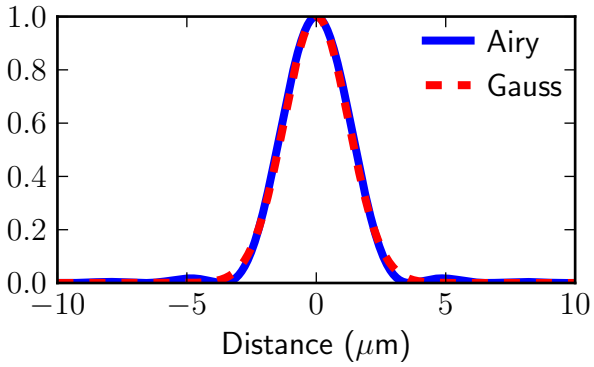


**Figure 4.16. – Airy function and Gaussian approximation.** This plot shows the point spread function due to diffraction for the imaging system used in the experiment ($\lambda = 530$ nm, $f = 135$ mm, $D = 25$ mm.)

$$w_{\text{diffr., Airy}} = 1.22\lambda \cdot \frac{f}{D}, \tag{4.4}$$

$$\sigma_{\text{diffr., Gauss}} = 0.42\lambda \cdot \frac{f}{D}, \tag{4.5}$$

where $f$ and $D$ represent the focal length and the lens aperture respectively. The width of the Airy function, $w_{\text{diffr., Airy}}$, is defined as the distance from the centre of the image to the first zero of intensity; for the Gauss curve $\sigma_{\text{diffr., Gauss}}$ is the rms width.

As a rough estimate, both lenses are considered to be perfect, and a plane wavefront of diameter 25 mm (the size of the first lens) falls on the camera objective with a focal length of 135 mm. Using the Gaussian approximation to the Airy function (equation 4.5), and the central wavelength emitted by the YAG:Ce crystal of 530 nm, results in $\sigma_{\text{diffr.}} = 1.2\,\mu\text{m}$.

### Depth of field and optical aberrations

An optical imaging system images from the object to the image plane. If the object is three dimensional, then parts of it will extend past the object plane where the resolution is highest. Some blurring will occur for these other parts of the object and is connected with the depth of field of the imaging system; this becomes more severe for low f-number (large aperture) imaging systems such as the case here. By shifting the optics setup and determining the resolution as a function of position, an approximate value for the resolution due to the depth of field and optical aberrations

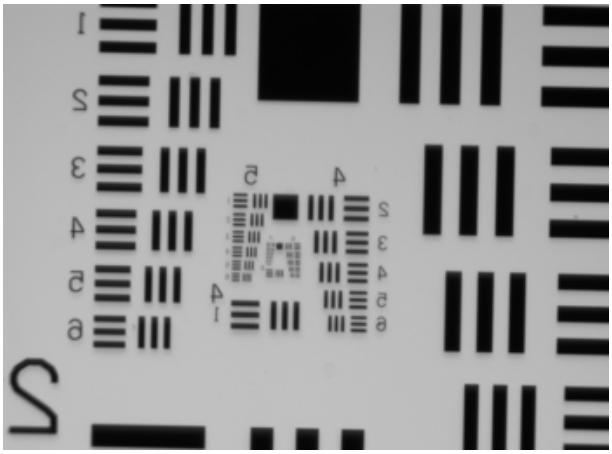

**Figure 4.17. – USAF 1951 spatial resolution test pattern.** The pattern consists of groups with each six elements each in turn consists of three bars. The line pairs per millimetre value refers to the width of one black and one white bar.

can be specified by taking the average over the length of the object. To measure the resolution, the measured contrast of the stripes of a USAF pattern (see fig. 4.17) is compared to a convolution between a series of step functions (which represent the USAF pattern) with a Gauss function (representing the point spread function of the optics that is to be determined). The system resolution is found when the contrast of the measured and the convolution cases match. The results for a lens that is 75 µm offset from the optimum position are shown in figures 4.18 and 4.19, giving a resolution width of 4.2 µm. Figure 4.20 shows the results for a range of optics positions. Taking the average of the resolution function over the optical length of the crystal gives $\sigma_{DO} = 3.5\,\mu\text{m}$. This empirical method also includes any optical aberrations of the lens system. The above setup has also been simulated with the Zemax [zem] ray tracing software. The depth of field effect is much smaller in the simulation at approximately 1 µm. Although the simulation approximates the camera objective as a perfect lens, the difference to the measured value seems surprisingly large. For the analysis in this thesis the lower resolution of 3.5 µm obtained from the measurement will be used.

Of the errors discussed in this section, the effect of depth of field of the imaging optics is the dominant effect. The associated estimated point spread function will be used to deconvolute the measured beam size at the YAG:Ce crystal. The errors arising from the imperfect lenses depend on less predictable factors such as the size of the beam in the lenses. Therefore these errors decrease the accuracy of the measurement, but will not be included in the deconvolution of the measured data.

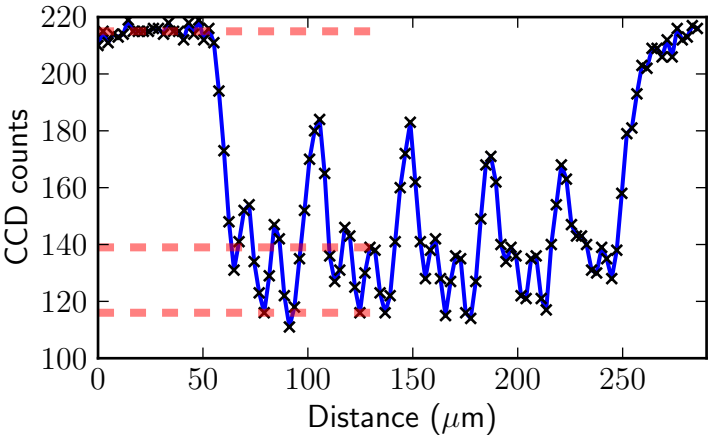


**Figure 4.18. – Lineout of USAF resolution pattern.** Measured CCD counts along a column passing through group six of the USAF resolution pattern. The individual elements of the group are each the two small peaks between the large peaks. For this lineout the optics were offset by $75\,\mu\mathrm{m}$ from the highest resolution (this corresponds to one offset on the horizontal axis of figure 4.20). The contrast is measured for element three (second from the top for even groups) using the red dashed lines giving a value of approximately 0.77 for this case.

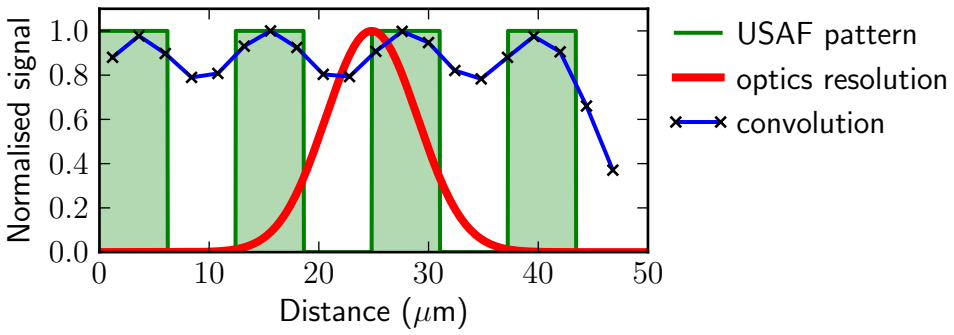


**Figure 4.19. – Determining the spatial resolution.** The USAF pattern (green, USAF group six, element three = 80.6 lp/mm) is smeared out by the optics point spread function (red) via a convolution of the two. The convolution function is sampled by pixels of finite size (black crosses connected by blue line). A point spread function width of $4.2\,\mu\mathrm{m}$ rms gives a contrast matching that in figure 4.18.

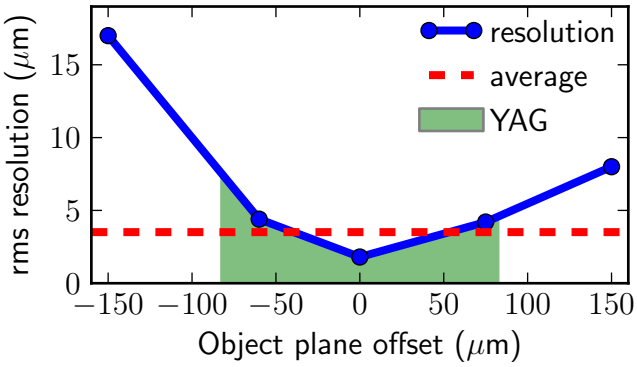


**Figure 4.20. – Effect of the offset of the object plane position on the resolution of the optics system.** The USAF pattern served as an object at different offset positions. The resolution averaged over the optical length of the YAG:Ce crystal (the optical length is the physical length divided by the refractive index, $300\,\mu\mathrm{m}/1.82$) is $3.5\,\mu\mathrm{m}$ (red line). The resolution deteriorates faster if the collimating lens is too close to the crystal (negative offset) than if it is too far away.

# 5. Experimental results of laser-wakefield acceleration

This chapter presents the electron beams obtained from the laser-wakefield acceleration setup shown in the previous chapter. The results in this chapter have been discussed previously in the following publications: [Osterhoff et al. 2008; Osterhoff 2008] (steady-state gas cell) and [Popp 2011] (variable-length gas cell). The initial experiments for deploying the miniature quadrupole lenses were conducted with the steady-state gas cell, whereas the emittance measurements were carried out with the variable length gas-cell. Those experiments are presented in the next chapter.

## 5.1. Electron beam energy spectrum

Initial experiments at the Max-Planck Institut für Quantenoptik used a capillary with an electrical discharge as a gas target for LWFA experiments. The electrical discharge was used to pre-ionise the hydrogen gas which then relaxed to a radial parabolic density profile which guided the laser and the acceleration process over many Rayleigh lengths. Although high electron energies were achieved [Karsch et al. 2007], the fluctuations of the electrical discharge also led to unstable electron beams. The stability was greatly improved by operating the capillary without the electrical discharge and using a reproducible gas density profile [Osterhoff et al. 2008]. The electron beams from this configuration typically had a plateau spectrum up to $\sim 200$ MeV with a peak at this energy (see figure 5.1). The diameter of the gas-cell did not play an important role in the generated electron beams as capillaries of different diameters led to similar experimental results. The stability of the generated electron beams enabled many experiments. These included investigating the effect of the pulse-front tilt of the laser beam on LWFA [Popp et al. 2010], the generation of soft X-ray radiation from a magnetic undulator [Fuchs et al. 2009], the imaging of these beams using magnetic lenses [Weingartner et al. 2011], and the measurement of the electron beam emittance [Weingartner et al. 2012].

Using an upgrade of the ATLAS laser led to higher-charge beams at higher energy. Additionally, a variable-length gas-cell was used to explore the dynamics of the acceleration process. The results and in-depth analysis of this work can be found in Popp [2011]; relevant aspects for this thesis are described in the following.

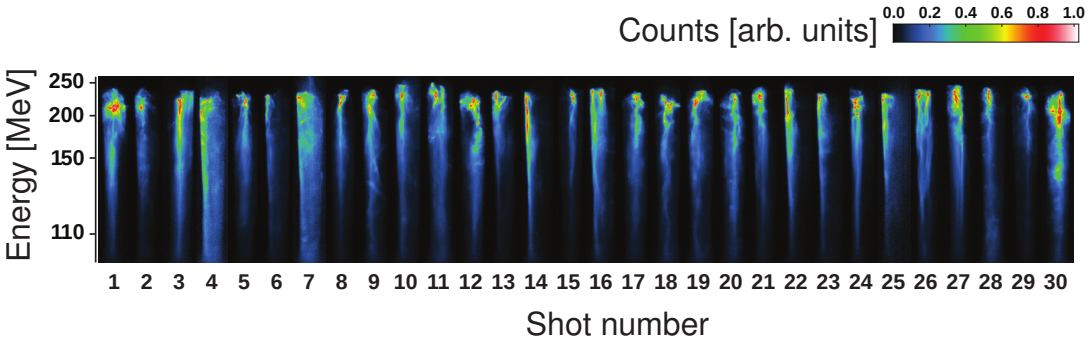


**Figure 5.1. – Steady-state gas cell electron beam spectra.** 30 consecutive electron beam spectra obtained with the steady-state gas cell (15 mm long). The vertical axis shows the beam energy due to the dipole magnet dispersion. The horizontal axis shows the divergence in the horizontal plane in the experiment. The colour scale is linearly correlated with charge. Figure taken from [Osterhoff 2008].

Figure 5.2 shows electron beam spectra measured for a range of accelerator lengths. A typical shot had a plateau spectrum with charge 0.2 pC/MeV up to an energy of 350 MeV. At this energy there was typically a peak on top of the plateau with 0.4 pC/MeV and an rms energy spread of 6% containing an integrated charge of 15 pC. Because of the fluctuations in the peak electron energy, the emittance measurements in the following chapter were conducted slightly below the 350 MeV peak to ensure that sufficient charge was available for every shot. Evident in the data is the continuous acceleration (until ∼4 to 5 mm) and the dephasing and breaking up of the electron beam beyond this. The dephasing length can be obtained by analysing the high-energy cut-off energy of the spectra. These highest-energy electrons are expected at the head of the electron bunch in the plasma bubble and have therefore "sampled" most of the longitudinal electric field of the bubble. For example, for an electron density of $6.5 \times 10^{18}\mathrm{cm}^{-3}$, the cut-off energy showed a parabolic dependence with acceleration length[i] and started to decrease from about 4.9 mm [Popp 2011]. Beyond this length, the laser had lost sufficient energy that it could no longer drive a strong plasma wave. The electron beam itself had sufficient charge to drive a plasma wave and slowly lost energy with increasing accelerator length.

A scan of the plasma density revealed that the accelerated charge increases with density (figure 5.3). This relationship is as expected from the consideration of the required longitudinal momentum for an electron to be trapped by the plasma potential and also the reduced plasma wave velocity discussed in section 2.4. From 1D theory the resonant laser pulse length for driving the plasma wave is $\mathrm{L}_{FWHM} \sim 0.37 l_p$ for

[i] As expected from a linear electric field along the bubble axis as in figure 2.2.

a Gaussian-shaped beam in time (Esarey et al. [2009]). The pulse length of the ATLAS laser of 23 fs will resonate with a plasma density of $\sim 3 \times 10^{18}\mathrm{cm}^{-3}$. Above this density a lower accelerating field is expected hence also the lower electron energies. Previous work has shown a decrease in stability of electron beams above the resonant driving density [Osterhoff 2008] due to filamentation of the laser. Filamentation cannot be seen in the spectra shown here, however the stability decreases above a density of $\sim 4 \times 10^{18}\mathrm{cm}^{-3}$.

By plotting the high-energy cut-off of the beams against acceleration length, the parameters of the accelerating field could be determined [Popp 2011]. For a density of $6.5{\times}10^{18}\mathrm{cm}^{-3}$ (130 mbar), the calculated accelerating field at the point of injection was $\sim 160$ GV/m and decreased linearly with 34 MV/mm$^2$. The dephasing length was found to be 4.9 mm with a cut-off energy of 380 MeV. This gives an average accelerating field over one dephasing length of $\sim 79$ MV/mm.

## 5.2. Spatial beam characteristics

### Electron beam pointing and divergence

By observing the electron beam before the dipole magnet the divergence and pointing can be measured. A single shot behind the steady-state capillary target is shown in figure 5.4. It has an FWHM divergence of 1.6 mrad. The average over 20 consecutive shots gives a mean divergence of 2.1 mrad FWHM and pointing fluctuations of 1.8 mrad rms. Interestingly, the later experiments conducted with the variable-length gas cell show a significantly smaller divergence of $\lesssim 0.5$mrad rms using the same diagnostics. Using more sophisticated methods[ii] divergences as small as 0.40 mrad were observed. This is amongst the smallest electron beam divergences published to-date for LWFA. The small divergence can be explained by adiabatic damping of the beam during its transition to vacuum (see discussions in sections 2.6 and 6.2.7).

### Electron beam spectral divergence

From the spectra shown in figures 5.1, 5.2, and 5.3, a spectral divergence in the horizontal plane can be obtained. The spectral divergence for three example shots is shown in figure 5.5. As is stated in the figure caption, a majority of shots shows a larger divergence at or beyond the spectral peak which is relevant for the discussion surrounding figure 6.6.

[ii] Quadrupole scan, results discussed in section 6.2.1.

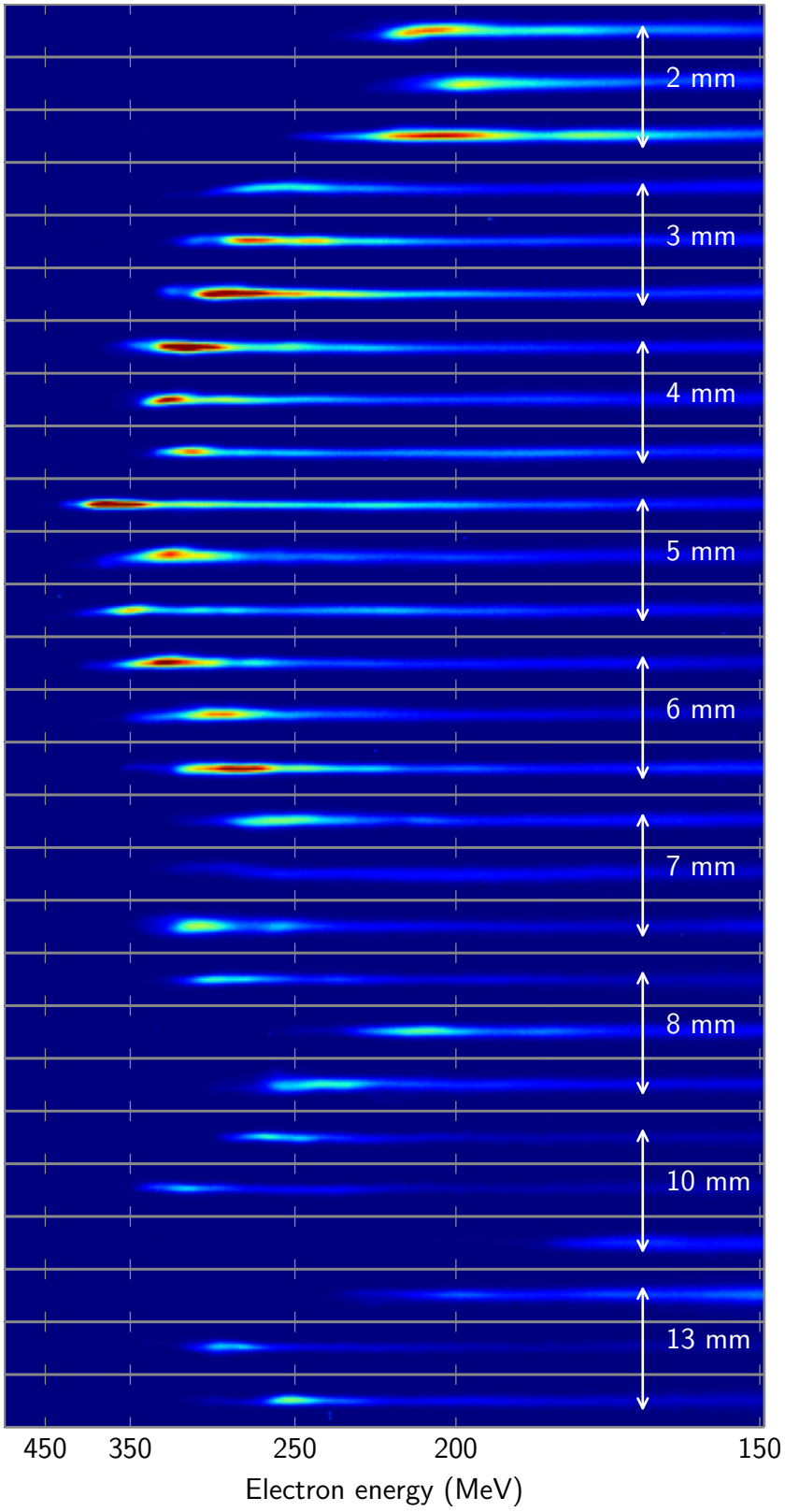


**Figure 5.2. – Accelerator length scan.** Consecutive shots for various lengths of the adjustable gas-cell at a density of $6.5 \times 10^{18}\mathrm{cm}^{-3}$ (130 mbar). Dephasing/depletion of the high-energy peak occurs around 6 to 7mm. The colour scale is the same for all shots and the same as in figure 5.3.

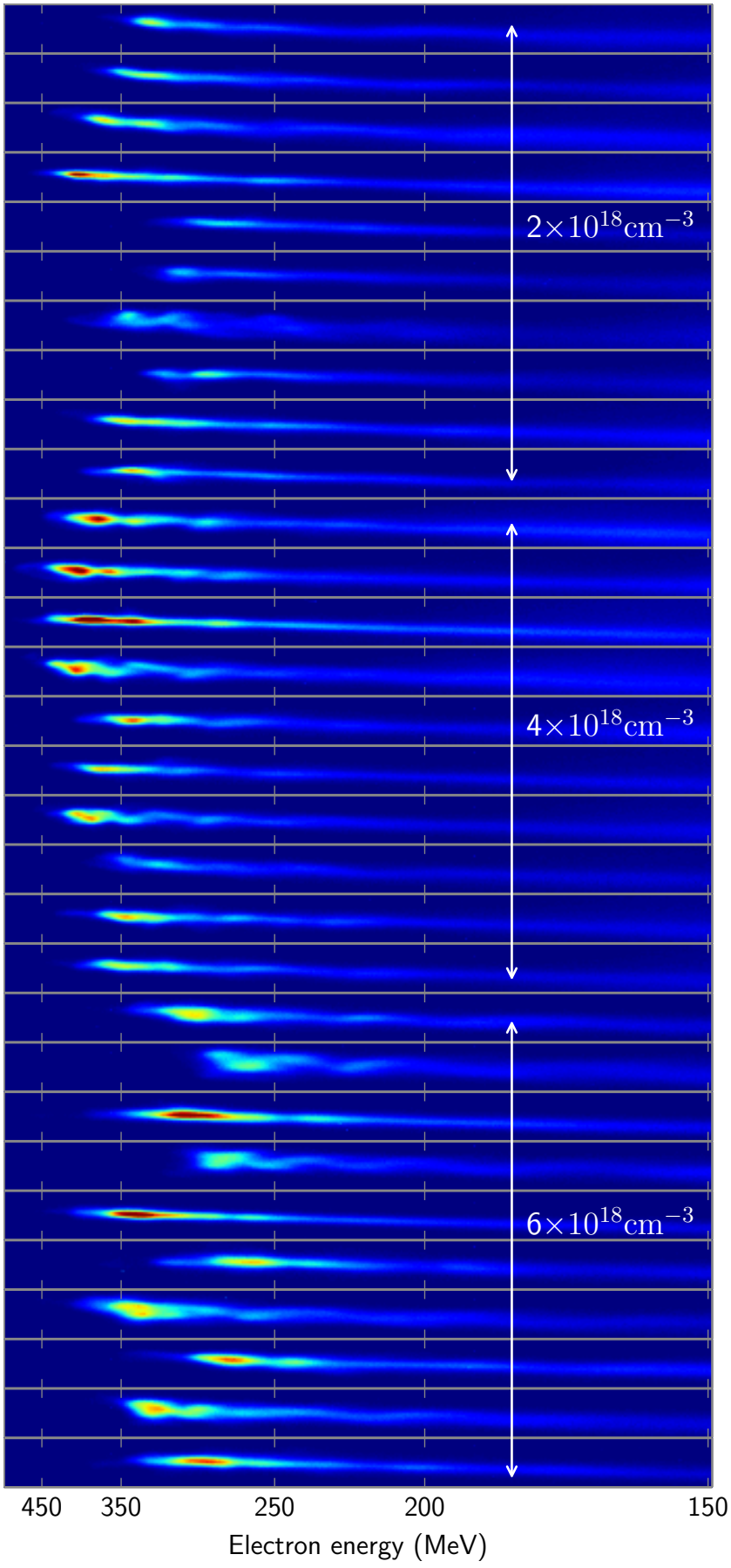


**Figure 5.3. – Accelerator plasma density scan.** Consecutive shots for a 6 mm acceleration length

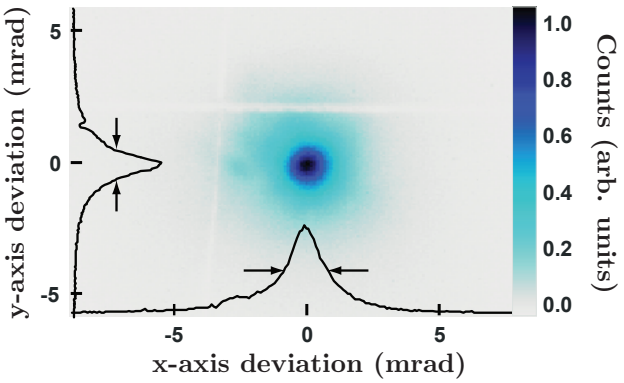


**Figure 5.4. – Electron beam divergence.** Transverse profile of a single electron beam observed on a scintillating phosphor screen ∼1 m behind the accelerator. The beam profile is not spectrally resolved and therefore contains all electron energies of the beam. Illustration taken from [Osterhoff 2008].

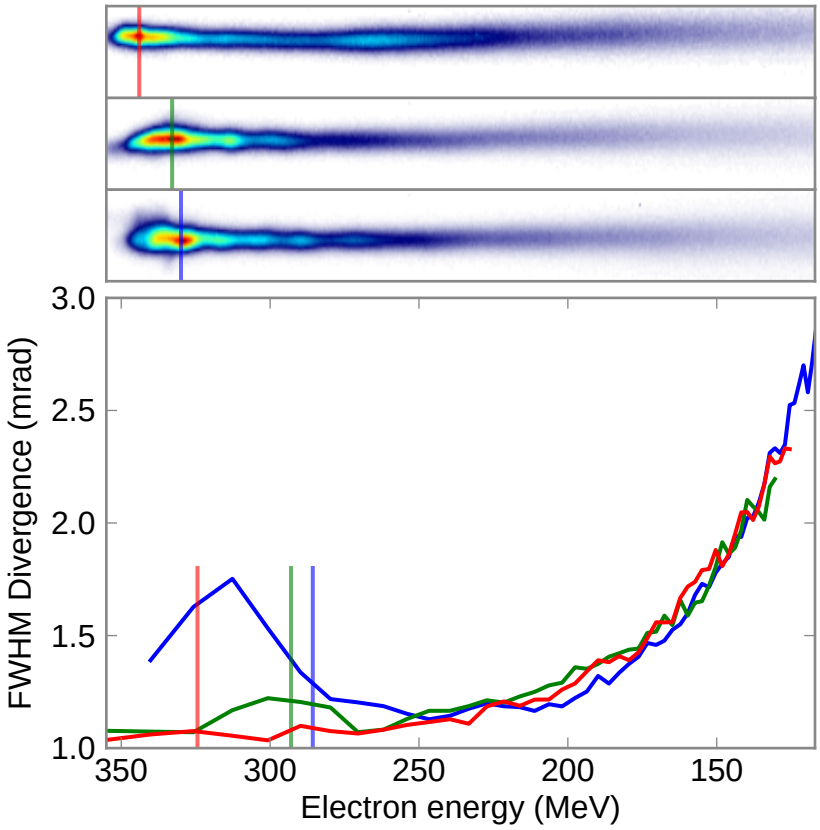


**Figure 5.5. – Electron beam divergence spectrally resolved.** Three individual shots are shown (top three images) and their respective divergence behind the spectrometer (bottom plot). The vertical lines indicate the energy with the highest charge density ("spectral peak"). These three shots have been chosen to demonstrate three different categories of shots: 1) no divergence change around the peak (red peak, ∼40% of shots), 2) local divergence maximum at the spectral peak (green peak, ∼50 % of shots), or 3) a larger divergence at the cut-off energy beyond the spectral peak (blue peak, ∼10% of shots). Note that the energy scale of the bottom plot is linear, whereas for the top three plots it is not linear.

# 6. Measurements of the electron beam emittance

In this chapter the experimental measurement of the electron beam emittance is discussed. The measurement method was detailed in section 3.4 and relies on electron beam imaging using magnetic quadrupole lenses. The first part of this chapter therefore explores the imaging process itself and the second part the emittance measurement.

## 6.1. Beam transport of LWFA electrons

The results presented in this section were published in [Weingartner et al. 2011].

Of practical importance is the ease with which quadrupole lenses can be aligned in the experiment. First the longitudinal position of the lenses is set according to simulation results for the target energy. Next the transverse position of the lenses with respect to the beam propagation direction must be adjusted. The fact that a transversely-offset lens introduces a dipole magnetic field is used by observing the beam position before and after a lens has been moved into the beam. If the beam stays at the same position for each lens independently, it can be assumed that the beam propagates through the magnetic centre of the lens doublet and is not deflected by either lens. The difficulty of this alignment procedure results from the inherent fluctuations of the pointing of the electron beam from the plasma. This makes a single shot through a lens inconclusive about the exact transverse position of the lens due to the fact that both the lens and the beam can have an offset to the target propagation axis. This can be resolved by taking statistics over a series of shots and observing a trend. It is also possible to observe the beam after it has been dispersed by the dipole spectrometer: if the dispersed beam is consistently tilted in one direction, a dipole field from the quadrupole lenses is deflecting the beam. As the magnitude of the deflection depends on the electron energy, a tilted spectrum is observed.

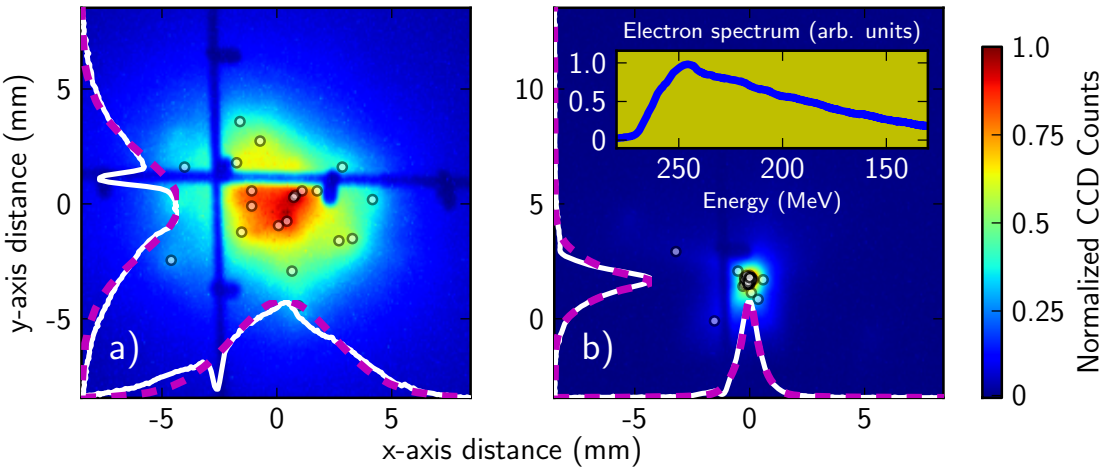


**Figure 6.1.** – **Electron beam spatial stability improvement:** False colour images observed at S1, 1.12 m behind the source (experimental sub-figures are each normalised to one). a) Sum of 20 consecutive electron beams and peak positions of each shot (dots). Shot-to-shot pointing fluctuations as well as the beam divergence lead to FWHM widths in the summed signal of $5.3 \times 5.2$ mm (x-axis $\times$ y-axis). b) Sum of 47 consecutive electron beams with a magnetic lens doublet set to collimate 220 MeV electrons, the FWHM widths are reduced to $0.9 \times 1.2$ mm (x-axis $\times$ y-axis). The inset shows a sum of 30 electron beam spectra taken shortly before. Despite the chromaticity of the magnetic lenses, the beam collimation is still effective even with an FWHM energy spread of 80 MeV ($\sim$35%). Results from particle tracking are shown as lineouts (magenta dashed lines) which have already been convoluted with the instrument function of the detection system of S1 to allow a direct comparison with the experimental lineouts (white solid lines).

### 6.1.1. Spatial stability improvement of LWFA electron beams

LWFA electron beams exhibit large pointing fluctuations on the order of $\gtrsim$1 mrad rms (see section 5.2). This results in a different transverse position of the electron beam on target from shot to shot and will decrease the stability of subsequent experiments. By imaging the beam with quadrupole lenses, both the spot size and the shot-to-shot position fluctuation on target can be reduced. To quantify the effect of imaging the beam, the size of the summed signal of many shots observed at S1 (1.12 m behind the gas cell) was compared with and without PMQ lenses (figure 6.1). The summed beam size at S1 arises from the electron beam pointing and divergence and for the case where PMQ lenses are used, also the combination of the beam energy spread and the lens chromaticity. Figure 6.1(a) shows the sum of 20 consecutive electron beams and their respective peak positions without PMQ lenses. The summed signal has a FWHM width of $\sim$ 5.2 mm resulting from pointing insta-

bilities of 1.8 mrad rms (defined from the peak positions) and a mean divergence of 1.7 mrad FWHM. Figure 6.1(b) shows the sum of 47 consecutive shots with a PMQ doublet positioned to collimate 220 MeV electrons resulting in an FWHM width of $0.94 \times 1.20$ mm (x-axis $\times$ y-axis), approximately a factor of five smaller than the freely drifting beam. This reduction in spatial fluctuations was successful despite the large range of electron energies (260 to <150 MeV) measured in the experiment (see figure 6.1(b) inset). To confirm these results, simulations were performed for a freely drifting beam and for a beamline with a quadrupole doublet. The simulation tracked an electron beam with the measured energy spectrum and a fixed divergence such that the freely drifting beam matches the experiment[i]. The tracked electron beam spot was convoluted with the instrument function of the detector at S1 (assumed to have a Gaussian shape), where the width is determined by the graininess of the phosphor screen and the resolution of the optical imaging system observing the screen giving a combined resolution of $\sigma \sim 160$ $\mu$m. For a subset of the beam containing only 220 MeV electrons, and assuming a source beam of size 1$\mu$m and divergence 1 mrad, calculations using linear beam optics of the transport system give a spot size of $0.20 \times 0.44$ mm (x-axis $\times$ y-axis) and divergences of just a few $\mu$rad at S1. For these electrons the spot size can be maintained over long distances which is essential for applications involving apertures or which are sensitive to the divergence such as for undulator experiments [Fuchs et al. 2009]. Furthermore, simulations of Gaussian, on-axis beams with a divergence of 1.7 mrad FWHM (as measured in the experiment) show that the imaging system transports all particles with energy in the range measurable with the spectrometer without clipping at the lens apertures.

### 6.1.2. Electron beam focusing

Increasing both the distance of the PMQ lenses to the gas cell, as well as the distance between them by ~5 mm changes the collimation into a focus at the position of S2, 1.94 m behind the accelerator. Figure 6.2(a) depicts the summed signal of 20 consecutive shots detected at S2 without magnetic lenses. For these unfocused beams the average width at 220 MeV of a *single* shot caused by the divergence is 3.2 mm FWHM. The summed signal of multiple shots is much larger due to pointing fluctuations occurring from shot to shot. Figures 6.2(b) and (c) show the focusing effect of the PMQ lenses at 230 and 210 MeV respectively for a sum of consecutive shots. As for the case in figure 6.1 b), the summed beam size is reduced for a broad range of electron energies. The lenses were aligned such that the electrons hit the spectrometer entrance on the laser axis. The fact that the best focusing coincides with the chosen energy (green vertical lines) proves the excellent accuracy in charac-

[i] The divergence of the simulated beam was the Gaussian addition of the pointing fluctuations and the divergence.

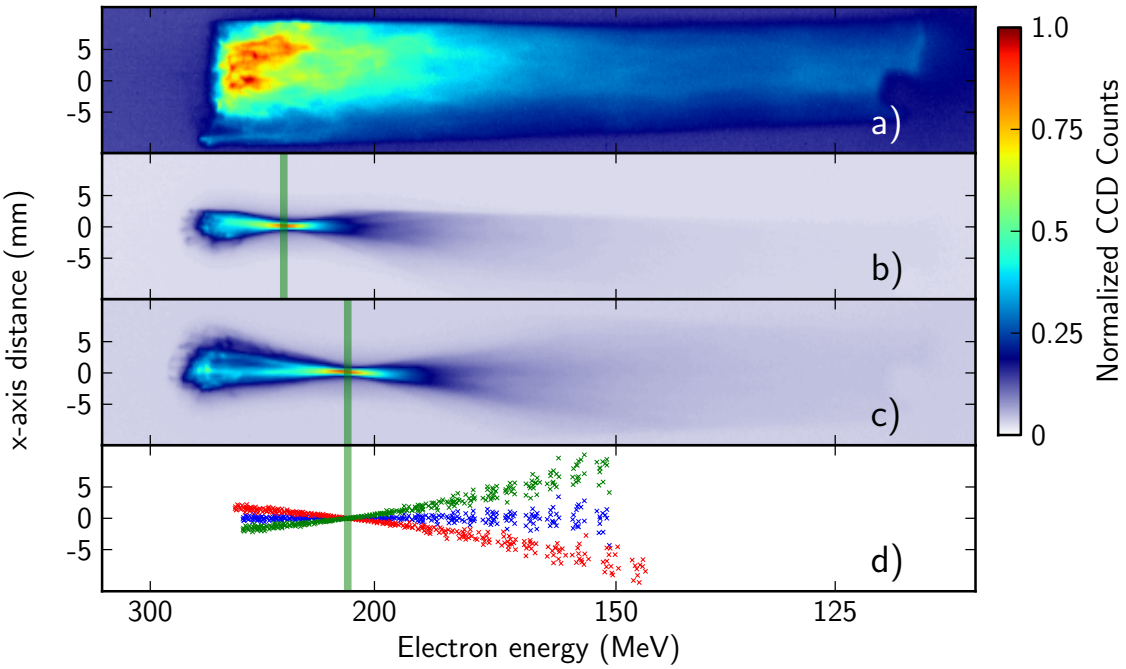


**Figure 6.2. – Electron beam focusing:** False colour images of summed electron beam spectra observed at S2 (experimental sub-figures are each normalised to one). a) Sum of 20 consecutive shots without magnetic lenses. b) Sum of 44 shots, focus at 230 MeV. c) Sum of 30 shots, focus at 210 MeV. Vertical green lines indicate the target electron energy to be focused at the screen position. d) Tracking simulations with lenses positioned as in c) for electron beams with energies 150 - 250 MeV with initial divergence of 1.7 mrad FWHM for three different initial pointing angles ($\theta_{x,y}$) leaving the gas cell: on-axis beam $\theta_{x,y} = 0$ (blue), $\theta_x = \theta_y = 3.6$ mrad (red), $\theta_x = -3.6$ mrad $\theta_y = 0$ (green).

terising, modelling and positioning the lenses to achieve the desired focus. As in the previous section for the beam collimation case, a particle tracking simulation using GPT showed that the bunch is transported without any loss of particles within the measurable energy range of the spectrometer. Individual shots in these configurations have widths $\lesssim$500 $\mu$m FWHM at the focused energy and are limited by the resolution of the detection setup. For high-resolution measurements of the beam focus size see section 6.2. To change the focusing from 210 to 230 MeV required changing the distance from the lenses to the gas cell by 22 mm, and the distance between them by 4 mm. The required drift lengths around the lens doublet depend linearly on the electron energy for a broad range of energies indicating the simplicity and tunability of this method. The chromaticity of the lenses results in the imaging of only a particular electron energy at S2. For off-target energies the beam

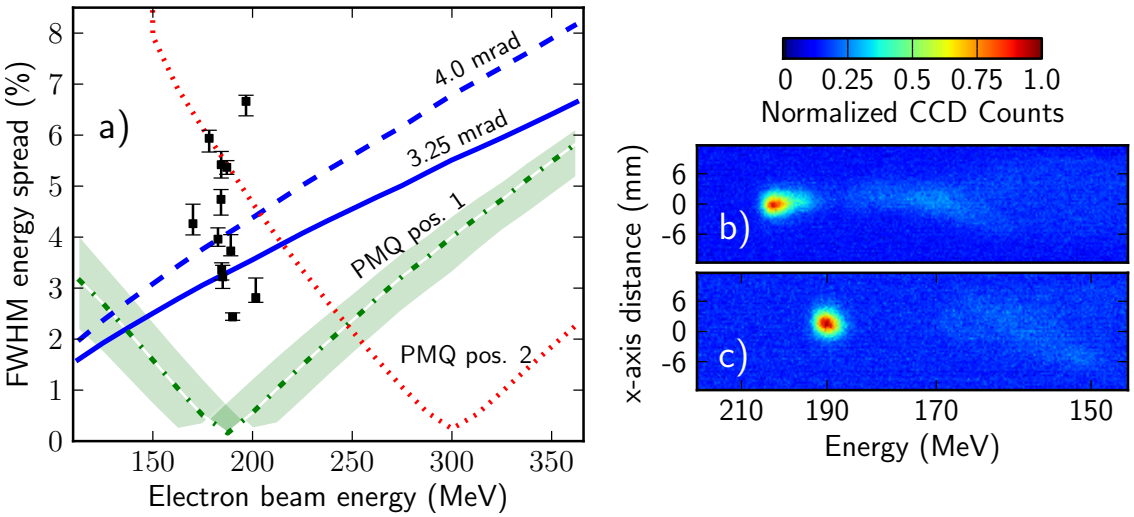


**Figure 6.3. – Energy resolution improvement:** a) A mono-energetic electron beam entering a dipole magnet spectrometer will have its measured energy spread artificially enlarged by its divergence. The spectral resolution is shown for two cases, mono-energetic electron beams with an initial FWHM divergence of 3.25 mrad (solid blue line) and 4.0 mrad (dashed blue line). These errors can be significantly reduced for any energy that can be focused on the observation plane at S2 by the magnetic lenses. The green (dash-dotted) and red (dotted) curves show the calculated measurement accuracy for two different lens positions. The green shaded area shows the effect of longitudinally misaligning the second lens by ±5 mm. Black squares represent measured energy spreads with the lens system focusing 190 MeV (corresponding to the green dash-dotted curve). b) and c) show false colour images of electron spectra observed at S2 for this lens setting with FWHM energy spreads of 2.8% b), and 2.4% c).

divergence and pointing lead to a larger spot size and transverse offset, respectively. For many shots this results in the observed shape of the summed signal which is confirmed by simulations assuming ideal quadrupole lenses with field gradients and positions as in the experiment (see figure 6.2(d)). The measurements suggest the possibility of using PMQ lenses in a spectral filter by placing a suitable mask at the focus position to scatter and therefore substantially increase the emittance of off-target (out of focus) energies. After a subsequent lens system to collimate the desired beam energy, the effective on-axis energy spread will be reduced. This idea was pursued in depth in the work of Lechner [2011].

### 6.1.3. High-resolution imaging spectrometer

The beam transport system can also be used to improve the characterisation of the electron spectrum. In the experiment the energy of an electron beam is measured by observing its deflection behind a dipole magnet. An experimental error can result from the finite position offset and angle at the spectrometer entrance due to the divergence, or for a series of shots, the pointing fluctuations of an electron beam. The divergence in the dispersion plane of the spectrometer causes an increase in the measured energy spread due to the larger spot size observed behind the magnet. The pointing fluctuations cause an error in the measured absolute energy from shot to shot due to the resulting position offset behind the magnet. These experimental errors can be significantly reduced by imaging the electron beam from the accelerator exit to the observation screen. This has been realised with imaging spectrometers specifically designed for LWFA beams [Nakamura et al. 2008; Sears et al. 2010b] which have accuracies of 1% rms or better over a range of several hundred MeV. Alternatively, a non-invasive method is to use an undulator as a diagnostic device by analysing the emitted radiation [Gallacher et al. 2009]. In the present work PMQ lenses were used to image the electron beam and, in combination with a simple dipole magnet, create an imaging spectrometer. To quantify the spectrometer resolution for the imaging and the free-drift cases, particle tracking simulations of mono-energetic beams with a source size of 1 $\mu$m and FWHM source divergence of 4 mrad were performed for a range of energies. Using the dispersion function of the spectrometer, the tracked beam size at S2 was then mapped to an energy spread (figure 6.3 (a))[ii]. The error for the freely drifting beam is shown for two source divergences deduced from data taken during these experiments, 3.25 mrad (blue solid line) and 4.0 mrad (blue dashed line) corresponding to the lowest and median measured electron beam divergences. The measured error becomes more severe at higher energies due to the lower dispersion of the spectrometer. The effect of imaging with PMQ lenses is shown for two different lens positions (green dash-dotted and red dotted curves) improving the resolution of the spectrometer to $\sim$0.2% FWHM for the focused energy. In practice the resolution is likely to be limited by the detector observing the beam behind the dipole magnet, for the experiment in this work this leads to a resolution of $\sim$0.4% FWHM. Figures 6.3(b) and (c) show measured spectra at S2, Fig. 6.3(c) depicts a beam with an energy spread of 2.4% FWHM, or 1.0% rms assuming a Gaussian profile, and containing 0.4 pC of charge. Even a large misalignment of the second lens in position by $\pm$5 mm leads to only a minor decrease of spectral resolution (figure 6.3(a) green shaded area) indicating that the measured energy spread is intrinsic to the electron

[ii] The results presented here are based entirely on simulations to allow the inclusion of quadrupole lenses in the beamline. For an analytical derivation for a freely drifting beam with a divergence and a dipole-magnet spectrometer, see the work of Osterhoff [2008].

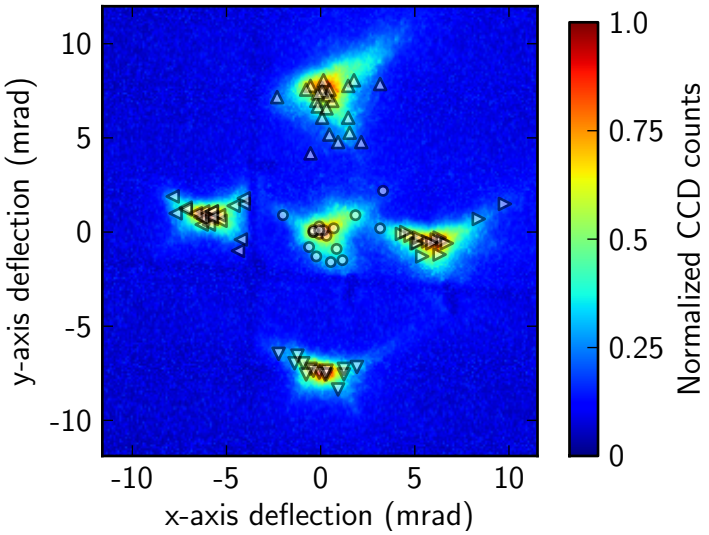


**Figure 6.4. – Electron beam steering:** False colour summed images observed at S1, 1.12 m behind the electron source with symbols marking the peak position of individual shots. The central spot shows the sum of 18 shots (circle symbols). The surrounding four spots (triangle symbols of differing orientation) were observed after offsetting the second lens transversely to the beam propagation direction in four separate positions. This introduces a dipole moment which deflects the electron beam. The lens was moved by $\pm 390$ $\mu$m and $\pm 530$ $\mu$m in the x and y direction and caused corresponding angular deflections of 6.1 and 7.3 mrad in the same direction.

bunch. The positioning error of the first lens is even less critical in this context. The detrimental effect of higher order magnetic multipoles [Becker et al. 2009] (and the resulting increase of both the beam size at S2 and the apparent energy spread) were included in the simulation by tracking the beam through measured field maps of the lenses used in the experiment. Beams with a similarly low energy spread have been demonstrated in experiments using a second counter-propagating laser pulse to control the electron injection precisely [Rechatin et al. 2009]. The generation and reliable diagnosis of low energy spread LWFA electron beams is a fundamental requirement for realising a laser-driven laboratory-scale FEL.

### 6.1.4. Electron beam steering

Besides imaging the electron beam, its propagation direction could be actively steered. By introducing a transverse offset $d$ of the second PMQ lens to the beam propagation axis, the beam experiences a dipole field of magnitude $\sim gd$ when it enters the lens, where $g$ is the lens magnetic field gradient. For a transverse offset in the focusing (defocusing) plane of the lens, the beam will be deflected towards

(away) from the lens centre, and for a thick lens, experience a dipole field of decreasing (increasing) magnitude as it passes through the lens. Hence, the angular deflection is weaker in the focusing than in the defocusing plane for the same lens offset. Figure 6.4 shows steering of the electron beam on screen S1, 1.12 m from the source with four different transverse offsets of the second lens. The introduced horizontal offsets of L2 were $\pm 390$ $\mu$m (defocusing plane), and the vertical offsets were $\pm 530$ $\mu$m (focusing plane). This resulted in average angular deflections of 6.1 mrad and 7.3 mrad in the same directions which gives a larger deflection per offset in the defocusing plane as expected. The drawback of this method is the possible distortion of the beam shape. Both the introduced dipole strength and the magnitude of higher order aberrations grow with the offset $d$. The perturbing effect of the higher order aberrations increases with the beam size in the lens. The introduced dipole field disperses the beam due to its energy spread and hence also increases the spot size. Depending on the subsequent requirements on the electron beam, these effects need to be taken into account. Steering the beam using quadrupole lenses is a simple and compact method to counteract an undesirable angular offset of the electron beam that can be caused by a tilted intensity pulse front of the driver laser [Popp et al. 2010].

## 6.2. Electron beam emittance

In this section the measurements used to obtain an electron beam emittance will be shown and discussed. The results of the analysis give the transverse emittance, the electron energy, the source size, and the source divergence; the latter two refer to the values of a "virtual" electron beam source at the accelerator exit[iii]. The divergence corresponds to the free drift divergence of the beam as it would be measured by a beam profile monitor after a drift behind the capillary. The source size is a helpful concept to quantify the size of the electron beam at the accelerator exit, but may not correspond to a real beam waist. The reason for this potential discrepancy is the lack of empirical data concerning the effect of the plasma to vacuum transition (for more details, see section 6.2.7). The electron energy obtained from the data analysis can be compared to that from the position of the measurement apparatus and the spectrometer calibration. The results presented in this section were published in Weingartner et al. [2012] and are summarised in table 6.1.

[iii] In the text the word "size" is sometimes omitted leaving just 'source' and 'divergence' to refer to the virtual source parameters.

**Table 6.1.** – Results from the lens position (multi-shot) and energy scan (single-shot, mean over several shots) methods

| **Energy (MeV)** | $\varepsilon_n(\pi.\mu m.rad)$ | $\sigma(\mu m)$ | $\theta(mrad)$ |
|---|---|---|---|
| **300** | | | |
| E scan | $0.22^{+0.02}_{-0.02}$ | 0.91 | 0.40 |
| D2 scan | $0.19^{+0.03}_{-0.01}$ | 0.91 | 0.35 |
| **270** | | | |
| E scan | $0.19^{+0.02}_{-0.02}$ | 0.88 | 0.40 |
| D2 scan | $0.17^{+0.02}_{-0.01}$ | 0.92 | 0.34 |
| **245** | | | |
| E scan | $0.21^{+0.03}_{-0.03}$ | 0.95 | 0.44 |
| D2 scan | $0.20^{+0.01}_{-0.02}$ | 0.93 | 0.44 |

### 6.2.1. Energy dependence

Derived source size and divergence
Divergence dependence on electron energy

This section shows experimental results of the lens-scan method which was described in section 3.4.1. The method measures the electron beam size at the YAG:Ce crystal for a range of lens positions. The electron beam parameters can be fitted to this data which was done for beams with energies of 245, 270, and 300 MeV at a plasma density of $6 \times 10^{18}\mathrm{cm}^{-3}$. The retrieved source divergence will be compared with the measured free-drift value, and also the effect of space-charge on the measurement will be discussed.

Figure 6.5 shows a scan of the z-position of lens two and the resulting measured beam size at the YAG:Ce crystal positioned behind the dipole magnet such that electrons with an energy of 245 MeV are observed. Each data point is the mean rms beam width of 15 or more shots; the width of each shot is evaluated for a small integrated energy bandwidth (±0.05 MeV) around the observed energy. The error bars correspond to a 95% confidence interval for the mean. The parameter fit gives a source size of 0.93±0.11 µm and source divergence of 0.44±0.04 mrad, resulting in a normalised emittance of $0.20^{+0.01}_{-0.02}$ $\pi$·mm·mrad. The error limits are 95% confidence intervals obtained by bootstrapping procedure using 2000 samples (see Appendix A). The accuracy of the method is also illustrated by the expected dependence for a 20% larger emittance by increasing the inferred source size or divergence.

This measurement was repeated for electron energies of 270 and 300 MeV. For

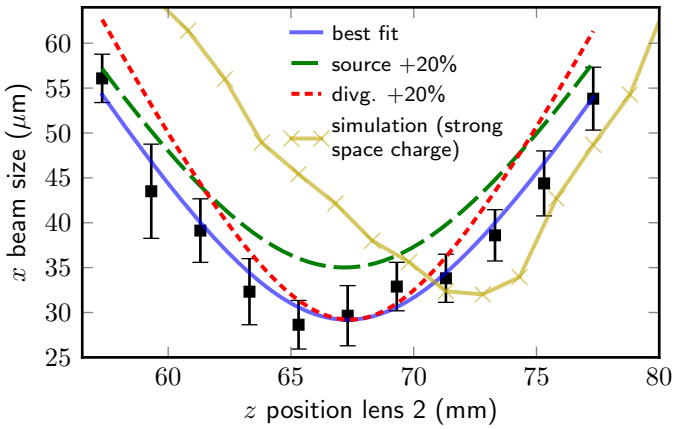


**Figure 6.5. – Lens position scan for 245 MeV electrons.** The black squares show the mean RMS beam sizes for various $z$-positions of lens two. The error bars correspond to a 95% confidence interval for the mean value. The fit curve (blue) neglects space charge and gives a normalised emittance of $0.20^{+0.01}_{-0.02}$ $\pi$·mm·mrad and inferred RMS source size and divergence of $0.93\,\mu\mathrm{m}$ and 0.44 mrad, respectively. The influence of space charge is shown by the yellow line which shows the expected beam sizes for a high space-charge beam. The discrepancy in shape and position along the horizontal scale of the yellow and blue lines indicate that space charge is negligible. The initial source size and divergence in the space-charge simulation were chosen to be $0.25\,\mu\mathrm{m}$ and 0.45 mrad respectively to obtain a similar curve as obtained from the measurements.

270 MeV electrons the fit routine gives a source size of $0.92^{+0.07}_{-0.11}\mu$m and source divergence of $0.34^{+0.08}_{-0.04}$ mrad, resulting in a normalised emittance of $0.17^{+0.02}_{-0.01}$ $\pi$·mm·mrad. Similarly for 300 MeV electrons the fitted source size is $0.91\pm0.07\mu$m and the source divergence is $0.35^{+0.09}_{-0.06}$ mrad, resulting in a normalised emittance of $0.19^{+0.03}_{-0.01}$ $\pi$·mm·mrad. As above, the error bars represent 95% confidence intervals. The normalised emittance remains relatively constant which supports the expected linear focusing forces in the wakefield during acceleration as discussed in section 2.5, and which has been previously observed at lower electron energies of $<$20 MeV [Sears et al. 2010a]. To make a more conclusive claim about a constant normalised emittance would require a larger range of energies to be measured. One reason is that the margin of error of $\sim 10\%$ in the calculated emittance is comparable to the energy range that is scanned here.

The derived divergences are compared with the free-drift divergences measured behind the spectrometer with a lanex screen in figure 6.6. Below about 250 MeV the lanex and the lens-scan divergences agree well. For higher energies the larger diver-

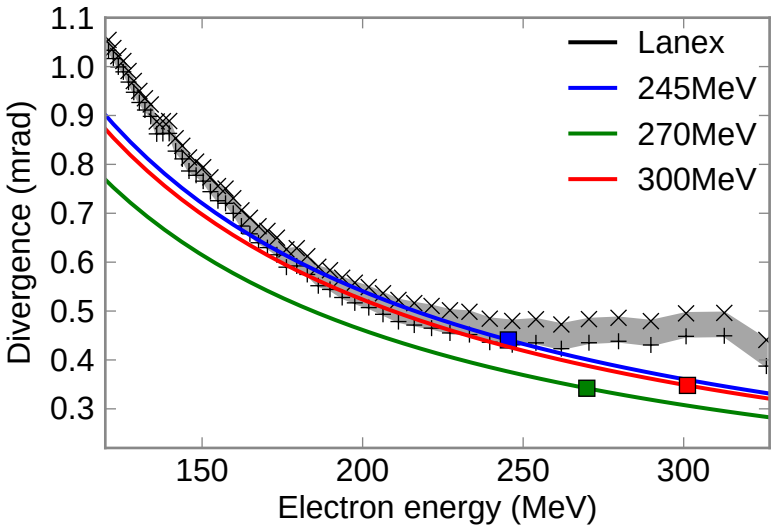


**Figure 6.6. – Comparison of divergence measurements.** The plot shows the measured electron beam divergence using the lens scan method (squares). The measured divergences are extrapolated for other energies by assuming the source divergence scales as $\theta(\gamma)/\gamma = \theta(\gamma_0)/\gamma_0$ as would be expected from an electron beam source undergoing adiabatic damping during acceleration (solid blue, green, and red lines). The measured divergence with the lanex screen at S2 are shown in black (crosses: raw data, pluses: raw data deconvoluted with a $\sigma = 400\mu\text{m}$ Gaussian to account for the resolution of the lanex measurement).

gences often seen around the spectral peak of individual shots lead to a flattening of the average divergence of many shots as observed by the lanex screen (see figure 5.5). As the spectral peak is at a different energy from shot to shot, the lanex divergence flattens out for $> 250$ MeV. During the lens-scan measurements the spectral peaks of the electron bunches were well beyond 300 MeV being observed by the YAG:Ce crystal, and hence the larger divergence did not influence the measured divergence. There is therefore no discrepancy between the lanex divergence and the lens-scan divergence.

As touched upon in section 3.3.3, the space-charge of the beam affects the beam dynamics during propagation and the position and shape of the lens-scan measurements. As a simple test a beam without space-charge was tracked [GPT] for the different lens positions as in the experiment. The simulated "lens scan" without space charge perfectly matches the "best fit" line in figure 6.5 which is a strong indication that space charge is not relevant in the data over many shots as in this scan. To illustrate how a lens scan would look for a high-charge case, a tracking simulation of 3000 macro-particles including point-to-point space charge for an ini-

tially mono-energetic 245 MeV, 50 pC beam with duration 4.5 fs was carried out (see figure 6.5). The figure shows a clear deviation from the measurements in terms of shape and position. To focus a beam including space charge requires a stronger focusing lens system to compensate the repulsion of the electrons. In the present work stronger focusing is achieved by increasing the $z$-position of lens two, resulting in the shift of the beam size curve to the right as seen in the figure. Such a shift could also be caused by the source position being further away from the first lens (source position upstream of the physical exit of the gas cell, inside the gas cell). A source position inside the gas cell seems unlikely as the depletion length of the laser and gas cell under similar conditions was measured to be $\sim$ 7mm in the experiments described in Popp [2011]. Hence the electron beam is still contained within the wakefield forces for the entire length of the gas cell which was 5 mm for these experiments. Furthermore, as is discussed in section 6.2.7, the plasma-to-vacuum transition rather leads to a shift of the source position *closer* to the first lens (source position downstream of the physical exit of the gas cell, outside of the gas cell). Despite these arguments, as the electron source position is not precisely known, the position of the measured curve of a lens scan is not conclusive about the strength of the space charge affecting the beam. A stronger indicator seems to be the shape of the measured curve. Anderson and Rosenzweig [2002] showed that quadrupole scans of beams with significant space charge display an asymmetry about their minimum, with the stronger focusing side (larger lens two $z$-position) showing a steeper flank. As the measured data does not show a significant asymmetry (or shift), space charge effects must be much less significant in the experiment than in the simulation in the figure. As the charge is reduced in the simulation, the yellow curve moves towards the measured data, becomes symmetric, and eventually matches the blue fit curve. The measurement accuracy benefits from the spectral splitting of the beam behind the dipole magnet which reduces the charge density and hence the space charge repulsion of the beam. The measured data therefore confirms that space charge is negligible in the present experiment.

### 6.2.2. Single-shot emittance measurement

In the previous section a lens was moved and the resulting changes in beam size were used to fit an emittance. This method requires multiple shots to cover a range of lens positions for the fit routine. Alternatively to changing a lens position, a range of electron energies can be observed and an emittance fitted to the resulting beam sizes as a function of energy (see discussion in section 3.4.2). In this case the disadvantage of large energy spreads from the LWFA process can be put to good use as a single shot easily delivers a large enough energy range to fit an emittance. At 300 MeV, the dispersion of the electron spectrometer is such that the YAG:Ce crystal with diameter $\phi = 10$ mm can observe a range of electron energies of slightly

more than 4 MeV. This energy range is large enough to fit an emittance with good accuracy.

Figures 6.7(a) and 6.7(b) show the fitted curve to the raw data for two shots at different energies. Due to the larger dispersion of the dipole magnet spectrometer at 245 MeV, the energy range on the YAG:Ce crystal is only 2.5 MeV at this energy. For the 300 MeV shot the fitted source size and source divergence are 0.628±0.005µm and 0.383±0.013 mrad, resulting in a normalised emittance of 0.143±0.004 $\pi$·mm·mrad. The error bars for all numbers in this paragraph represent a 95% confidence interval based on a bootstrap analysis (for a description and comparison to other error bars see below). This shot has a particularly low emittance which can be seen in the context of some shots around it. For the 44 shots taken with similar conditions the average observed emittance value is 0.22±0.02 $\pi$·mm·mrad. The 245 MeV shot is also a low-emittance shot with a derived value of 0.12±0.01 $\pi$·mm·mrad, the 48 shots taken around it have an average of 0.21±0.03 $\pi$·mm·mrad. The average values at both energies agree well with the values obtained from the multi-shot methods described earlier in this section.

As the analysis for the energy-scan method relies on fitting to electron beam sizes of different energy, it is more robust in the 300 MeV than for the 245 MeV case. This becomes clear when looking at the hypothetical fit curves for increased electron beam source parameters. The source size and source divergence which best fit to the data are increased by 20% and the expected beam size at the YAG:Ce crystal is calculated. From these curves it becomes clear that the source size mainly influences the "height" of the fit curve[iv], and the divergence the "steepness" of the curve flank (see figure 3.13). In figure 6.7(b) it is clear that the source size is well distinguishable from the 20% larger source case but the same can not be said for the divergence. A bootstrap analysis [v] of the 245 MeV shot shows the 95% confidence interval for the divergence is $0.387 \pm 0.035$mrad, an error of approximately 9% which leads to a similar accuracy for the emittance. The confidence interval for the divergence of the 300 MeV shot is $0.383 \pm 0.011$mrad, an error below 3%. For this experiment the >4 MeV energy window at 300 MeV is therefore a sensible minimum energy range to obtain an accurate fit for the divergence and therefore the emittance.

Aside from a bootstrap analysis, the error or accuracy of the fit to individual YAG:Ce crystal shots can be estimated by varying relevant experimental parameters (within a reasonable error range) and checking if a fit for the data can still be found. This method is difficult to quantify as it requires subjective choices for what are "reasonable" errors for the experimental parameters. However, it is a useful analysis to get a feeling for which parameters are particularly important to keep small for

[iv] As the system is approximately imaging the electron beam source, a 20% increase in source size results in a ∼20% increase in measured beam size at the YAG:Ce crystal.

[v] 2000 resampled residuals, see appendix A.

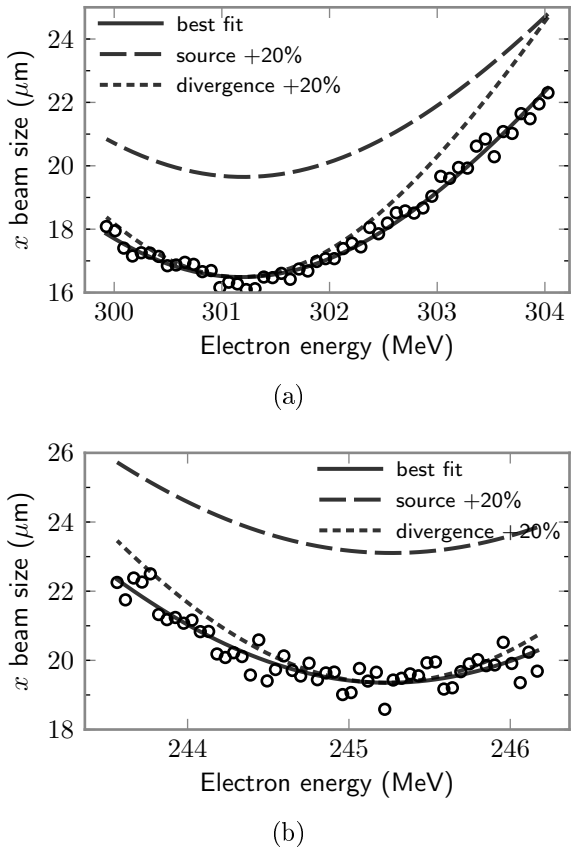


**Figure 6.7. – Electron beam size of two shots at the YAG:Ce crystal.** The smaller spectrometer dispersion at higher energies means a larger energy range can be seen on the YAG:Ce crystal at 300 MeV (a) than around 245 MeV (b).

an accurate measurement. The experimental errors for the derived emittance of the 300 MeV shot shown in figure 6.7(a), lead to bounds of $\pm 0.03$ $\pi$·mm·mrad, an order of magnitude larger than the bootstrap bounds obtained above. The experimental parameters that were varied to find these bounds where the drifts between the gas cell and lens 1 ($d_1$), the drift between the lenses ($d_2$), and the drift from lens 2 to the YAG:Ce crystal ($d_3$). The fit parameters were the source size and divergence, and the electron beam energy. The drift $d_2$ ($\sim$10 cm) is best determined as is it was measured with calipers. Even with a generous measurement error for $d_2$ of $\pm 3$ mm, the fitted emittance varies by only 1%. For $d_1$ the situation is more complex: on top of the physical measurement error as for $d_2$, there is the additional uncertainty of where exactly the source of the electron beam is. As discussed in section 2.6, the electron beam source may not be at the physical exit of the gas cell due to the gas density downramp. Such a source position shift has not been measured explicitly

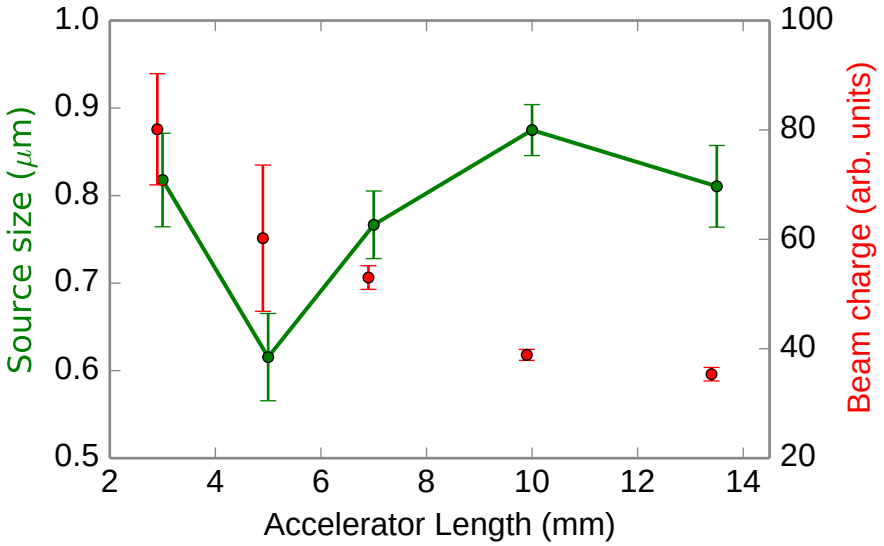


**Figure 6.8. – Accelerator length scan.** The plasma density was constant at $5.5 \times 10^{18}\mathrm{cm}^{-3}$. Each data point is the mean value of at least 36 shots (except at 5 mm, here the mean of 8 shots). The error bars show the 95% confidence interval for the mean. The charge data points are slightly offset in the horizontal axis to be distinguishable from the derived source size data. The increase of source size with acceleration length can be explained by heating of the electron beam due to its interaction with the tail of the laser during acceleration. The decrease in charge with acceleration length could be due to the higher charge observed near the high-energy cutoff (see the main text); for shorter accelerator lengths, the observed electrons 232 MeV are closer to the cut-off energy.

but simulations indicate shifts of several mm are possible. The upper and lower bounds of $\pm 0.03$ $\pi$·mm·mrad for the derived emittance given above are a worst-case consideration and arise from a combined error for $d_1$ and $d_3$. A shift of the electron beam source position of $\Delta d_1 = \pm 10$ mm and a measurement error for the drift to the YAG:Ce crystal $\Delta d_3 = \pm 50$ mm, results in this largest possible error.

The fit parameter values of this section are summarised in table 6.1 on page 102.

### 6.2.3. Acceleration length dependence

Figure 6.8 shows the effect of accelerator length on the derived source size and the measured charge for 232 MeV electrons generated with a plasma density of $5.5 \times 10^{18}\mathrm{cm}^{-3}$. The measured source size is in general around 0.8 µm, with a decreased size for an 5 mm acceleration length. First of all, the variation in source size

with acceleration length measured here is not contrary to the relatively constant source size measured for 245, 270, and 300 MeV electrons in section 6.2.1. The approximate difference in acceleration length given the average gradient of 79 MV/mm (see section 5.1) is $\sim$ 700µm, a small fraction of the length variation plotted in figure 6.8. Hence the two results, constant source size for small energy range, various source size for accelerator length range, are not contradictory. This data cannot confirm that the transverse focusing fields within the plasma are linear (and hence emittance preserving) for the presented range of accelerator lengths. Although the data is certainly not conclusive, at least a hypothesis can be made for the increased source size either side of an accelerator length of 5 mm. After an acceleration length of only 3 mm, the examined energy of 232 MeV is near the energy peak of the earliest injected electrons. It is plausible (and also worth further investigating) that the first batch of electrons that is injected into the wakefield does so with a higher transverse distribution. For accelerator lengths larger than 5 mm, a possible interaction of dephased electrons with the laser is further discussed below.

In Popp [2011], a length scan with a similar plasma density as used here revealed a dephasing length of $\sim$ 5 mm for the cut-off energy of 380 MeV (see also section 5.1). Furthermore, a fit to the cutoff energy revealed an accelerating gradient of 34 MV/mm$^2$. From these fit parameters the required acceleration distance to achieve 232 MeV electrons can be calculated, giving a distance of $\sim$ 2mm after injection. After an acceleration length of $\gtrsim$ 7.9mm, 232 MeV electrons could also be "dephased electrons"; electrons which have previously obtained a higher energy but have decelerated back down to 232 MeV after passing into the decelerating phase of the wake wave (see figure 2.4)[vi]. Dephased electrons have therefore passed into the front half of the potential bucket and into a region where the laser intensity can become significant. In Mangles et al. [2006] it was observed that the interaction of electrons with the laser pulse leads to an increase in the beam emittance due to the transverse ponderomotive force. If additionally to this the condition $c\tau > \lambda_p/2$ is fulfilled (the laser extends to the middle of the plasma wakefield), beam heating and hence a larger electron beam size is expected. For the density of this run ($5.5 \times 10^{18}$cm$^{-3}$), and for the 23 fs laser pulse this condition is met. The increase in measured source size from $\sim$ 7mm could therefore come from laser-beam heating. However as the laser is expected to have depleted at around 7 mm acceleration length, an alternative reason for the increased beam size could be the transition from a laser-driven to the beam-driven regime.

The charge shows a steady decline with acceleration length. This result agrees with the spectra shown in figure 5.2. These spectra show a relatively constant charge

[vi] The fit parameters were obtained for a density scan at $6.5 \times 10^{18}$cm$^{-3}$ as opposed to $5.5 \times 10^{18}$cm$^{-3}$ used in the length scan in this work. As the dephasing length scales inversely with density (see equation 2.29), the lower density as used here leads to a longer dephasing length than the 5 mm taken from Popp [2011].

distribution with energy, along with a high-charge peak at the high-energy end of the beam spectrum. In Osterhoff [2008], this charge distribution was also observed for a fixed-length 15 mm long gas cell and explained with phase space compression occurring around the dephasing point: as electrons pass the dephasing point, they begin to lose energy whereas lower-energy electrons still accelerate. An alternative explanation can be given based on a variable-length gas cell as mentioned in the previous paragraph (Popp [2011]). Here a peaked density is observed even for accelerator lengths *shorter* than the dephasing length. This implies that the injection process itself is different for the high-energy electrons which are first injected than for those electrons injected later on. A clear difference is that the later-injected electrons are affected by the already-trapped electrons (see "beam-loading" in section 2.4). The data shown in figure 6.8 can be interpreted such that beam loading leads to steadily less injection (and hence less measured charge), and could also be the cause for the decrease of the measured source size before dephasing. A possible explanation could be a reduced "acceptance" of off-axis injection due to the modified wakefields due to beam-loading. In effect the already-injected electrons could lead to preferred injection of on-axis electrons leading to a lower source size. The experimental data shown here is not extensive enough to validate this hypothesis, more investigation is necessary at short acceleration lengths.

The measurements shown here were made for 232 MeV electrons. At this energy the spectral dispersion of the electrons results in a range of only 2 MeV being observed at the YAG:Ce crystal for a single shot. As discussed in section 6.2.2, for such a small range of energies the difference in beam sizes does not allow to obtain a reliable measure of the source divergence, hence it is left out in this discussion and in figure 6.8. It would be interesting to repeat this measurement at an energy which permits an accurate measurement of the divergence. As discussed in section 2.6, the beam envelope equations are only valid for an ion channel (such as behind the laser pulse in the blow-out regime). As the laser energy is depleted after approximately 7 mm at the electron density used here, the divergence damping during the transition to vacuum could be considerably reduced for longer accelerator lengths. This would be observable by an increase of the derived source divergence.

### 6.2.4. Plasma density dependence

A central parameter for LWFA is the plasma density. In chapter 2 the role the plasma density plays on the plasma wavelength and theoretical models of the injection and trapping of electrons were discussed. It is therefore interesting to ask the question how the plasma density affects the electron beam emittance. In figure 6.9 the measured charge, derived source size, divergence, and emittance are shown for a range of plasma densities. The data was taken for a constant gas cell length of 5 mm.

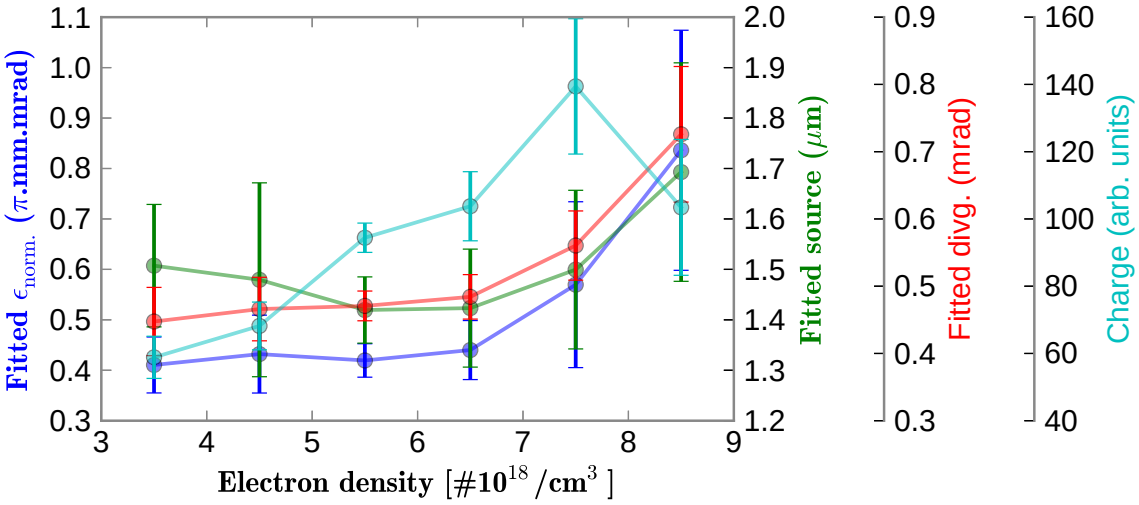


**Figure 6.9. – Plasma density scan.** The accelerator length was 5 mm, the measured energy 310 MeV. The data points are the mean values of 10 shots and the error bars show the 95% confidence interval for the mean. Above a density of $\sim 7 \times 10^{18}\text{cm}^{-3}$ the laser and the electron bunch interact leading to an increase in the electron beam phase space.

In the previous section the accelerator length scan showed signs of electron beam heating by the laser pulse for lengths >5 mm with a plasma density of $5.5 \times 10^{18}\text{cm}^{-3}$. As the density increases, the plasma wavelength decreases and the laser pulse occupies a larger fraction of the plasma bubble. In Mangles et al. [2006] the onset of electron beam heating by the laser pulse was extrapolated to be at $c\tau \sim \lambda_p/2$. For the laser used in this experiment with a FWHM pulse duration of 23 fs, a density of approximately $7 \times 10^{18}\text{cm}^{-3}$ (with a corresponding non-linear plasma wavelength of $\lambda_p \sim 14\,\mu\text{m}$) fulfils this condition. The source size as well as the divergence plotted in figure 6.9 show an increase at or slightly below this density and thus agrees with Mangles et al. [2006]. The results in Mangles et al. [2006] were obtained for the entire electron beam spectrum, for a different laser pulse, and different plasma density. As the experimental setup here provides a method to determine the source size spectrally resolved, it would be interesting to make a follow-up measurement of when the source size increases with plasma density while scanning the observed electron energy. Presumably higher energies would be heated at a lower density as they are further forward in the wakefield. Such emittance heating is detrimental for applications dependent on the small-emittance beams which the LWFA can principally provide. Careful thought has to go into choosing the optimal acceleration length to obtain high enough energies yet avoid heating of the electron beam by the laser.

The accelerated charge is shown to generally increase with density as expected from the decreased trapping threshold due to the slower phase velocity of the plasma wave (as discussed in section 2.4). For the measured density above $7.5 \times 10^{18}\text{cm}^{-3}$ the charge drops quite significantly. A similar rise and fall of accelerated charge was observed previously by Osterhoff [2008]: the increasing charge flank is explained by a "more efficient wave-breaking with higher density" which leads to an "enhanced injection probability" (see also the discussion in section 2.4 and figure 2.3). For the drop in charge a number of effects such as electron dephasing (reducing the total observed charge due to a lower cut-off energy), a reduction of the beamloading threshold for higher density (less charge can be injected before beamloading occurs), and the growing deviation from the resonant plasma wave driving condition (less efficient plasma wave generation) are discussed.

### 6.2.5. Computer (PIC) simulation of electron injection

The results of the last two sections will be compared with simulations here. Computer simulations based on the **PIC (particle-in-cell)** method are currently the standard tool to simulate LWFA experiments. PIC codes track the relativistic motion of macro-particles and solve Maxwell's equations on a grid at each time step. As PIC simulations make few physical assumptions, they can be very successful in describing experimental results in terms of accelerated charge and energy [Tsung et al. 2006]. In contrast, Popp [2011] has seen a large discrepancy between simulation and experiment in terms of charge and questions the accuracy of the injection process due to the limited resolution of the simulated grid as compared to the small injected beam sizes[vii]. Cowan et al. [2012] also notes that in a standard PIC implementation, electro-magnetic waves travelling along the axis experience a numerical dispersion error. Quoting from this reference: "*This artificial slowdown of the driver and the bubble leads to incorrect dephasing of accelerated electrons and also permits synchronisation of sheath electrons with the bubble, leading to their unphysical injection*".

The results in this thesis showed that the electron beam source size varied with both the plasma density and the acceleration length. As the shortest experimental acceleration length was 3 mm, it is interesting to use computer simulations to investigate the effect of the plasma density on the injection and early stages of acceleration. Two simulations were performed using the PIC code OSIRIS ([Fonseca et al. 2002]), with a plasma density of 100 and 150 mbar ($5 \times 10^{18}\text{cm}^{-3}$ and $7.5 \times 10^{18}\text{cm}^{-3}$ respectively) and a laser as in the experiment (see figure 6.10). It can be seen that the larger pressure results in an earlier injection point as well as a larger injection cross-section. The earlier injection can be explained by stronger

[vii] In the simulation shown in figure 6.10 a transverse grid resolution ~0.2µm was used. The injected beam size is of the same order as can be seen in figure 6.10(b)

self-focusing of the laser beam in a higher plasma density, resulting in the laser intensity to reach the wavebreaking threshold at an earlier point. The larger injected beam size seems plausible considering the discussion around figure 2.3; a higher density lowers the trapping momentum threshold, making trapping of off-axis electrons easier and increasing the injected beam size.

The injected beam size is clearly larger in the laser polarisation direction, $x_3$. A larger beam size in the laser polarisation axis has been observed experimentally by Mangles et al. [2006], however there it is attributed to heating of the dephased electron beam by direct interaction with the laser pulse in the bubble. PIC simulations discussed in Cowan et al. [2012] also show an asymmetry in the transverse bubble shape which would support the observed asymmetry in the injected beam sizes shown in the simulation here.

An interesting perspective is recent progress in PIC simulations with enhanced algorithms which could be used to further investigate the results shown here. In particular, Lehe et al. [2013] has implemented a method to reduce numerical Cherenkov radiation which has led to a significant reduction in emittance growth during acceleration in the plasma. The simulation shown in this thesis displayed a doubling of the injected beam size in just over 1 mm of acceleration (outside of the data shown in figure 6.10), which does not agree with the experimental result found in the previous section that the source size increases mildly with the acceleration length (figure 6.8). Cowan et al. [2013] describes a "perfect dispersion" implementation of the PIC algorithm which avoids the unphysical injection quoted above from Cowan et al. [2012].

### 6.2.6. Laser and electron beam pointing correlation

Due to slight pointing fluctuations of the laser beam, the laser focal spot position at the gas cell also fluctuates. Figure 6.11 shows a schematic of the setup used to measure the correlation between these fluctuations in the laser focus position and the electron beam position measured at the YAG:Ce crystal.

For a gas-cell target as used in these experiments, there is no guiding of the laser beam. Hence the electron beam source position at the exit of the gas cell ($x_1$) and the other image sizes ($x_{1-4}$) are given by:

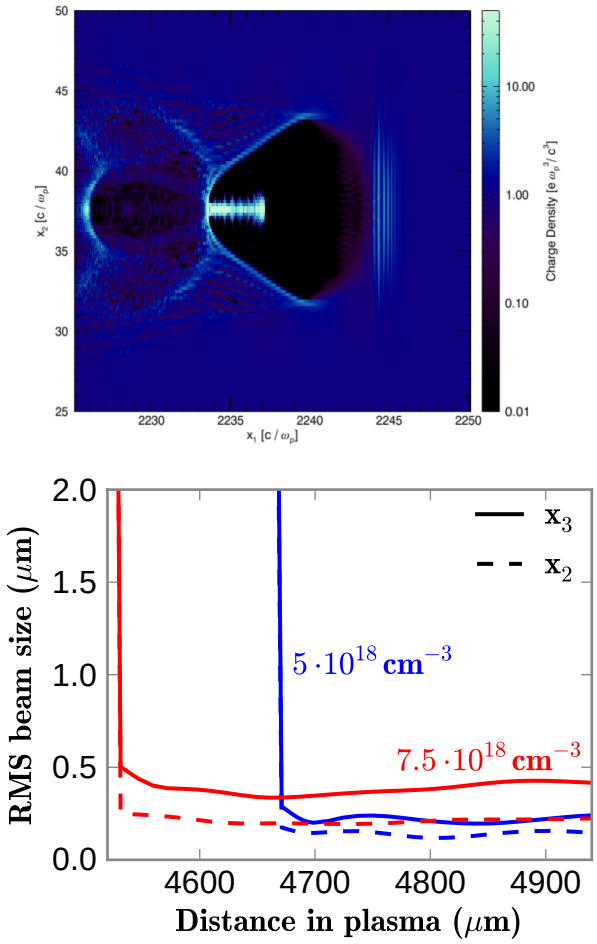


**Figure 6.10. – Computer simulation of LWFA.**
Left: a snapshot of the PIC simulation with a plasma density of $5 \times 10^{18}\mathrm{cm}^{-3}$ showing the plasma bubble trailing the laser pulse and injected electrons. Both axes are spatial scales, the horizontal axis ($x_1$) is along the propagation axis of the laser pulse, the vertical axis ($x_2$) is transverse to it. The laser pulse was linearly polarised in the direction of $x_3$.
Right: the electron beam size around the injection point for injected particles for two different plasma densities. Simulation data courtesy of T. Mehrling.

$$
\begin{aligned}
x_1 &= \theta \cdot f_{\text{parab.}} \\
x_2 &= M_{\text{quads}} \cdot x_1 \\
x_3 &= \theta \cdot f_{\text{lens}} \\
x_4 &= M_{\mu\text{obj.}} \cdot x_3.
\end{aligned}
\tag{6.1}
$$

Here $f$ refers to the focal lengths of the optical lenses and $M$ to the magnification of the respective imaging optics. The following parameters apply to the experiment: $M_{\mu\text{obj.}} = 20, f_{\text{lens}} = 0.5\text{m}, M_{\text{quads}} = 30, f_{\text{parab.}} = 1.5\text{m}$. For this setup the expected correlation between the measured quantities $x_2$ and $x_4$ turns out to be $x_2/x_4 = 4.5$ [viii]. This correlation fits well to the measured data shown in 6.12.

For a gas target with an electrical discharge or a capillary waveguide, the laser beam undergoes guiding during propagation. Therefore the correlation measured here would not exist as the electron beam axis is usually aligned with the laser axis *in the plasma*. Particularly interesting is the possibility to use this method as a diagnostic for offsets between the laser axis and the electron beam axis. Such an offset is observed when the driving laser beam has an intensity pulse-front tilt [Popp et al. 2010]. Due to the image magnification of the electron beam source with the quadrupole lenses, the measurement of an offset angle between the laser and the electron axis as small as 70$\mu$rad is feasible[ix]. This could be used to fine-adjust the compressor grating angles in the laser beamline to optimise the laser-intensity in focus.

As mentioned in section 4.2, the vertical plane was chosen to have the smaller image magnification. A reason for this choice was to reduce the effect of vertical source position fluctuations on the electron energy that arrives at a fixed position at the YAG:Ce crystal. From figure 6.12, it is evident that the laser spot fluctuates vertically within 50 µm. The vertical magnification is about 6, leading to vertical

[viii] The laser angle does not directly enter into the correlation. However it was assumed that this angle is small enough to allow the use of the paraxial approximation for the imaging along the beamline. By calculating $\theta$ using the equations 6.1 and the data in figure 6.12, $\theta$ is typically under $\pm 10\mu$rad, which is consistent with a previous description of the laser system [Osterhoff 2008]. The paraxial approximation is justified in this case.

[ix] A rough calculation: measurement resolution of an offset at the YAG:Ce crystal: 10 µm, electron beam source magnification: 30x. This allows the measurement of a 300 nm offset at the exit of the gas cell which is 5 mm long for the present experiment. This corresponds to an angle of 70$\mu$rad

image offsets of at most 300 µm. The dispersion at the YAG:Ce crystal is about 1.7 MeV/mm when it is positioned to observe 300 MeV electrons, meaning that the image offset leads to a energy offset of 0.5 MeV. From figure 6.7 it can be seen that such an energy offset leads to a negligible increase of the measured beam size around the focused energy. If the large image magnification (factor 30) had been used in the vertical plane, then the energy offsets would fluctuate within 2.5 MeV which would make the vertical source position offsets a relevant error in the measured beam size.

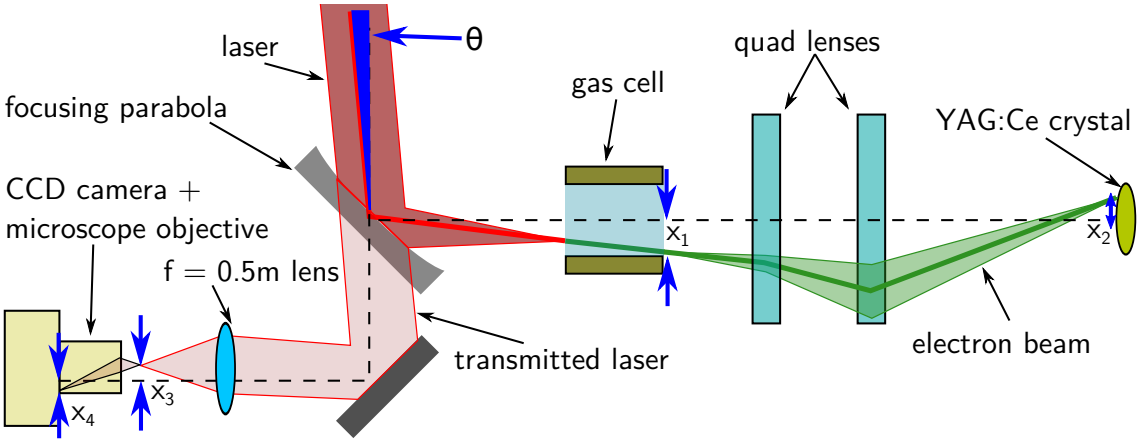


**Figure 6.11. – Setup for measurement of laser beam and electron beam pointing correlation (not to scale).** Relevant quantities for the correlation measurement are marked: $x_{1-4}$: image sizes of the laser/electron-beam along the beamline, $\theta$: pointing angle offset of the laser beam relative to the beamline axis.

### 6.2.7. Effect of density downramp on electron beam

Divergence damping
Virtual source position shift and effect on retrieved emittance

As the presented emittance measurement method measures the beam *after* it has exited the plasma, it is not suitable to quantify changes of the beam size while it is still in the plasma. The expected scaling of the matched beam size with the plasma density $x_m \sim n_e^{-1/4}$ can thus not be validated[x]. However, the discrepancy between the inferred source size from the emittance measurements above (∼1 µm) and the matched beam size in the plasma (∼0.2 µm) can be resolved by considering

[x] The matched beam size can be obtained by setting $x'$ and $x'' = 0$ in the beam envelope equation for an ion channel as given in equation 2.30.

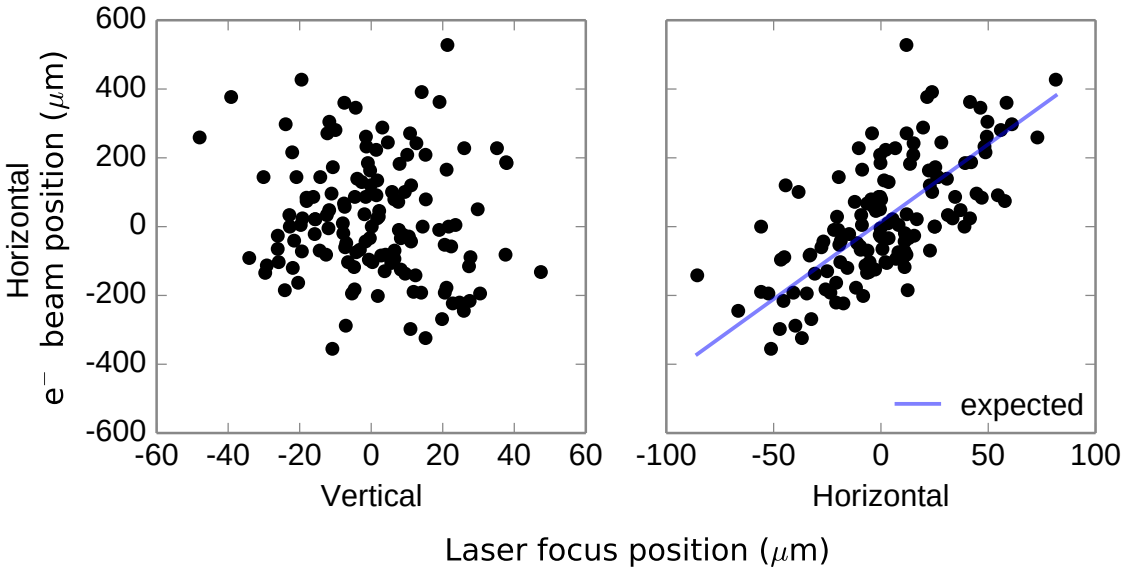


**Figure 6.12. – Correlation between laser beam pointing and electron beam source position.** The expected correlation between $x_2$ and $x_4$ is shown by the blue line (right-hand plot). As expected, there is no correlation between the vertical laser position and the horizontal position of the imaged electron beam (left-hand plot).

the density transition from the plasma to the vacuum. If the electron beam passes through a density downramp comparable to or longer than its betatron wavelength, the decreasing transverse focusing forces lead to an increase of the matched spot size and (due to the conserved emittance) to a decrease of the divergence [Sears et al. 2010a]. This effect was investigated by solving equation 2.30 for a density downramp obtained from computational fluid dynamics (CFD) simulations [openFOAM, computational fluid dynamics code.] modelling the experiment (gas cell with a 1 mm exit hole diameter). The beam divergence obtained from the lens-two position scan measurement (0.45 mrad) is reproduced if the density from the CFD simulations is attenuated smoothly to zero from $z \sim$10 mm (figure 6.13(a)). The need to truncate the density downramp to reproduce the experiment suggests that the model assumption of a pure ion channel is not valid for the entire downramp, probably due to laser diffraction and depletion[xi].

The downramp also causes a shift of the effective source position (as evident in figure 6.13(a)) which affects the retrieved emittance value. For this example the source position shift is approximately 8 mm and leads to a $\sim$14% smaller retrieved

[xi] Without truncating the density profile, the simulated divergence is even smaller than the experimentally measured one.

emittance (see figure 6.14 for a range of offsets). The fitted electron beam energy to this shifted electron beam source is ∼14 MeV below the expected beam energy from the measurement, which is beyond the reasonable experimental error for the measured energy (<10 MeV). Further evidence that the source position shift is probably small comes from the fitted Courant-Snyder parameters. The fitted parameters at the first lens can be back-propagated towards the gas-cell using equation 3.24. The back-propagated beam waist coincides with the physical exit of the accelerator to within 1 mm for the lens-position scans of section 6.2.1. To clarify the effect of the downramp on the divergence and the source position requires further analysis. This could be approached by taking measurements of the density downramp profile (as shown in Weineisen et al. [2011]) in place of the CFD simulations used here and conducting quadrupole-scan measurements for different downramp lengths.

The qualitative agreement of the model with the measurements suggests the possibility of a further reduction by using a longer downramp. Figure 6.13(b) shows that the majority of the divergence decrease occurs within the first few millimetres and is relatively insensitive to longer downramps. In Nakamura et al. [2007] a smaller beam divergence was observed for larger diameter capillaries (and therefore longer density downramps at the exit). Aside from the differences in the laser propagation and electron injection in the different sized plasma channels, the longer downramp offers a further possible cause for the observed reduced divergence. The beam divergence presented here is amongst the smallest published to-date for LWFA beams and can be explained by the longer density downramp of the employed gas cell as opposed to commonly used super-sonic gas jets. To reduce the source divergence further, a separate density peak (in this case $\sim 10^{15}\,\mathrm{cm}^{-3}$) could be incorporated slightly downstream of the main downramp and be used to focus the beam similarly to work being done on plasma lenses [Thompson et al. 2010]. Provided the laser pulse still contains enough energy to create an ion channel, this even promises to focus the entire bunch as opposed to only the rear part for a purely beam-driven plasma lens. This has recently been demonstrated experimentally for LWFA electrons [Thaury et al. 2015]. The benefit of a smaller source divergence is the reduced bunch elongation for a given beam transport system [Weingartner et al. 2011], more relaxed requirements on the beam optics, and a reduced chromatic emittance growth in the drift after the target.

### Virtual source position shift

Figure 6.14 shows the effect of an offset of the electron beam source position on the fitted beam parameters. This means that an emittance is fitted to the same measured beam sizes at the YAG:Ce crystal but the assumed longitudinal position of the source of the electron beam is shifted. The result is that an offset of the source towards lens 1 (source is after the physical exit of the gas cell) leads to a

smaller fitted source size, lower fitted energy, and as a result of these two, a smaller beam emittance. This connection is to be expected from an imaging system and is readily understood using common geometric optics relations. For an imaging system, the ratio of the object size/height to its distance to the principal plane of the lens is equal to the same ratio on the image side, i.e. $h_o/d_o = h_i/d_i$. A change in the object position with constant image height and position therefore leads to: $h_o = h_i/d_i \cdot d_o = kd_o$, a proportional change in the object size. From the thin lens equation ($1/d_o + 1/d_i = 1/f$), it follows that for a constant $d_i$, $f$ must decrease if $d_o$ decreases. For the fitted energy of the electron beam a smaller $d_o$ results in a lower fitted electron beam energy as this corresponds to a shorter focal length $f$ of the magnetic lenses.

The remaining question is at which point the Courant-Snyder parameters should then be calculated if the electron source position is uncertain? The condition is that it must be before the changing beamline element which is the position of lens 2. Therefore any well-defined position between the electron source at the accelerator exit and the end of lens 1 is suitable. Due to the uncertainties of the electron source position, for the results of this thesis the Courant-Snyder parameters were calculated directly upstream of the first lens. The beam parameters can be propagated back towards the accelerator exit using equation 3.24 to obtain the source size and divergence at the beam waist.

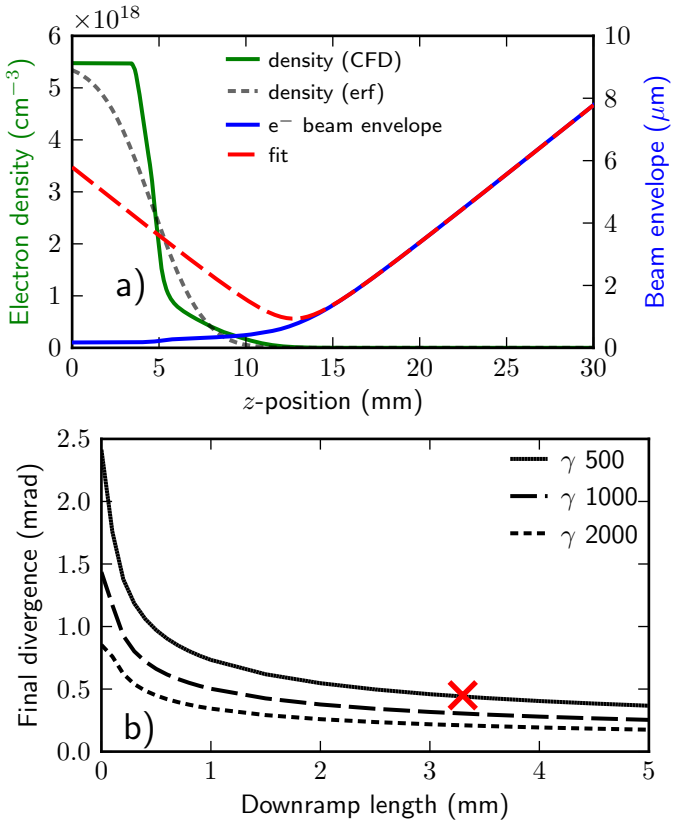


**Figure 6.13. – Simulations of the electron beam envelope and divergence in a downramp. a)**: Evolution of the electron beam envelope (solid blue) in the plasma to vacuum density transition (solid green, based on CFD simulations) according to equation 2.30. The fit line (red dashed) describes an effective electron source with the same emittance as the beam envelope but propagating without the focusing forces of the plasma; the beam waist and divergence are consistent with the values inferred from the lens position scan measurements of figure 6.5. The same effective source is obtained with a downramp modelled by an error function of length 3.3 mm (black dotted). The physical exit of the gas cell is at $z$=5 mm. **b)**: The final divergence after the accelerator downramp as a function of its length, $l$ (where $n_e = n_0(0.5\,\mathrm{erf}(-z/l)+1)$), for three different beam energies with normalised emittances of 0.2 $\pi$·mm·mrad. The cross indicates the case in a).

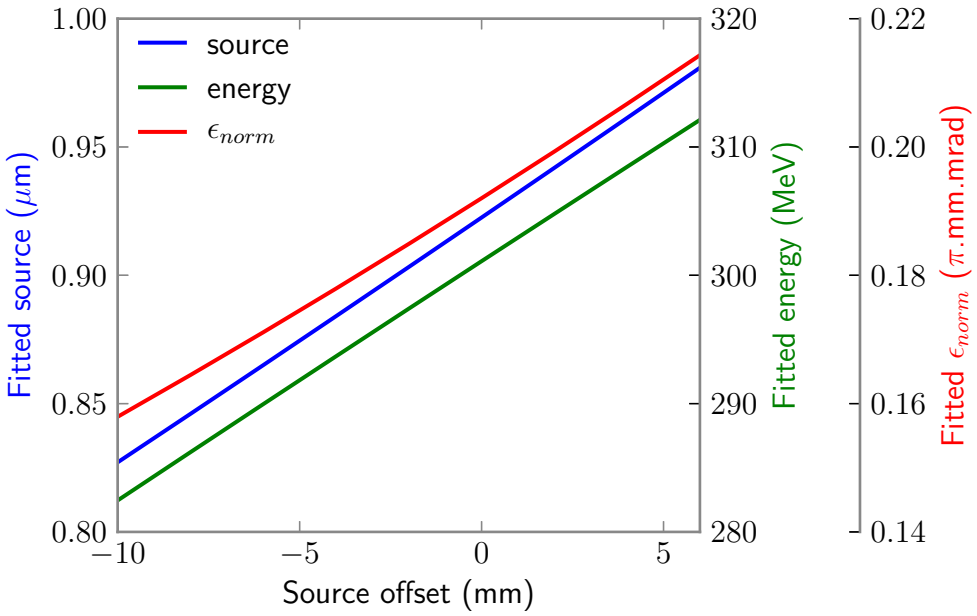


**Figure 6.14. – Effect of longitudinal source position offset on fitted beam parameters.** An offset in the source position (either caused by the density down-ramp or a measurement error of the drift of lens 1) affects the result of the fitted source size, beam energy and beam emittance. A negative source offset represents a shift of the beam source *towards* the lens, effectively decreasing drift 1.

# 7. Conclusions and outlook

The main objective of this thesis was the measurement of the transverse emittance of laser-wakefield accelerated electron beams. The first published results regarding this question used a pepper-pot mask and measured the emittance for a broad range of energies [Fritzler et al. 2004]. A different approach was to use the characteristics of the betatron radiation emitted by the beam while still in the plasma [Kneip et al. 2012]. In this work a modified version of the well-established quadrupole scan method was used. The advantage of this method is that it includes the effects of the plasma-to-vacuum transition and can be spectrally resolving. It is expected from a self-injection LWFA experiment that the spread in injection times leads to a correlation of beam energy and energy spread along the beam (see figure 7.1). Hence a spectrally resolved measurement measures the (longitudinal) *slice* emittance. The slice emittance is an important parameter to be able to design an FEL experiment based on LWFA electron beams. Furthermore the measurement is not susceptible to chromatic emittance growth due to the total energy spread and the divergence of the LWFA beam.

To prepare the emittance experiment, initial experiments employed high-gradient quadrupole lenses to transport LWFA beams. The results were published in Weingartner et al. [2011] and the main findings of these measurements where:

**Bunch-duration-preserving beam transport:** As the PMQ lenses used for these experiments achieve a high magnetic field gradient, the electron beam can be collimated closely behind the plasma accelerator exit where the beam cross-section is still small. This reduces the bunch elongation caused by the path difference between the low- and high-divergence electrons (see figure 3.9).

**Imaging spectrometer:** A common method to determine the spectrum of an electron-beam involves measuring the deflection behind a dipole magnet. As this method makes assumptions concerning the position and angle of the particles entering the dipole field, it delivers inaccurate results for beams with large divergence and pointing fluctuations. By imaging the electron beam, the resolution of the spectrometer could be reduced down to the resolution of the imaging phosphor screen used to measure the beam deflection ($\sim$0.2% FWHM). This allowed the measurement of beams with integrated energy spreads of just 1% rms (see figure 6.3).

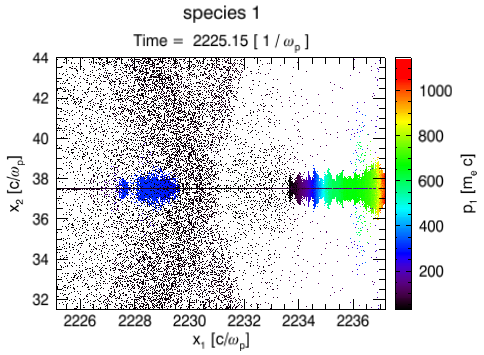


**Figure 7.1. – PIC simulation showing the correlated energy of self-injected LWFA bunch.** This figure shows the same time step as figure 6.10 (zoomed in to the bunch), with the beam energy encoded as colour. The injected electron bunch is leaving the frame on the right-hand side.

**Alignment of the lens doublet:** This was achieved by "desteering" the lenses. The lenses were individually placed in the beam path and adjusted until the electron beam passing through it was not deflected[i]. The effect of a deliberate lens offset can be seen in figure 6.4, where the beam is shown to be steered by several mrad.

**Improvement of the spatial stability of the electron beam:** Despite a broad range of electron energies (>100 MeV), the beam can be collimated and stabilised. In the presented results the summed beam size was reduced by a factor of five (see figure 6.1).

Particle tracking simulations indicate that no beam charge is lost due to clipping at the lens apertures for these experimental results.

In a separate experiment to generate undulator radiation from LWFA electron beams [Fuchs et al. 2009], some further interesting effects concerning beam transport were found. The PMQ focusing system allows to filter a bandwidth of the undulator radiation despite the broad band of energies in the electron beam. This comes from the chromatic focusing of the lenses, only a certain electron energy is collimated. Electrons with other energies will have larger divergences in the undulator. As the undulator radiation emitted by each electron is within a narrow cone of its propagation direction, the undulator radiation beam will have essentially the same size and divergence as the emitting electron beam. The photon beam can therefore

[i] This was done for an average beam position of many shots to compensate for the shot-to-shot fluctuations of the electron beams

be spectrally selected by the lens setup, and additionally be focused on a downstream target. The second aspect is particularly interesting for short-wavelength undulator radiation which would otherwise require multilayer optics to focus.

The stability of the LWFA electron beam source allowed high-resolution measurements of the emittance; the results were published in Weingartner et al. [2012]. The main findings from the emittance measurements where:

**Constant normalised emittance:** The transverse focusing fields in the plasma accelerator are expected to be emittance conserving. This means that the transverse emittance should stay constant if normalised by $\gamma$ to account for the longitudinal acceleration (also known as "adiabatic damping" of the transverse phase space). For the current experiment, the measured emittance was about 0.2 $\pi$·mm·mrad for a range of energies between 245 and 300 MeV.

**Multi- and single-shot methods possible:** The "traditional" method to use quadrupole lenses for an emittance measurement is to change the focal strength of an electric quadrupole. The adaptation for a permanent-magnet quadrupole is to scan the position of a lens. Another method was discovered which utilises a small range of energies of the beam which allow to characterise the beam emittance. The results of the multi- and single-shot methods agree. A single-shot method is particularly relevant for LWFA beams which can vary significantly from shot to shot in comparison to conventionally-accelerated electron beams.

**Accuracy of calculated emittance:** This was explored by considering the factors that could affect the measured data used to calculate the emittance (effect of space charge, lens-position and -field errors) and also the accuracy of the fitting routine itself (bootstrapping). Space charge is not relevant for the energy slices of the beam observed in this experiment as this would lead to a deformation of the measured beam sizes in a scan (asymmetrical flanks) and a shift of the curve in terms of energy or lens position. The tolerances of the fitted parameters was explored using the bootstrapping technique and shows that the fitted parameters are expected to be within $\sim 10\%$ of the calculated values with a 95% confidence interval. The lens-position errors have two potential sources: an incorrect measurement of the lens positions and a shift of the virtual electron source position due to the plasma-to-vacuum transition. The measurement error of the drift length is within 2 mm as the drift from the accelerator to the lens could be directly measured with calipers. The greater potential error comes from the virtual source-position offset which requires empirical analysis for the gas target in question to be determined. The error in the calculated emittance due to the source-position offset can be limited to $< 20\%$ as the fitted energy would otherwise not be plausible.

**Laser heating of the electron beam within the plasma:** It was observed that the electron beam size increases if the accelerator is driven to dephasing. By increasing the plasma density, the laser occupies a larger portion of the wakefield and heats the electrons transversely (see section 6.2.4). Although the data for the length scan of the accelerator is not conclusive, the electron beam could also be heated if the accelerator length is too long (see section 6.2.3). For emittance-sensitive applications of the electron beam the acceleration length, plasma density, and laser-pulse length have to be chosen to avoid this issue.

**Correlation between laser and electron beam position:** Fluctuations in the position of the driver laser focal spot led to corresponding fluctuations in the electron beam source position (see section 6.2.6). An offset between the laser and the electron beam can for example be caused by a pulse-front tilt (PFT) of the laser beam. A PFT can therefore be diagnosed very precisely using the setup described in this work.

**Divergence damping at the accelerator exit:** The decreasing strength of the transverse focusing fields in the plasma-to-vacuum transition lead to an adiabatic damping of the electron beam divergence as the beam size increases (assumption: constant emittance). The increase in beam size is inferred from the expected smaller beam size in the plasma (from PIC simulations, see figure 6.10, and the matched beam size (see equation 2.31), both suggest a size of $x_m \lesssim 0.5\,\mu\text{m}$) relative to the larger calculated virtual source size of $\sim 0.9\,\mu\text{m}$. Furthermore the divergence of the electron beams was the lowest published at the time. Since then, an experiment with a larger energy of 2 GeV has shown smaller divergences of $\sim 0.5$ mrad FWHM [Wang et al. 2013]. Like in the work of this thesis, this experiment used self-injection but was otherwise conducted with a more powerful laser and different plasma densities. From section 3.2.1, it is clear that the transverse momentum of a particle in a beam is related to the divergence and energy of the particle as $p_x \sim \gamma\beta x'$. Considering the effect of adiabatic damping using this relation, the transverse electron momentum in this work is still lower than in the work of [Wang et al. 2013], and also lower than for a more comparable case in terms of energy [Osterhoff et al. 2008] (200 MeV electron beams). The explanation presented in chapter 6 of this thesis suggests that the longer plasma-to-vacuum transition in the present experiment leads to divergence damping. The extension of this idea to use a separate wakefield stage as a laser-plasma lens has been demonstrated experimentally [Thaury et al. 2015].

The following topics could be investigated in further experiments or improve on the above findings:

- The emittance should be calculated for a larger range of energies to better check if the normalised emittance is constant. Given that the experimental parameters would be chosen such that laser heating of the electron bunch within the plasma were not relevant, a constant source size (initially determined during injection) and a decreasing divergence with energy due to adiabatic damping during acceleration would be expected.

- Comparison of the emittance for different injection mechanisms such as longitudinal and transverse self-injection, ionisation injection, density-downramp injection, or colliding-pulse injection: With regards to the experiments performed by [Corde et al. 2013], emittance measurements with the cut-off energy electrons of very short accelerators (longitudinal injection) should show significantly smaller emittances than those conducted with longer accelerators (transverse injection). A challenge for such experiments would be the reduced charge expected for the longitudinal injection regime of about an order of magnitude less than for transversely-injected electrons.

- Correlation between emittance and charge: Beam loading in the plasma during acceleration affects the injection of electrons and therefore the emittance. Just as in the case of laser-beam heating, it would be useful to quantify this effect for emittance-sensitive applications.

- Influence of the laser polarisation axis: In the presented experiments the polarisation axis of the laser was oriented along the dispersion direction of the dipole magnet and the YAG crystal diagnostics measured in the perpendicular plane. It has been observed that the electron beam can interact with the laser while it is still trapped in the wakefield. This leads to an increase of divergence in the laser polarisation plane and has for example been directly controlled by rotating the polarisation axis and observing an identical rotation in the shape of the resulting electron beam [Mangles et al. 2006]. It has also been shown in 3D PIC simulations that the emittance may become substantially larger due to this effect [Németh et al. 2008]. In the light of the need for low emittance beams in both transverse planes for table-top FEL experiments and the discussed effects, it would be important to extend the measurements of this thesis and measure the effect of rotating the laser polarisation axis on the measured emittance.

- Experiments to explore the effect of various plasma-to-vacuum transitions or plasma lensing on the achievable beam divergence and emittance.

# A. Derived emittance and parameter errors

## Emittance fit from data

The electron beam size measurements taken at the YAG:Ce crystal require some analysis to derive the unknown beam parameters such as the emittance. To obtain the electron beam Courant-Snyder parameters at a point in the beamline before the YAG:Ce crystal (for example at the exit of the gas cell) the ideas from section 3.2.2 can be used to derive a fit function such as equation 3.23:

$$x(s_1)^2 = M_{11}^2 \varepsilon \beta(s_0) - 2M_{11}M_{12}\varepsilon\alpha(s_0) + M_{12}^2\varepsilon\gamma(s_0). \tag{A.1}$$

The fit parameters for this function are the beam Courant-Snyder parameters $(\beta(s_0), \alpha(s_0), \gamma(s_0))$ at any position $s_0$ and the left hand side is the square of the beam size at the YAG:Ce crystal. In the experiment multiple measurements are made where the transfer matrix $\boldsymbol{M}$ is varied and the beam size $x(s_1)$ at the YAG:Ce crystal is measured. The "best-fit" parameters are found by using a Levenberg-Marquardt algorithm to minimise $\chi^2$:

$$\chi^2 = \sum_i^N \frac{(x_i - f(\varepsilon, \vec{k}, \boldsymbol{M}))^2}{\sigma_i^2}, \tag{A.2}$$

which is the sum over all offsets of the fit function $f$ from the observed data $x_i$ divided by the expected standard deviation $(\sigma_i)$ of the observed data around the fit function. It is worthwhile to consider the shape of the minimisation function $\chi^2$. The function $f$ is rather complicated due to the transfer matrix $\boldsymbol{M}$ being a product of all beamline element matrices between the YAG:Ce crystal and the point where the Courant-Snyder parameters should be determined. Figure A.1(a) shows how the function looks around the optimal fit parameters for the source size and divergence for the fit shown in figure 6.7(a). It is important to note that the function is convex downward and presumably so also for any relevant fit parameter range. This means that the function has a unique global minimum and a least squares fit algorithm will find the global minimum for $\chi^2$ and not get stuck at some local minimum.

## Fit parameter accuracy

To get an accuracy estimate for the fitted parameters (in the example here the source size and divergence), the bootstrap technique was chosen [Press et al. 2007]. This method creates synthetic data sets by resampling the observed data. This Monte-Carlo method is suitable for cases when the underlying error distribution of the data is unknown and synthetic data sets cannot be generated by drawing from this known distribution. The bootstrap method instead creates synthetic data sets by drawing each data point from the entire observed data set. For example, for observed data points $y_1, y_2, y_3, y_4$ a synthetic bootstrap sample could be any permutation of these values, including duplicates of individual points such as $y_3, y_1, y_4, y_1$. For the lens position scan (see figure 6.5) ∼20 measurements were each taken at ∼10 different lens positions. The bootstrap data for one of the lens positions is generated by drawing 20 times from the observed beam widths at this lens position. This procedure is repeated for every lens position. The electron beam parameters are then fitted to the synthetic data set. By repeating this process many times a distribution of fit parameters is obtained from which a confidence interval can be determined. For the energy scan the synthetic data set is generated based on the *residuals* (= data - fit curve) of the fit routine (see figure 6.7(a)). A resampled residual from the fit to the observed data is added to the fit curve at each energy. A new fit is then found for this synthetic data and this is again repeated many times to obtain a distribution of fit parameters and the associated confidence intervals.

Once the bootstrap samples have been fitted and the resulting parameter distributions obtained, the method of determining the confidence interval has to be decided on. Figures A.1(b) and A.1(c) show the distribution of bootstrap samples for the example used above for a fit to a single shot (figure 6.7(a)). The density distribution shows the bootstrap samples and the observed values for the fitted emittance. As the median bootstrap sample value agrees very well with the observed value, the bootstrap samples are centred on the observed values, i.e. there is no *bias* in the bootstrap distribution. Figure A.1(c) shows three methods of determining the confidence intervals from the distribution of the bootstrap samples. The simplest method is to set the boundaries for each variable independently such that 95% (for a 95% confidence interval) of the bootstrap samples are contained. In this example, it is more useful to give the joint confidence interval for both fitted parameters as they both go into the product for the desired quantity, the fitted beam emittance. According to Press et al. [2007] the most common choice for the confidence region is a contour of the $\Delta\chi^2$ function used in the fitting routine, in this case the contour should contain 95% of the bootstrap samples. Another option which will be the process used for the errors in this thesis is to sort the bootstrap samples according to their offset to the median emittance. The shape of the confidence region is then determined by including the 95% closest bootstrap samples to the median emittance.

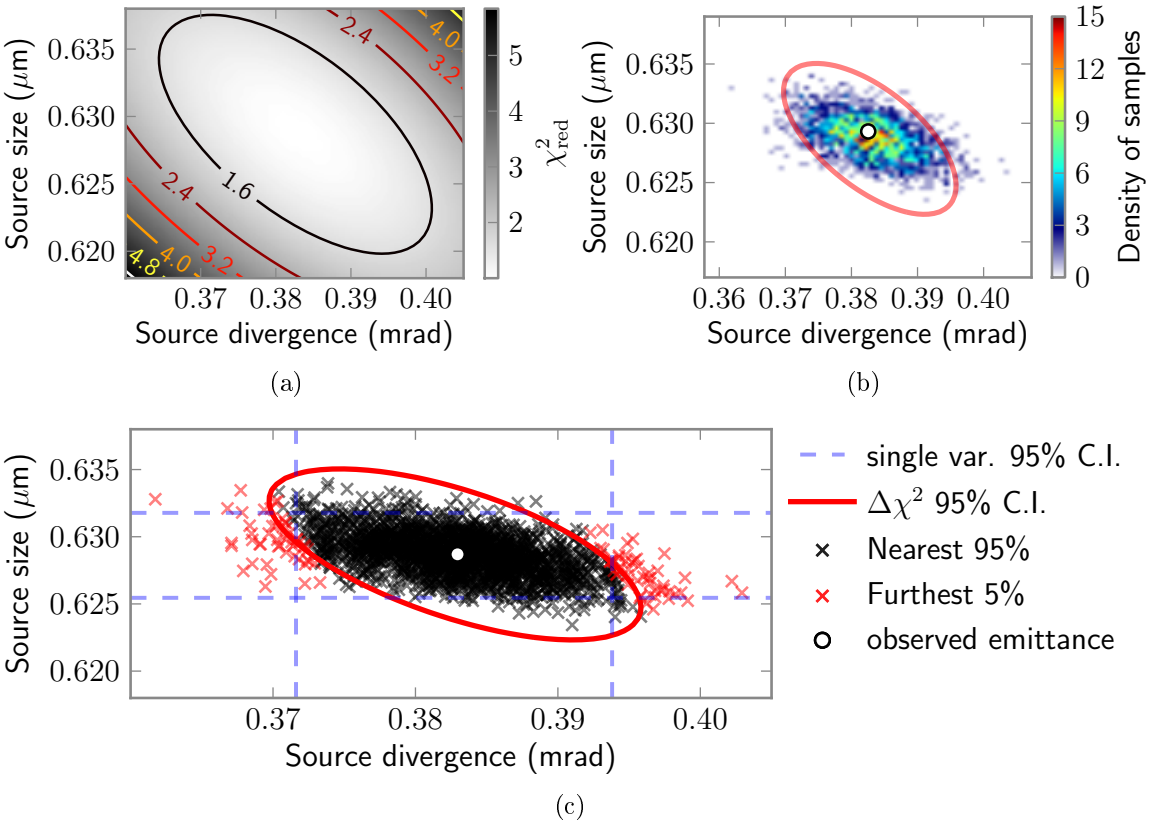


**Figure A.1. – Fitting beam parameters and the associated errors.** a) Reduced $\chi^2$ for the fit parameters source size and source divergence for the data shown in figure 6.7(a). b) Distribution of 2000 bootstrap samples (residual resampling). c) Three possible ways to give an error estimate of the fitted parameters from the bootstrap distribution. For each case 95% of all the bootstrap samples are 'enclosed' within the chosen shape boundary, the shape varies between the methods. 1. Square shape (blue dashed lines): the 95% C.I. for each parameter is obtained independently of the other parameter. 2. Constant $\chi^2$ boundary (red contour): use a contour of $\chi^2$ which includes 95% of all bootstrap samples. 3. Smallest emittance offset (black crosses): the shape is such that it contains the 95% of the bootstrap sample closest to the median fit emittance (white circle). The red crosses correspond to remaining 5% of samples outside of the confidence region for this shape.

The confidence limits for the parameters are then the lowest and highest values from all of the included samples. The three methods are compared in table A.1. As the $\Delta\chi^2$ contours do not always line up with the bootstrap sample distribution, the error from this method will always be larger than the "nearest emittance" method.

**Table A.1. – Bootstraps confidence intervals.** The confidence intervals as shown in figure A.1(c). The units for the source are in $\mu$m, those for divergence in mrad, and those for emittance in $\pi$·mm·mrad. The observed values are the fit values from the real experimental data.

| Parameter | C.I. method | Observed | Upper bound | Lower bound |
|---|---|---|---|---|
| Source | Single variable | 0.629 | 0.003 | −0.003 |
| " | $\Delta\chi^2$ | " | 0.006 | −0.006 |
| " | Nearest emittance | " | 0.005 | −0.005 |
| Divg. | Single variable | 0.383 | 0.011 | −0.011 |
| " | $\Delta\chi^2$ | " | 0.013 | −0.013 |
| " | Nearest emittance | " | 0.013 | −0.013 |
| Emittance | Nearest emittance | 0.143 | 0.004 | −0.004 |

# Bibliography


`http://www.pulsar.nl/gpt`. General Particle Tracer, accessed 01.02.2016.

Estar database. `http://physics.nist.gov/PhysRefData/Star/Text/method.html`. The range is calculated by using the the continuous-slowing-down approximation (CSDA). In this approximation, the rate of energy loss at every point along the track is assumed to be equal to the total stopping power. Energy-loss fluctuations are neglected. The CSDA range is obtained by integrating the reciprocal of the total stopping power with respect to energy. The YAG:Ce crystal was entered in the ESTAR database as a composite material weighted by the atomic mass of its constituent elements: $Y_3Al_5O_{12} \rightarrow$ Y 266.7, Al 134.9, O 192.0. Website accessed: 14.07.2011.

`http://www.zemax.com`. Zemax ray tracing software.

S. G. Anderson and J. B. Rosenzweig. Space-charge effects in high brightness electron beam emittance measurements. *Physical Review Special Topics - Accelerators and Beams*, 5(1):1–12, (2002).

S. Becker, M. Bussmann, S. Raith, M. Fuchs, R. Weingartner, P. Kunz, W. Lauth, U. Schramm, M. El Ghazaly, F. Grüner, H. Backe, D. Habs, S. Schramm, and M. E. Ghazaly. Characterization and Tuning of Ultra High Gradient Permanent Magnet Quadrupoles. *Phys. Rev. ST Accel. Beams*, 12:102801, (2009).

H. A. Bethe. Moliere's theory of multiple scattering. *Physical Review*, 89(6):1256–1266, (1953).

K. L. Brown, D. C. Carey, F. C. Iselin, and F. Rothacker. *TRANSPORT: a computer program for designing charged-particle beam-transport systems; 3rd ed.* CERN, Geneva, (1980). Also publ. as SLAC and FERMILAB.

E. Brunetti, R. Shanks, G. Manahan, M. Islam, B. Ersfeld, M. Anania, S. Cipiccia, R. Issac, G. Raj, G. Vieux, G. Welsh, S. Wiggins, and D. Jaroszynski. Low Emittance, High Brilliance Relativistic Electron Beams from a Laser-Plasma Accelerator. *Physical Review Letters*, 105(21):3–6, (2010).

A. Buck, K. Zeil, A. Popp, K. Schmid, A. Jochmann, S. D. Kraft, B. Hidding, T. Kudyakov, C. M. S. Sears, L. Veisz, S. Karsch, J. Pawelke, R. Sauerbrey, T. Cowan, F. Krausz, and U. Schramm. Absolute charge calibration of scintillating screens for relativistic electron detection. *Review of Scientific Instruments*, 81(3): 033301, (2010).

A. Buck, M. Nicolai, K. Schmid, C. M. S. Sears, A. Sävert, J. M. Mikhailova, F. Krausz, M. C. Kaluza, and L. Veisz. Real-time observation of laser-driven electron acceleration. *Nature Physics*, 7(7):543–548, (2011).

CAWO, Website accessed: 08.10.2017. `http://www.cawo.com/products/intensifying-screens/green-emitting/`.

A. Cianchi, M. P. Anania, M. Bellaveglia, M. Castellano, E. Chiadroni, M. Ferrario, G. Gatti, B. Marchetti, A. Mostacci, R. Pompili, C. Ronsivalle, A. R. Rossi, and L. Serafini. Challenges in plasma and laser wakefield accelerated beams diagnostic. *Nuclear Instruments and Methods in Physics Research, Section A: Accelerators, Spectrometers, Detectors and Associated Equipment*, 720:153–156, (2013).

M. Conte and W. MacKay. *An Introduction to the Physics of Particle Accelerators*. World Scientific, (2008). ISBN 9789812779601.

S. Corde, C. Thaury, a. Lifschitz, G. Lambert, K. Ta Phuoc, X. Davoine, R. Lehe, D. Douillet, a. Rousse, and V. Malka. Observation of longitudinal and transverse self-injections in laser-plasma accelerators. *Nature communications*, 4:1501, (2013).

B. M. Cowan, S. Y. Kalmykov, a. Beck, X. Davoine, K. Bunkers, a. F. Lifschitz, E. Lefebvre, D. L. Bruhwiler, B. a. Shadwick, and D. P. Umstadter. Computationally efficient methods for modelling laser wakefield acceleration in the blowout regime. *Journal of Plasma Physics*, 78(04):469–482, (2012).

B. Cowan, D. Bruhwiler, J. Cary, E. Cormier-Michel, and C. Geddes. Generalized algorithm for control of numerical dispersion in explicit time-domain electromagnetic simulations. *Physical Review Special Topics - Accelerators and Beams*, 16 (4):041303, (2013).

Crytur, Website accessed: 11.07.2011. `http://www.crytur.cz/`.

G. Datzmann, G. Dollinger, G. Hinderer, and H. Korner. A superconducting multipole lens for focusing high energy ions. *Nuclear Instruments and Methods in Physics Research Section B: Beam Interactions with Materials and Atoms*, 158 (1-4):74–80, (1999).

T. Eichner, F. Grüner, S. Becker, M. Fuchs, D. Habs, R. Weingartner, U. Schramm, H. Backe, P. Kunz, and W. Lauth. Miniature magnetic devices for laser-based, table-top free-electron lasers. *Physical Review Special Topics - Accelerators and Beams*, 10(8):82401, (2007).

P. Emma and H. D. Nuhn. Quadrupole magnet error sensitivities for FODO-cell and triplet lattices in the LCLS undulator. Technical Report LCLS-TN-2000-5. SLAC-TN-2005-038, SLAC, Stanford, CA, (2000).

E. Esarey, P. Sprangle, J. Krall, and a. Ting. Overview of plasma-based accelerator concepts. *IEEE Transactions on Plasma Science*, 24(2):252–288, (1996).

E. Esarey, B. Shadwick, P. Catravas, and W. Leemans. Synchrotron radiation from electron beams in plasma-focusing channels. *Physical Review E*, 65(5):1–15, (2002).

E. Esarey, C. Schroeder, and W. Leemans. Physics of laser-driven plasma-based electron accelerators. *Reviews of Modern Physics*, 81(3):1229–1285, (2009).

E. Esarey and M. Pilloff. Trapping and acceleration in nonlinear plasma waves. *Physics of Plasmas*, 2(5):1432, (1995).

J. Faure, Y. Glinec, A. Pukhov, S. Kiselev, S. Gordienko, E. Lefebvre, J. P. Rousseau, F. Burgy, and V. Malka. A laser-plasma accelerator producing monoenergetic electron beams. *Nature*, 431(7008):541–544, (2004).

J. Faure, C. Rechatin, A. Norlin, A. Lifschitz, Y. Glinec, and V. Malka. Controlled injection and acceleration of electrons in plasma wakefields by colliding laser pulses. *Nature*, 444(7120):737–739, (2006).

R. Fonseca, L. Silva, F. Tsung, V. Decyk, W. Lu, C. Ren, W. Mori, S. Deng, S. Lee, T. Katsouleas, and J. Adam. Osiris: A three-dimensional, fully relativistic particle in cell code for modeling plasma based accelerators. In P. Sloot, A. Hoekstra, C. Tan, and J. Dongarra, editors, *Computational Science - ICCS 2002*, volume 2331 of *Lecture Notes in Computer Science*, pages 342–351. Springer Berlin Heidelberg, (2002). ISBN 978-3-540-43594-5.

S. Fritzler, E. Lefebvre, V. Malka, F. Burgy, a. E. Dangor, K. Krushelnick, S. P. D. Mangles, Z. Najmudin, J.-P. Rousseau, and B. Walton. Emittance Measurements of a Laser-Wakefield-Accelerated Electron Beam. *Physical Review Letters*, 92(16): 165006, (2004).

M. Fuchs, R. Weingartner, A. Popp, Z. Major, S. Becker, J. Osterhoff, I. Cortrie, B. Zeitler, R. Hörlein, G. D. Tsakiris, U. Schramm, T. P. Rowlands-Rees, S. M.

Hooker, D. Habs, F. Krausz, S. Karsch, and F. Grüner. Laser-driven soft-X-ray undulator source. *Nature Physics*, 5(11):826–829, (2009).

J. G. Gallacher, M. P. Anania, E. Brunetti, F. Budde, A. Debus, B. Ersfeld, K. Haupt, M. R. Islam, O. Jäckel, S. Pfotenhauer, A. J. W. Reitsma, E. Rohwer, H. P. Schlenvoigt, H. Schwoerer, R. P. Shanks, S. M. Wiggins, and D. A. Jaroszynski. A method of determining narrow energy spread electron beams from a laser plasma wakefield accelerator using undulator radiation. *Physics of Plasmas*, 16(9):1–8, (2009).

C. G. R. Geddes, C. Toth, J. van Tilborg, E. Esarey, C. B. Schroeder, D. Bruhwiler, C. Nieter, J. Cary, W. P. Leemans, and J. V. Tilborg. High-quality electron beams from a laser wakefield accelerator using plasma-channel guiding. *Nature*, 431(7008):538–541, (2004).

C. G. R. Geddes, K. Nakamura, G. R. Plateau, C. Toth, E. Cormier-Michel, E. Esarey, C. B. Schroeder, J. R. Cary, and W. P. Leemans. Plasma-density-gradient injection of low absolute-momentum-spread electron bunches. *Physical Review Letters*, 100(21):1–4, (2008).

F. Grüner, S. Becker, U. Schramm, T. Eichner, M. Fuchs, R. Weingartner, D. Habs, J. Meyer-ter Vehn, M. Geissler, M. Ferrario, L. Serafini, B. van der Geer, H. Backe, W. Lauth, and S. Reiche. Design considerations for table-top, laser-based VUV and X-ray free electron lasers. *Applied Physics B*, 86(3):431–435, (2007).

F. Grüner, C. Schroeder, a. Maier, S. Becker, and J. Mikhailova. Space-charge effects in ultrahigh current electron bunches generated by laser-plasma accelerators. *Physical Review Special Topics - Accelerators and Beams*, 12(2):1–11, (2009).

C. Grupen. Physics of particle detection. ICFA Instrumentation School, Capetown, (2001).

E. Hecht. *Optics*. Addison-Wesley, (2002). ISBN 9780805385663.

S. Karsch, J. Osterhoff, a. Popp, T. P. Rowlands-Rees, Z. Major, M. Fuchs, B. Marx, R. Hörlein, K. Schmid, L. Veisz, S. Becker, U. Schramm, B. Hidding, G. Pretzler, D. Habs, F. Grüner, F. Krausz, and S. M. Hooker. GeV-scale electron acceleration in a gas-filled capillary discharge waveguide. *New Journal of Physics*, 9(11):415–415, (2007).

S. Kneip, C. McGuffey, J. Martins, M. Bloom, V. Chvykov, F. Dollar, R. Fonseca, S. Jolly, G. Kalintchenko, K. Krushelnick, a. Maksimchuk, S. Mangles, Z. Najmudin, C. Palmer, K. Phuoc, W. Schumaker, L. Silva, J. Vieira, V. Yanovsky, and a. Thomas. Characterization of transverse beam emittance of electrons from

a laser-plasma wakefield accelerator in the bubble regime using betatron x-ray radiation. *Physical Review Special Topics - Accelerators and Beams*, 15(2):2–6, (2012).

I. Kostyukov, E. Nerush, A. Pukhov, and V. Seredov. A multidimensional theory for electron trapping by a plasma wake generated in the bubble regime. *New Journal of Physics*, 12(4):045009, (2010).

M. Krus, T. Levato, H. T. Kim, G. Grittani, D. Margarone, T. M. Jeong, T. Mocek, and G. Korn. First experimental test of quadrupole lens-free multiple profile monitor technique for electron beam emittance measurement with a PW laser system. In G. Korn and L. O. Silva, editors, *Proc. SPIE*, volume 9515, page 95151K, (2015). ISBN 9781628416367.

C. Lechner. Energy-filtering of laser-driven electrons with high-gradient magnetic lenses. Diploma thesis, Ludwig-Maximilians Universität, (2011).

R. Lehe, a. Lifschitz, C. Thaury, V. Malka, and X. Davoine. Numerical growth of emittance in simulations of laser-wakefield acceleration. *Physical Review Special Topics - Accelerators and Beams*, 16(2):021301, (2013).

J. Lim, P. Frigola, G. Travish, J. Rosenzweig, S. Anderson, W. Brown, J. Jacob, C. Robbins, and a. Tremaine. Adjustable, short focal length permanent-magnet quadrupole based electron beam final focus system. *Physical Review Special Topics - Accelerators and Beams*, 8(7):1–17, (2005).

W. Lu, M. Tzoufras, C. Joshi, F. Tsung, W. Mori, J. Vieira, R. Fonseca, and L. Silva. Generating multi-GeV electron bunches using single stage laser wakefield acceleration in a 3D nonlinear regime. *Physical Review Special Topics - Accelerators and Beams*, 10(6):061301, (2007).

A. Lumpkin, B. Yang, W. Berg, M. White, J. Lewellen, and S. Milton. Optical techniques for electron-beam characterizations on the APS SASE FEL project1. *Nuclear Instruments and Methods in Physics Research Section A: Accelerators, Spectrometers, Detectors and Associated Equipment*, 429(1-3):336–340, (1999).

O. Lundh, J. Lim, C. Rechatin, L. Ammoura, A. Ben-Ismaïl, X. Davoine, G. Gallot, J.-P. Goddet, E. Lefebvre, V. Malka, and J. Faure. Few femtosecond, few kiloampere electron bunch produced by a laser-plasma accelerator. *Nature Physics*, 7(3):219–222, (2011).

G. R. Lynch and O. I. Dahl. Approximations to multiple Coulomb scattering. *Nuclear Inst. and Methods in Physics Research, B*, 58(1):6–10, (1991).

A. R. Maier, A. Meseck, S. Reiche, C. B. Schroeder, T. Seggebrock, and F. Grüner. Demonstration scheme for a laser-plasma-driven free-electron laser. *Physical Review X*, 2(3):1–7, (2012).

K. Makino and M. Berz. COSY INFINITY Version 9. *Nuclear Instruments and Methods in Physics Research Section A: Accelerators, Spectrometers, Detectors and Associated Equipment*, 558(1):346–350, (2006).

G. G. Manahan, E. Brunetti, C. Aniculaesei, M. P. Anania, S. Cipiccia, M. R. Islam, D. W. Grant, a. Subiel, R. P. Shanks, R. C. Issac, G. H. Welsh, S. M. Wiggins, and D. a. Jaroszynski. Characterization of laser-driven single and double electron bunches with a permanent magnet quadrupole triplet and pepper-pot mask. *New Journal of Physics*, 16(10):103006, (2014).

S. Mangles, A. Thomas, M. Kaluza, O. Lundh, F. Lindau, A. Persson, F. Tsung, Z. Najmudin, W. Mori, C.-G. Wahlström, and K. Krushelnick. Laser-Wakefield Acceleration of Monoenergetic Electron Beams in the First Plasma-Wave Period. *Physical Review Letters*, 96(21):1–4, (2006).

S. P. D. Mangles, C. D. Murphy, Z. Najmudin, A. G. R. Thomas, J. L. Collier, A. E. Dangor, E. J. Divall, P. S. Foster, J. G. Gallacher, C. J. Hooker, D. A. Jaroszynski, A. J. Langley, W. B. Mori, P. A. Norreys, F. S. Tsung, R. Viskup, B. R. Walton, and K. Krushelnick. Monoenergetic beams of relativistic electrons from intense laser-plasma interactions. *Nature*, 431(7008):535–538, (2004).

S. P. D. Mangles, a. G. R. Thomas, O. Lundh, F. Lindau, M. C. Kaluza, a. Persson, C.-G. Wahlstrom, K. Krushelnick, and Z. Najmudin. On the stability of laser wakefield electron accelerators in the monoenergetic regime. *Physics of Plasmas*, 14(5):056702, (2007).

S. F. Martins, R. a. Fonseca, W. Lu, W. B. Mori, and L. O. Silva. Exploring laser-wakefield-accelerator regimes for near-term lasers using particle-in-cell simulation in Lorentz-boosted frames. *Nature Physics*, 6(4):311–316, (2010).

T. Matsuoka, C. McGuffey, P. G. Cummings, S. S. Bulanov, V. Chvykov, F. Dollar, Y. Horovitz, G. Kalintchenko, K. Krushelnick, P. Rousseau, a. G. R. Thomas, V. Yanovsky, and A. Maksimchuk. On electron betatron motion and electron injection in laser wakefield accelerators. *Plasma Phys Contr. F.*, 56(8):084009, (2014).

A. Murokh, J. Rosenzweig, V. Yakimenko, E. Johnson, and X. J. Wang. Limitations on the Resolution of Yag:Ce Beam Profile Monitor for High Brightness Electron Beam. *The Physics of High Brightness Beams*, pages 564–580, (2000).

K. Nakamura. Review of Particle Physics. *Journal of Physics G: Nuclear and Particle Physics*, 37(7A):075021, (2010).

K. Nakamura, B. Nagler, C. Toth, C. G. R. Geddes, C. B. Schroeder, E. Esarey, W. P. Leemans, a. J. Gonsalves, and S. M. Hooker. GeV electron beams from a centimeter-scale channel guided laser wakefield accelerator. *Physics of Plasmas*, 14(5):056708, (2007).

K. Nakamura, W. Wan, N. Ybarrolaza, D. Syversrud, J. Wallig, and W. P. Leemans. Broadband single-shot electron spectrometer for GeV-class laser-plasma-based accelerators. *Review of Scientific Instruments*, 79(5):53301, (2008).

K. Németh, B. Shen, Y. Li, H. Shang, R. Crowell, K. Harkay, and J. Cary. Laser-Driven Coherent Betatron Oscillation in a Laser-Wakefield Cavity. *Physical Review Letters*, 100(9):1–4, (2008).

openFOAM, computational fluid dynamics code. `www.openfoam.org`.

J. Osterhoff, A. Popp, Z. Major, B. Marx, T. Rowlands-Rees, M. Fuchs, M. Geissler, R. Hörlein, B. Hidding, S. Becker, E. A. Peralta, U. Schramm, F. Grüner, D. Habs, F. Krausz, S. M. Hooker, S. Karsch, and R. T. P. Rees. Generation of Stable, Low-Divergence Electron Beams by Laser-Wakefield Acceleration in a Steady-State-Flow Gas Cell. *Phys. Rev. Lett.*, 101(8):085002, (2008).

J. Osterhoff. *Stable, ultra-relativistic electron beams by laser-wakefield acceleration.* PhD thesis, Ludwig Maximilians Universität, München, (2008).

G. R. Plateau, C. G. R. Geddes, D. B. Thorn, M. Chen, C. Benedetti, E. Esarey, a. J. Gonsalves, N. H. Matlis, K. Nakamura, C. B. Schroeder, S. Shiraishi, T. Sokollik, J. van Tilborg, C. Toth, S. Trotsenko, T. S. Kim, M. Battaglia, T. Stöhlker, and W. P. Leemans. Low-Emittance Electron Bunches from a Laser-Plasma Accelerator Measured using Single-Shot X-Ray Spectroscopy. *Physical Review Letters*, 109(6):064802, (2012).

A. Popp, J. Vieira, J. Osterhoff, Z. Major, R. Hörlein, M. Fuchs, R. Weingartner, T. P. Rowlands-Rees, M. Marti, R. A. Fonseca, S. F. Martins, L. O. Silva, S. M. Hooker, F. Krausz, F. Grüner, and S. Karsch. All-Optical Steering of Laser-Wakefield-Accelerated Electron Beams. *Physical Review Letters*, 105(21):215001, (2010).

A. Popp. *Dynamics of electron acceleration in laser-driven wakefields: Acceleration limits and asymmetric plasma waves.* PhD thesis, Ludwig Maximilians Universität, München, (2011).

W. H. Press, S. A. Teukolsky, W. T. Vetterling, and B. P. Flannery. *Numerical Recipes 3rd Edition: The Art of Scientific Computing.* Cambridge University Press, 3 edition, (2007). ISBN 0521880688.

S. Raith. Characterization and tuning of higher order field components in high-gradient miniature quadrupoles. Diploma thesis, Ludwig-Maximilians Universität, (2009).

C. Rechatin, J. Faure, a. Ben-Ismail, J. Lim, R. Fitour, a. Specka, H. Videau, a. Tafzi, F. Burgy, and V. Malka. Controlling the Phase-Space Volume of Injected Electrons in a Laser-Plasma Accelerator. *Phys. Rev. Lett.*, 102(16):1–4, (2009).

M. Reiser. *Theory and design of charged particle beams.* Wiley Series in Beam Physics and Accelerator Technology. Wiley-VCH, (2008). ISBN 9783527407415.

K. Schmid, a. Buck, C. Sears, J. Mikhailova, R. Tautz, D. Herrmann, M. Geissler, F. Krausz, and L. Veisz. Density-transition based electron injector for laser driven wakefield accelerators. *Physical Review Special Topics - Accelerators and Beams*, 13(9):1–5, (2010).

M. Schnell, A. Sävert, B. Landgraf, M. Reuter, M. Nicolai, O. Jäckel, C. Peth, T. Thiele, O. Jansen, A. Pukhov, O. Willi, M. C. Kaluza, and C. Spielmann. Deducing the Electron-Beam Diameter in a Laser-Plasma Accelerator Using X-Ray Betatron Radiation. *Physical Review Letters*, 108(7):075001, (2012).

C. Schroeder, E. Esarey, C. Geddes, C. Benedetti, and W. Leemans. Physics considerations for laser-plasma linear colliders. *Physical Review Special Topics - Accelerators and Beams*, 13(10):1–11, (2010).

C. Schroeder, C. Benedetti, E. Esarey, and W. Leemans. Nonlinear Pulse Propagation and Phase Velocity of Laser-Driven Plasma Waves. *Physical Review Letters*, 106(13):1–4, (2011).

C. B. Schroeder, E. Esarey, B. a. Shadwick, and W. P. Leemans. Trapping, dark current, and wave breaking in nonlinear plasma waves. *Physics of Plasmas*, 13 (3):033103, (2006).

C. Sears, A. Buck, K. Schmid, J. Mikhailova, F. Krausz, and L. Veisz. Emittance and divergence of laser wakefield accelerated electrons. *Physical Review Special Topics - Accelerators and Beams*, 13(9):92803, (2010)a.

C. M. S. Sears, S. B. Cuevas, U. Schramm, K. Schmid, A. Buck, D. Habs, F. Krausz, and L. Veisz. A high resolution, broad energy acceptance spectrometer for laser wakefield acceleration experiments. *Review of Scientific Instruments*, 81(7):73304, (2010)b.

P. Sprangle, E. Esarey, and A. Ting. Nonlinear theory of intense laser-plasma interactions. *Physical review letters*, 64(17):2011–2014, (1990).

G.-Z. Sun, E. Ott, Y. C. Lee, and P. Guzdar. Self-focusing of short intense pulses in plasmas. *Physics of Fluids*, 30(1987):526, (1987).

T. Tajima and J. M. Dawson. Laser Electron Accelerator. *Physical Review Letters*, 43(4):267–270, (1979).

C. Thaury, E. Guillaume, A. Döpp, R. Lehe, A. Lifschitz, K. Ta Phuoc, J. Gautier, J.-P. Goddet, A. Tafzi, A. Flacco, F. Tissandier, S. Sebban, A. Rousse, and V. Malka. Demonstration of relativistic electron beam focusing by a laser-plasma lens. *Nature Communications*, 6:6860, (2015).

A. G. R. Thomas. Scalings for radiation from plasma bubbles. *Physics of Plasmas*, 17(5):056708, (2010).

A. G. R. Thomas, Z. Najmudin, S. P. D. Mangles, C. D. Murphy, A. E. Dangor, C. Kamperidis, K. L. Lancaster, W. B. Mori, P. A. Norreys, W. Rozmus, and K. Krushelnick. Effect of laser-focusing conditions on propagation and monoenergetic electron production in laser-wakefield accelerators. *Physical Review Letters*, 98(9):2–5, (2007).

C. Thomas, N. Delerue, and R. Bartolini. Single shot 3 GeV electron transverse emittance with a pepper-pot. *Nuclear Instruments and Methods in Physics Research, Section A: Accelerators, Spectrometers, Detectors and Associated Equipment*, 729: 554–556, (2013).

M. C. Thompson, H. Badakov, J. B. Rosenzweig, G. Travish, N. Barov, P. Piot, R. Fliller, G. M. Kazakevich, J. Santucci, J. Li, and R. Tikhoplav. Observations of low-aberration plasma lens focusing of relativistic electron beams at the underdense threshold. *Physics of Plasmas*, 17(7):073105, (2010).

F. S. Tsung, W. Lu, M. Tzoufras, W. B. Mori, C. Joshi, J. M. Vieira, L. O. Silva, and R. a. Fonseca. Simulation of monoenergetic electron generation via laser wakefield accelerators for 5-25 TW lasers. *Physics of Plasmas*, 13(5):056708, (2006).

S. Vaganian and H. Henke. The Panofsky-Wenzel Theorem and General Relations for the Wake Potential. *Particle Accelerators*, 48(3):239–242, (1995).

X. Wang, R. Zgadzaj, N. Fazel, Z. Li, S. A. Yi, X. Zhang, W. Henderson, Y.-Y. Y.-Y. Chang, R. Korzekwa, H.-E. H.-E. Tsai, C.-H. C.-H. Pai, H. Quevedo, G. Dyer, E. Gaul, M. Martinez, A. C. Bernstein, T. Borger, M. Spinks, M. Donovan, V. Khudik, G. Shvets, T. Ditmire, and M. C. Downer. Quasi-monoenergetic

laser-plasma acceleration of electrons to 2 GeV. *Nature Communications*, 4(May): 1988, (2013).

T. Weineisen, B. Göppner, K. Schmid, M. Fuchs, H. Schröder, S. Karsch, and F. Grüner. Density measurement in a laser-plasma-accelerator capillary using Raman scattering. *Physical Review Special Topics - Accelerators and Beams*, 14 (5):1–5, (2011).

R. Weingartner, M. Fuchs, A. Popp, S. Raith, S. Becker, S. Chou, M. Heigoldt, J. Wenz, B. Zeitler, Z. Major, J. Osterhoff, F. Krausz, S. Karsch, F. Gr, K. Khrennikov, T. Seggebrock, and F. Grüner. Imaging laser-wakefield-accelerated electrons using miniature magnetic quadrupole lenses. *Physical Review Special Topics - Accelerators and Beams*, 14(5):052801, (2011).

R. Weingartner, S. Raith, A. Popp, S. Chou, J. Wenz, K. Khrennikov, M. Heigoldt, A. R. Maier, N. Kajumba, M. Fuchs, B. Zeitler, F. Krausz, S. Karsch, and F. Grüner. Ultralow emittance electron beams from a laser-wakefield accelerator. *Physical Review Special Topics - Accelerators and Beams*, 15(11):111302, (2012).

K. Wille. *The Physics of Particle Accelerators: An Introduction*. Oxford University Press, (2001).

M. Winkler, V. Chichkine, K. H. Behr, H. Geissel, S. Eliseev, A. Kalimov, G. Li, G. Münzenberg, W. R. Plaß, C. Scheidenberger, Z. Wang, H. Weick, and H. Wollnik. Development and test of iron-free quadrupole lenses with high magnetic flux densities. *Nuclear Instruments and Methods in Physics Research, Section B: Beam Interactions with Materials and Atoms*, 204:454–459, (2003).

H. Wollnik. *Optics of charged particles*. Academic Press, (1987). ISBN 9780127621302.

# Acknowledgements

The work that lead to this thesis could not have been achieved without a great deal of help from many people. As it's been quite some time since I actively worked at the MPQ/LMU, I hope I don't forget anyone and I apologise here if I do. A big thank you to:

**Prof. Dr. Florian Grüner** Thank you for your guidance, motivation, and patience with me and making it possible for me to complete this thesis! Due to your broad physical understanding and mastery of "back-of-the-envelope" calculations, I learned a lot from discussions with you. Thank you for giving me the opportunity to travel to conferences and to collaborating groups around the world. Working with you was always enlightening, uncomplicated, and a lot of fun, danke Vati!

**Prof. Dr. Stefan Karsch** I was very fortunate that the experimental work for this thesis meant a close collaboration with you and your group. As an experimentalist, it is invaluable to have a "jack-of-all-trades" with helpful advice on any problems that arise. For some reason, problems turned up at all times of day and night in the lab, thank you for all of your help! You also had a big influence in helping me interpret the physics happening in the experiment and taught me to always wear my laser goggles in the lab.

**Prof. Dr. Jörg Schreiber** Thank you for being second referee and reviewing this thesis.

**Prof. Dr. Ferenc Krausz** Thank you for bringing together the outstanding people and infrastructure at the high-field physics group and providing such a unique environment for me to work in.

**Prof. Dr. Dieter Habs** Dieter was my initial supervisor until Florian was able to take over as Professor. He was the driver of many interesting ideas that our group pursued and I will never forget his energetic lectures which contained the most orders of magnitude I have ever heard.

**Dr. Matthias Fuchs and Dr. Antonia Popp** A significant proportion of my hours in the lab were spent with these two, it was a pleasure to work with you. Thank

you so much for your support even though the hours were long (we were often the first customers when the bakery opened in Garching). I now also believe that "Ride the lightning" was their best album and have a much greater appreciation of the colour magenta.

**Konstantin Khrennikov, Matthias Heigoldt, Johannes Wenz** They go by many names "Das Triumvirat", Bljeds (?), Upstairs scientists. Your complete disregard for the time of day and your willingness to help made my experiments possible. Thanks for your humour and dedication. I'm sorry you had to measure so many parabolas.

**The FEL team** Thank you for being such a cheerful and helpful lot. Special thanks to **Stefan Becker** for coming up with such a clever way to tune the magnetic lenses, enabling the emittance measurement in the first place. **Sebastian Raith** for actually tuning the lenses and being a big help in the lab setting up the experiment and making the measurements despite having children at home! **Irene Dornmair** thank you for carefully proof-reading this thesis and your helpful suggestions!

**Dr. Zsuzsanna Major-Slattery and Dr. Jens Osterhoff** From my perspective the "first-generation electron accelerators". They built up most of the experimental infrastructure which I could later thankfully use to conduct my experiments. With Zsuzsi I also learned my first steps with high-power lasers.

**The high-field group at MPQ** Aside from labwork, we also spent quite some hours filming and producing some great moments in amateur film history. Modern classics including "A quantum of optics" and "Sendung mit der Mausz" where we tried to find out where all of those Thorlabs lab snacks were disappearing to.... Special thanks to **Christoph Wandt, Sandro Klingebiel, Christoph Skrobol, Alexander "Jaws" Buck** for making my time at MPQ so enjoyable.

**Dr. Sergey Rykovanov and Dr. Ioachim Pupeza** for jam sessions and broadening of musical horizons.

**The IMPRS programme** and Frau **Monika Wild** for your great efforts in providing a wonderful PhD network.

**LMU and MPQ technical staff** Manfred Fischer, Alois Böswald, Anton Horn, Harald Haas, Hans-Peter Schönauer für eure Ünterstutzung beim technischen Aufbau der Experimente. Rolf Öhm, Thomas Strobl und Michael Rogg und deren Mannschaften fur die stets kompetente Beratung und schnelle Bearbeitung unserer mechanischen Aufbauten trotz optimierungsbedürftige CAD-Zeichnungen.

**Meine Eltern** Danke dass ihr mich im Leben immer ermuntert und unterstüzt habt obwohl es zu einer so grossen räumlichen Entfernung geführt hat. Ich bin sehr dankbar dass ihr stets an meiner Seite steht.

**Anja, Leo, Mika** For my bachelor thesis I thanked Anja for her support and lemon cookies. Little did I know where my pursuit of a PhD would lead. I thank you for your love, support, and patience over so many years.